Master's thesis

NTNU
Norwegian University of Science and Technology
Faculty of Engineering
Department of Mechanical and Industrial Engineering

Sondre Audal

Validation of Force Propagation Through Composite Suspension Members On A Formula Student Race Car

Master's thesis in Mechanical Engineering
Supervisor: Jan Torgersen
June 2022

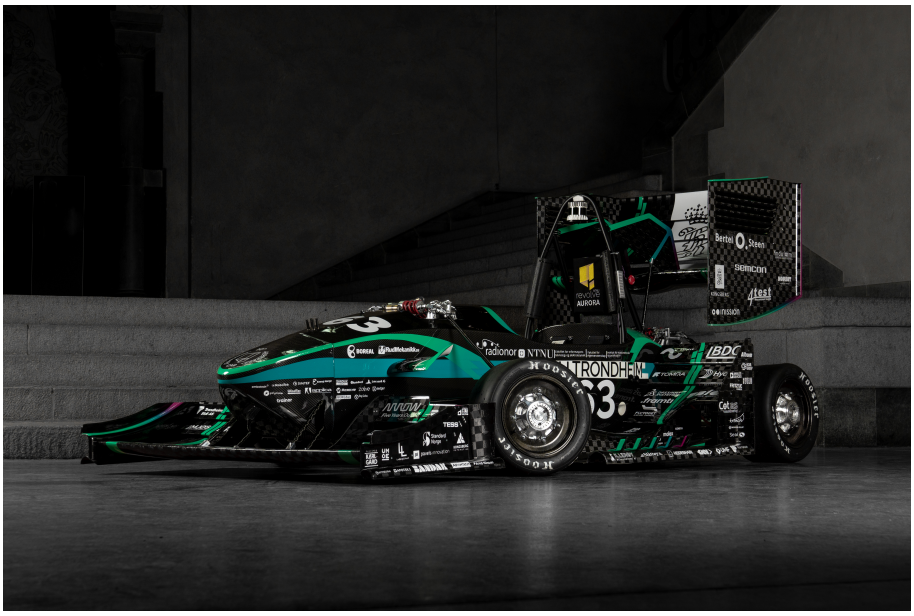

NTNU
Norwegian University of
Science and Technology

Sondre Audal

Validation of Force Propagation Through Composite Suspension Members On A Formula Student Race Car

Master's thesis in Mechanical Engineering
Supervisor: Jan Torgersen
June 2022

Norwegian University of Science and Technology
Faculty of Engineering
Department of Mechanical and Industrial Engineering

NTNU
Norwegian University of
Science and Technology

Abstract

This thesis aims to validate the forces acting on a Formula Student race car suspension through quasi-static testing. Comparing the reaction forces in two vastly different Abaqus models: one with only connectors and one containing all the front left suspension parts.

Ensuring good simulations is vital to designing a lightweight and comprehensible car. By comprehensible, we mean understanding the compliance which is present in the suspension. Validation of simulations is possible in many ways, but the best way is to compare the results to real-life testing. Performing quasi-static testing with different load cases and comparing the results against two vastly different Abaqus simulations yielded a wide range of results. More interesting was that the different Abaqus models also yielded different results!

The differences in peak load in the Abaqus models were 32.7%, and compared to quasi-static testing, the deviation was between 361.7% and -61.56% in comparable load scenarios.

Sammendrag

Denne oppgaven prøver å validere kreftene som virker på en Formula Studen racerbils hjuloppheng igjennom kvasi-statisk testing. Sammenlikning av opplagerkreftene i to vesentlig forskjellige Anaqus-modeller: én med bestående av bare *connectors*, og én som inneholder alle delene i fremre venstre hjuloppheng.

Å forsikre seg om gode simulering er vitalt for å designe en lettvekts- og forståelig bil. Med forståelig menes at vi forstår hvordan ettergivenhet (*compliance*) er tilstede i hjulopphenget. Validering av simuleringer er mulig igjennom mange muligheter, men den beste måten er å sammenlikne mot resulter fra fysisk testing. Å gjennomføre kvasi-statisk testing med forskjellige lastscenarioer og sammenlikne resultatene mot to svært forskjellige Abaqus-simuleringene ga et vidt spekter av resultater. Mer interessant var at de forskjellige Abaqus-modellene også ga forskjelle resultater!

Forksjellen mellom de høyste lastene i Abaqus-modellene var 32.7% og sammenliknet med den kvasi-statiske testingen, var avviket mellom 361.7% og -65.56% i sammenlignbare lastscenarior.

Preface

Thank you to all the people I have met throughout my years at NTNU, and especially those ambitious, dedicated, and innovative people I have met during my time in Revolve NTNU. Thank you to friends and family for holding on all these years.

Also thank you to all the embedded and control systems guys for making this testing possible, without you, this thesis would have been a thin soup.

Det måtte jo bli sånn.

Sondre Audal
Trondheim, June 10, 2022

Contents

List of Tables

List of Figures

Nomenclature

R_G Undeformed strain gauge resistance

ϵ Strain

ALLCCE Contact constraint elastic energy

ALLCCEN Contact constraint elastic normal energy

ALLCCSD Contact constraint stabilization dissipation

ALLCCSDT Contact constraint stabilization tangential dissipation

ALLCCSDN Contact constraint stabilization normal dissipation

ALLCD Energy dissipated by viscoelasticity.

ALLCW Work done by constraints penalties.

ALLFD Frictional Energy Dissipation.

ALLHF External heat energy through external fluxes.

ALLIE Internal Energy.

ALLIHE Internal Heat Energy.

ALLKE Kinetic Energy.

ALLLAE Artificial strain energy.

ALLMW work done by propelling added mass.

ALLPD Inelastic strain energy.

ALLPW Work done by contact penalties.

ALLSE Stored strain energy.

ALLVD Viscous Energy Dissipation.

ALLWK Work done by the externally applied loads.

ETOTAL Total Energy.

F Force applied.

GF Gauge Factor

R Resistance

s Distance moved.

W Work done.

Acronyms

CAD Computer Aided Design. 59, 60, 80

CAE Computer Aided-Engineering. 60

CFRP Carbon Fibre-Reinforced Polymer. 6, 18, 20, 79, 80, 86

DCU Damper Control Unit. 25

DOF Degrees Of Freedom. 17, 84, 85

etc Et cetera. 60, 61

FEA Finite Element Analysis. vi, vii, 3, 6, 17, 24, 31, 40, 44, 59, 61, 77

FLA Front Lower Aft. xi, 7, 39, 40

FLF Front Lower Fore. xi, 7, 21, 39, 40

FS Formula Student. 1

FSG Formula Student Germany. 2, 5

FUA Front Upper Aft. xi, 7, 39, 40, 61

FUF Front Upper Fore. xi, 7, 39, 40, 67

LHS Left-Hand Side. 80

RAM Random Access Memory. 17, 18

RF Reaction Force(s). 59

Chapter 1

Introduction

chapter 1 and chapter 2 will be heavily influenced by the authors previous work [1], with only minor changes to chapter 1, and some addendum to chapter 2.

1.1 Formula Student

Formula Student is the largest competition for engineering students. The competition was initiated by the Society of Automotive Engineers (SAE) in the United States of America. The competition is now worldwide, with different countries hosting the event. In Europe you have several countries hosting each summer, with the likes of Formula Student (FS) UK, FS Czech, FS Netherlands, FS Austria, FS East (based in Hungary), FS Spain, FS Italy and what is considered the most prestigious in Europe (if not the world): Formula Student Germany. The competitions is split into sub-events, which can be categorised as either a *static* or *dynamic* event, the full score overview is found at appendix A. For the last seven years, four-wheel-driven electric cars have proven to be the way to go; this is also the foundation Revolve NTNU has built its last five cars on. The competition is regarded as one of the biggest recruitment and development platforms for young automotive engineers.

1.2 Revolve NTNU

With key values of being innovative, dedicated, and ambitious, Revolve NTNU has managed to establish itself as a top contender in the competitions. Revolve NTNU has proven

Figure 1.1: Revolve NTNU's car for 2022: Aurora

they can design good race cars, proven by lightweight solutions, roll - and heave decoupled suspension, four-wheel-driven electric powertrain, and a lift-to-drag ratio over 3.1. In the 2021 season, Revolve NTNU's car, Luna, proved this by winning the skid-pad event at FSG.

1.3 Motivation

Running massive simulations with lots of parts and interactions is both frustrating and pleasant: Frustrating when it does not run, when it struggles to converge, errors in the contact pairing, having it run for half the simulation, for then to abort due to lost contacts. It is pleasant when it finally runs after days of reading manuals, message files, and discussing with professionals, and the results look plausible, and stress contours look amazing. However, just because it is a pleasant feeling does not justify the list of frustrations. A massive simulation is time-consuming; all the steps for doing a simulation: setup time, run-time,

and post-analysis. A simple simulation, which is close to real life, using simple features, and keeping the number of nodes low, is what real yields the results. Saving time in the setup time, run-time, and post-analysis, enables the engineer to spend his/her/their time more efficient, developing heart pumps, sterling heat pumps, or, as for me, race cars.

Knowing how good a simulation is could be hard to verify. Energies, reaction forces, and displacements are just a few ways to compare different Finite Element Analysis (FEA) simulations. The one thing that does not lie is real-life testing. It does not lie because it is happening, but that does not mean it could be misleading: poor equipment, poor setup, and even material irregularities are all factors that will affect the testing output.

The time-consuming and relatively expensive aspect of running these validation testing has been some of the reasons for Revolve NTNU not to run these. The equipment used also requires a) mechanical setting up/made, and b) electrical systems, required for data acquisitions, and c) post-testing analysis. Considering the nature of a year in Revolve NTNU; very few have the time to set up the and conduct it - the car has around a month between its first drive and its first competition.

The motivation expands upon the curiosity of comparing FEA-models. Knowing that if this test-setup works, this compact design could be utilised during testing, gathering live data from driving. This could allow for tyre data validation and getting to grips with how the tyre works against the road surface.

1.4 Objectives

This thesis aims to discover the consequences of the different modelling approaches and compare and validate them with real-life testing data. The modelling approaches will be a rigid beam model and an assembled model of the front left suspension.

Important parameters are for the simulation comparisons are:

- Run-time - how long does it take to run the model? Longer run-time usually means fewer iterations upon (1)design and (2)setup of model[1].
- Setup time - how long does it take to set up the model? A longer setup time means a taller ask to perform the analysis. Also, a longer setup time means less time for design iterations. Abaqus has a very powerful Python-scripting module[2]; this will only be briefly touched upon but not utilised to its full potential.

[1] Mesh convergence, contact definitions, i.e.

- Accuracy of results - how far away from real-life data is it?
- Is the simulation over-estimating or under-estimating? - This needs to be seen with respect to the point above, but knowing if the model is under-estimating reaction forces is essential so that the safety factor can be added post-analysis. If the models are over-estimating; the non-yielding criteria can be more lenient when small, yielding areas exist.

The testing will thus be performed on the front left suspension of the R22 car, Aurora.

Chapter 2

Pre-study

2.1 Initial Assessment

As mentioned in section 1.3, Revolve NTNU aims at a top 3 in FSG, and the in-house developed lap time simulator [3] shows that a 1% reduction in mass would yield a loss in an autocross lap time of 0.27%. Only increased lateral and longitudinal grip yields a better investment per cent - 0.57% and 0.35% respectively. Due to the lack of simulation equipment and validated tire models, it is hard to verify and quantify the consequences.

To ensure the safety of drivers, knowing the correct load cases is crucial. Almost equal to that, knowing the magnitude of the force propagation is highly important. Revolve NTNU has been using different estimations of the latter: from MATLAB scripts to probing infinitely stiff Abaqus models and free-body cutting the Abaqus models. These have yielded different results; thus, no one is sure how these forces propagate.

This thesis will examine how different modelling approaches vary and how they will compare versus real-life measurements. The measurements will be done using strain gauges. For this, the front left suspension of the R22 car, Aurora, will be assessed, mainly the A-arms.

2.2 Previous Work And Contributions

In 2018, Haugland wrote a thesis on the correlation between FEA and experimental testing. The thesis concluded on deviations between **-10%** and **48.8%** [4]. Studies by Autio et al. [5] also shows that strain gauging composites can vary to a great extend. Due to the race car nature of the vehicle and system in question, strain gauging the current setup is considered a suboptimal approach: The suspension systems aim to minimise compliance; thus, anisotropic CFRP is preferred instead of the denser, softer, isotropic aluminium. Huagland pinpointed in his thesis that the strain gauging, the method and readings, could be one of the causes for the great deviation between FEA and the experimental testing [4].

2.3 Suspension Members

For the 2022 season, Revolve NTNU opted for a new suspension setup, transitioning from the T-bar setup, introduced back in 2018[6, 7], to a roll-heave decoupled suspension. The latter allows for running coilover springs and dampers in both roll and heave mode, with the compromise of removing corner coilover dampers. This concept can be seen the likes of Mercedes AMG Project One[8, 9] and other high-performing Formula Student cars[10–12].

2.3.1 Naming Conventions

The suspension follows the naming convention described in the leading vehicle dynamics book, used by Revolve NTNU, among others: *Race Car Vehicle Dynamics* by Milliken and Milliken [13].

For this thesis, the front left suspension of Aurora is the topic of interest.

2.3.2 Compliance Chain

As seen in Figure 2.1, the front suspension is a complex assembly with over 250 components. None of these parts are infinitely stiff, hence they will act as a spring, a phenomenon known as *compliance*. Assessing the equation for displacement for a axially loaded bar, we have:

$$\delta = \frac{FL}{AE} \tag{2.1}$$

Where δ is the displacement, F is the load, L is the length, A is the cross-section area, and E is the E-modulus.

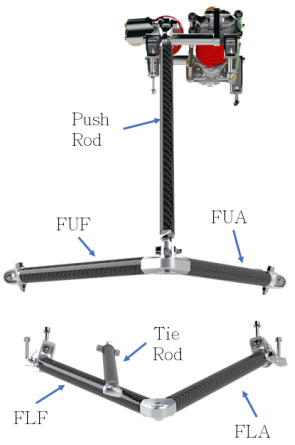

Figure 2.1: Naming of the front suspension, explaining FLF, FLA, FUF, FUA, push-, and tie rod.

Rearranging the equation, we can obtain that:

$$F = \frac{AE}{L}\delta \tag{2.2}$$

which corresponds greatly with the formula for force in spring:

$$F = kx \tag{2.3}$$

where k is the stiffness of the spring and x is the spring's displacement. Due to this nature, compliance also responds the same way when induced in series (Equation 2.5) and when in parallel (Equation 2.4) of N springs.

$$K_{total} = \sum_{n=1}^{N} K_n \tag{2.4}$$

$$K_{total} = (\sum_{n=1}^{N} \frac{1}{K_n})^{-1} \tag{2.5}$$

Revolve NTNU tends to emulate the compliance in suspension as seen in Figure 2.2. The reality is more like Figure 2.3.

Figure 2.2: Simplified compliance model with the monocoque on the left end and the ground on the right end.

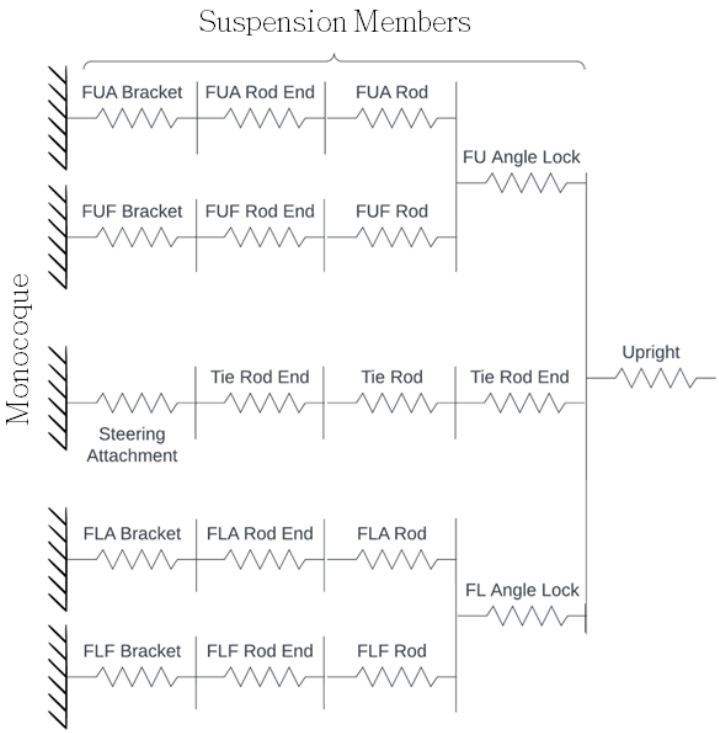

Figure 2.3: Illustration on how the compliance chain can be looked at. An angle lock is the piece that holds the paired rods (FxF and FxA) together.

From a practical point of view, the concept of looking at the simplified model (Figure 2.2) is frequently used by Revolve NTNU when designing parts [14]. This technique allows the team to avoid designing unnecessarily stiff parts, thus enabling a higher degree of weight saving.

2.4 Force Propagation In Assembly

For the given load cases, which is described in section 3.4, the forces will propagated in the manners shown in Figure 2.5 through Figure 2.10. Note that none of the arrows in the figures is up to scale nor quantified.

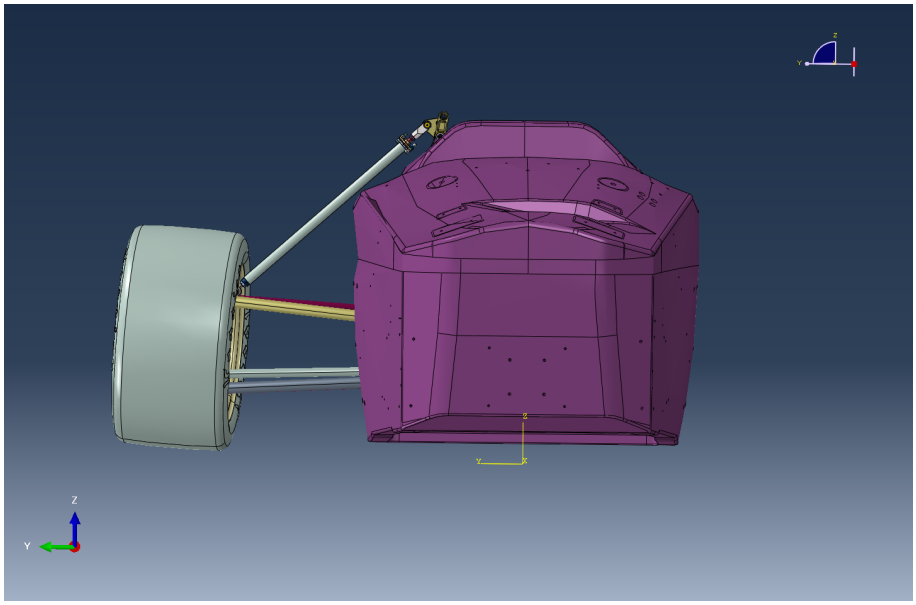

Figure 2.4: Rear view of the front left suspension.

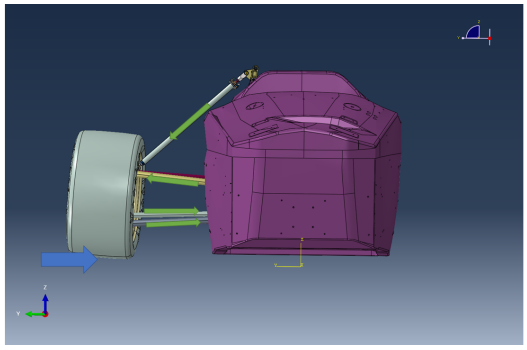

Figure 2.5: Force propagation in suspension when subject to pure lateral loading. Arrows not to scale.

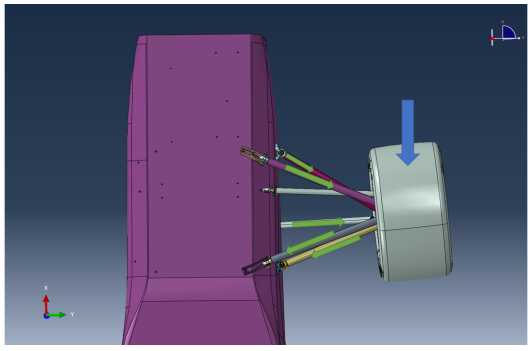

Figure 2.6: Force propagation in suspension when subject to pure longitudinal loading. Arrows not to scale.

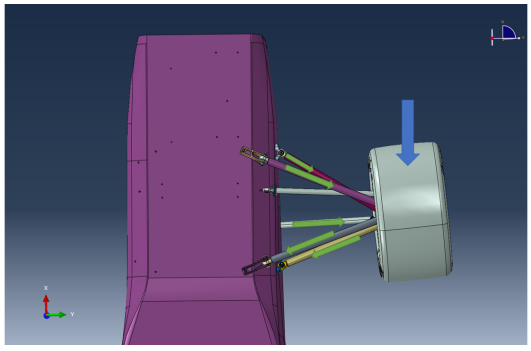

Figure 2.7: Force propagation in suspension when subject to pure longitudinal loading. Arrows not to scale.

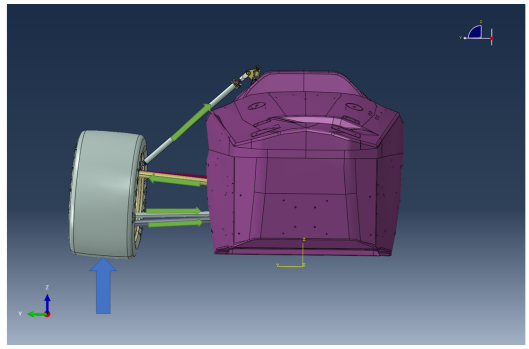

Figure 2.8: Force propagation in suspension when subject to pure Fz loading. Arrows not to scale.

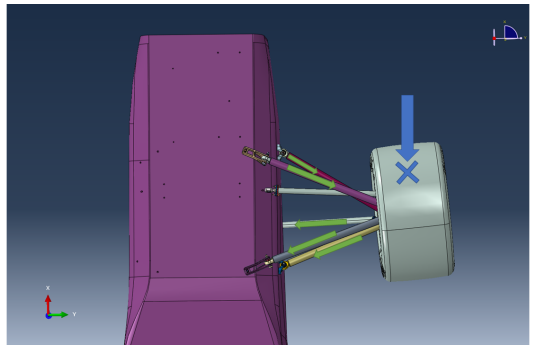

Figure 2.9: Force propagation in suspension when subject to combined Fz- and longitudinal loading. Arrows not to scale.

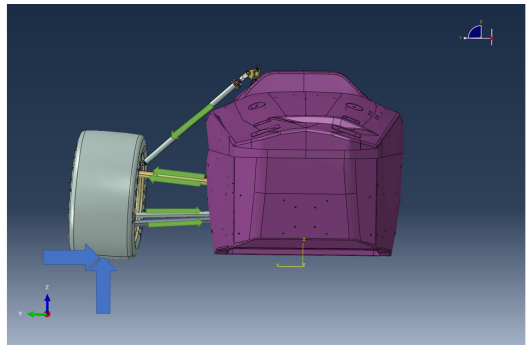

Figure 2.10: Force propagation in suspension when subject to combined Fz- and lateral loading. Arrows not to scale.

2.5 Theory

2.5.1 Energy

The energy in the Abaqus model is defined by this equation[15]:

$$\begin{aligned} ETOTAL = ALLKE + ALLIE + ALLVD + ALLFD + ALLIHE \\ -ALLWK - ALLPW - ALLCW - ALLMW - ALLHF \end{aligned} \tag{2.6}$$

Due to the scope of this thesis, not all parameters will be elaborated on further.

ETOTAL - Total Energy

ETOTAL is the total energy in the model, defined by Equation 2.6. This value should be approximately constant, with an error generally less than 1%[15].

ALLWK - Work done by externally applied loads

Continuously forward integrated. Defined by nodal forces and displacements.

$$\boldsymbol{W = Fs} \tag{2.7}$$

ALLIE - Internal Energy

Defined by equation:

$$ALLIE = ALLSE + ALLPD + ALLCD + ALLLAE \tag{2.8}$$

ALLSE is the stored strain energy in the model, thus a potential energy parameter. Strain energy is similar to energy stored in a spring.

$$U = \frac{1}{2} V \sigma \epsilon = \frac{\sigma^2}{2E} \times V \tag{2.9}$$

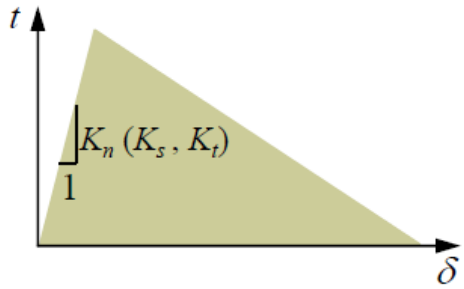

Figure 2.11: Traction-Separation Plot, provided by Dassault Systèmes and their lecture in *Surface-based Cohesive Behavior Lecture*.

2.5.2 Cohesive Behaviour

Cohesive Behaviour in Abaqus is a tool that enables elements with zero interface thickness to establish contact. It simplifies the simulation setup without the need for complex simulations, which has proven to be prone[16]. The feature is based upon this equation:

$$\mathbf{t} = \left\{ \begin{array}{c} t_n \\ t_s \\ t_t \end{array} \right\} = \left[\begin{array}{ccc} K_{nn} & K_{ns} & K_{nt} \\ K_{ns} & K_{ss} & K_{st} \\ K_{nt} & K_{st} & K_{tt} \end{array} \right] \left\{ \begin{array}{c} \delta_n \\ \delta_s \\ \delta_t \end{array} \right\} = \mathbf{K}\boldsymbol{\delta} \tag{2.10}$$

Where K_{nn} is the traction required to separate two surfaces in the normal (3) direction, and K_{ss} and K_{tt} are for the tangential direction - (1) and (2), respectively. The traction-separation behaviour of cohesive interactions can be further determined and provide complete control over the bonding property (Figure 2.11).

2.5.3 Strain Gauges

Strain gauges convert the change in length (*strain*) into an electrical signal. The strain gauge is a thin plastic film with strips of metallic traces. The strain gauge is then bonded to the specimen in question; thus, the metallic traces will alter in length, corresponding to the changes at the bonded surface. The change in length will change the cross-section of the traces; hence the resistance will change, which is detectable. This measurable change is called *Gauge Factor*, denoted *GF* . That gives the following equation:

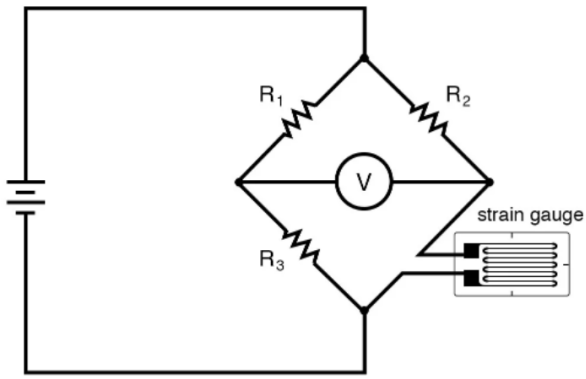

Figure 2.12: Circuit diagram of a quarter-bridge strain gauge circuit, also known as a Wheatstone bridge circuit.

$$GF = \frac{\Delta R/R_G}{\Delta L/L} = \frac{\Delta R/R_G}{\epsilon} \tag{2.11}$$

R_G is the resistance of the un-deformed strain gauge.

Since the values are diminutive, a Wheatstone bridge design is utilised, as seen in Figure 2.12. Figure 2.12 shows a quarter-bridge circuit, named because only one-quarter of the resistance is fitted with strain gauges. Half- and full-bridge circuits also exists[17] but are not utilised in this thesis. By balancing two legs of a bridge circuit, where one is the unknown resistance, the Wheatstone Bridge is exceptionally accurate and thus is proven helpful for strain gauges[17].

The strain gauge will have the resistance R_x, and hence, the balancing equations, following Figure 2.12, will look like:

$$\frac{R_3}{R_1} = \frac{R_x}{R_2} \tag{2.12}$$

$$R_x = \frac{R_3}{R_1} \times R_2 \tag{2.13}$$

The equation for measured voltage will then be:

$$\frac{V_{out}}{V_{in}} = \frac{R_3}{R_1 + R_3} - \frac{R_x}{R_x + R_2} \tag{2.14}$$

$$V_r = \frac{V_{out}}{V_{in-strained}} - \frac{V_{out}}{V_{in-unstrained}} \tag{2.15}$$

Where V_r is the exciting voltage of the bridge. Combining Equation 2.12 and Equation 2.15, yields the following equation:

$$\frac{\Delta R}{R} = \frac{-4V_r}{1 + 2V_r} \tag{2.16}$$

Which again can be substituted in Equation 2.11, and give:

$$GF = \frac{-4V_r}{\epsilon(1 + 2V_r)} \tag{2.17}$$

Chapter 3

Method

3.1 Finite Element Models

Two FEA-models were run: one with only connector elements (rigid beam model), and one was modelling the whole system with parts assembled. These two will be compared and discussed, both versus each other but also against the physical testing.

3.1.1 Beams & Connectors

This model is based on Abaqus' integrated feature of connecting reference points between each other. For this assignment, only links[18] and beams[19] properties have been opted for. *Links* constrains the translations' Degrees Of Freedom, whilst *beams* constrains both translation and rotational degrees of freedom. Effectively, it means links do not carry moments between the reference points, thus effectively emulating the rods with spherical bearings at each end. On the other hand, beams carry moments and thus seem great to emulate solid suspension parts, such as the upright and angle lock. Since this model only has twelve nodes, making it computationally easy and thus quick to run, even on an elderly computer with an Intel i7-4790 with four cores, eight logical processors, and 20 gigabytes of RAM.
The lack of upper suspension modelling is deemed inferior as the physical test will utilise stiff/solid dampers on the top, meaning the push rod pick-up point will be fixed in space. The latter is a simplified statement as the new dampers and the rocker system will have some compliance which will make the pick-up point move. The model is reliant on the

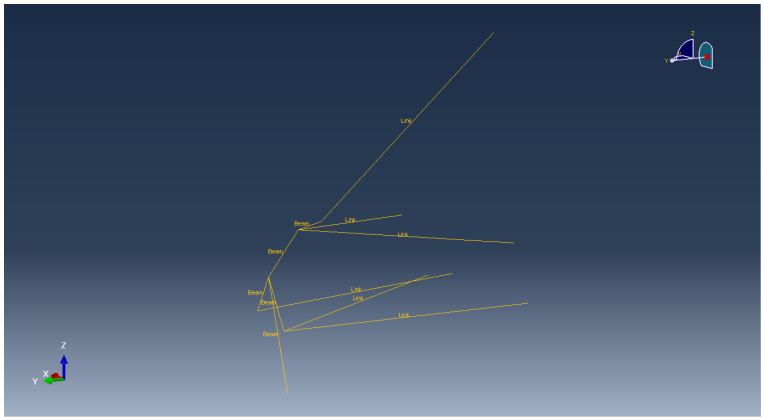

Figure 3.1: Front left connector suspension in Abaqus.

suspension pick-up points and the connector assignments.

3.1.2 Assembled Model

Trying to emulate reality in, if done correctly, more realistic matter, a model of the front left suspension was made in Abaqus. This model contains all the associated parts in the structural outboard suspension and their corresponding interaction: The CFRP rods are bonded together, simulated with an uncoupled cohesive interaction. The K_{ss}, K_{nn}, and K_{tt} parameters from Equation 2.10 are set at 3000, 800, and 800 respectively. The interaction between metallic parts in contact is modelled using hard normal contact and penalty tangential contact. The coefficient of friction is chosen based on which material is in contact. Surface-to-Surface contact is utilised to ensure complete control of the interactions and their properties. Surface-to-surface contact also enabled contact control, a feature proven helpful as the simulations are of great magnitude and thus have an increased potential of running into errors such as too big displacements and contact force errors. The threads are modelled with tie constraints [20]. The upright is left outside the scope of this thesis and thus the simulation. Including the upright would engage in a more significant number of contacts, bolt loads, and a greater number of elements to be calculated. Therefore, the upright is modelled as beam elements like in subsection 3.1.1, with pick-up points coupled to the appropriate bearing. The setup is detailed in Appendix B. The assembled model is undoubtedly a heavier simulation than those mentioned earlier. The simulation ran on a computer with an AMD Ryzen 9 5900X 12-Core Processor[1] and 64 gigabytes of RAM, with the simulation settings set to utilise 16 cores.

[1] Including 24 logical processors.

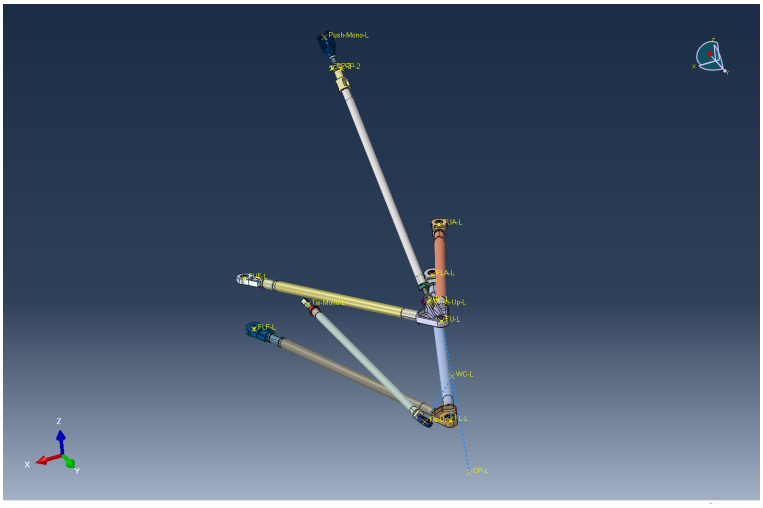

Figure 3.2: Front left assembled suspension in Abaqus.

3.1.3 *Errors*

In chapter 5, the differences will be discussed as *errors*. These are the definitions used in this analysis.

$$\Delta Model = Beam - Strain \tag{3.1}$$

$$\Delta Model[\%] = \frac{\Delta Model}{Beam} \times 100 \tag{3.2}$$

3.2 Physical Testing

In order to validate the models, physical testing is required. There are several ways of measuring load in structures, but the most common one is either load cells or strain gauges[21]. Revolve NTNU has used both in different variations[1][4]. Due to limited budgets, size constraints, and overall production complexity of the suspension system[2], and the potential of actually running the setup on the car during testing[3], the strain gauges were chosen. In order to acquire data more accurately than previously[4], special rod ends were made,

[2]The suspension system is bonded together using a jig which is not designed for big radius load cells to be installed at the rods. The rod ends are not radially bigger than the high-performance ones.

[3]The load cell used in [1] proved compliant not only in the axial direction but also in the radial direction, which is considered very sub-optimal.

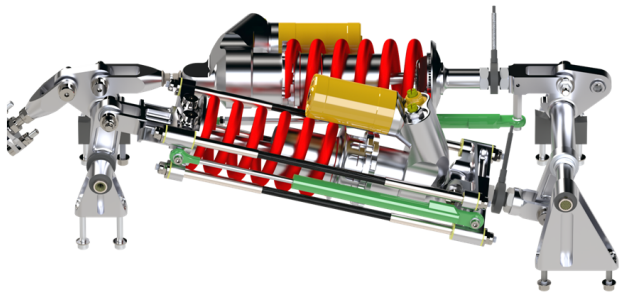

Figure 3.3: The top geometry with Öhlins dampers and coilover springs.

making the data acquisition state of the art. These rod ends are designed with inspiration from load cell technology [22]. Meaning they will be more compliant than the ones originally on the car due to the wanted strain. In order to not compromise the team's performance throughout the season, a spare suspension set was made for the front left corner. The design can be seen in Figure 3.4 and is implemented in the Abaqus model, see Figure 3.2. Note that the push rod also has implemented a new design for measuring strain. The push rod design did not make it on the car due to limitations mentioned in section 2.1. To not be affected by the coilover roll and heave dampers on the top of the monocoque, a set of solid fixtures were made. These lock the distance between the two rockers; thus the whole system is fully defined and will not move - apart from the compliance from the fixtures and rockers. The system can be seen in Figure 3.3.

Due to the lack of produced spare CFRP rods, the rods from the 2020-season were used. The layup is slightly different but should not affect the results in theory.

3.2.1 Rod End Design

Simulations (Figure 3.5 and Figure 3.6) proved the new design to be superior compared to the high-performance design, emphasising the state of the art potential.

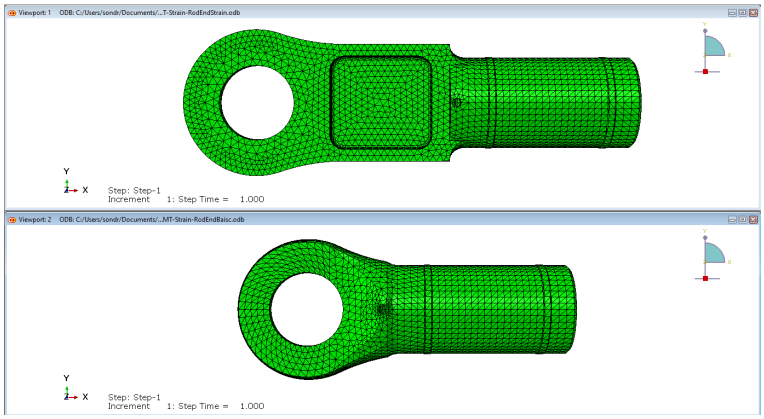

Figure 3.4: The two different rod end designs. The lower is the high-performance rod end. The upper shows the ones designed for strain gauging.

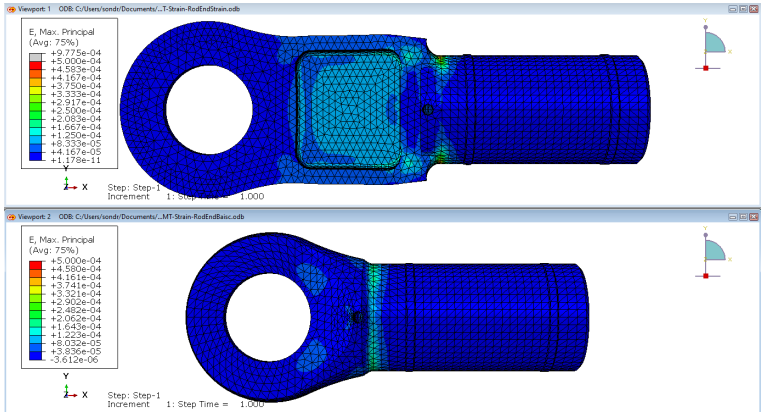

Figure 3.5: Differences in strain with compression loading of 1 kN.

Buckling

Since the design is softer than the old one, the risk of a lower buckling load is present. The increased weak spot of the suspension members has been proven to have a significant impact: during post-season testing in 2020, a load cell mounted in a test set-up for the push rod buckled under what should be considered slow driving.

The analysis was conducted using the *Buckling* step in Abaqus. Since the buckling load is proportional to the inverse of length, the analysis was only conducted on the longest A-arm: FLF, and the push rod, due to the different design. The buckling analysis was conducted by locking one end in all displacement directions and the axis along the rods

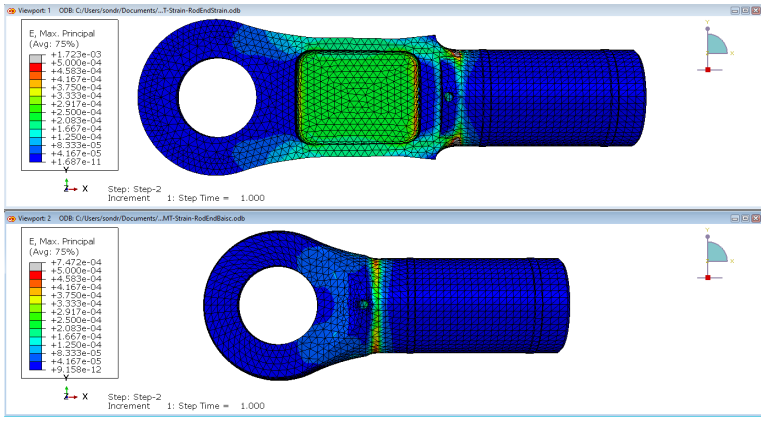

Figure 3.6: Differences in strain with tensile loading of 1 kN.

centre axis (U1, U2, U3, and UR1). The other end was constrained in all directions except for the one along the rods centre axis (U2 nad U3). These boundary conditions mean the lower end cannot move anywhere, nor twist around its centre axis, whilst the upper is allowed to move in the direction of loading. The setup is detailed in Appendix C.

The simulations yielded a buckling load of 13451 N in the lower A-arms, which is higher than the buckling load of the rods on the car. The higher buckling load is due to the rod being the weakest point in the chain, and when it is shortened, the buckling load increases. For the push rod, the buckling load is decreased and is approximately 4512 N, meaning the strain gauge design weakens the structure. Both of these statements are evident in the simulation results where one sees the buckling incident, see Figure 3.8.

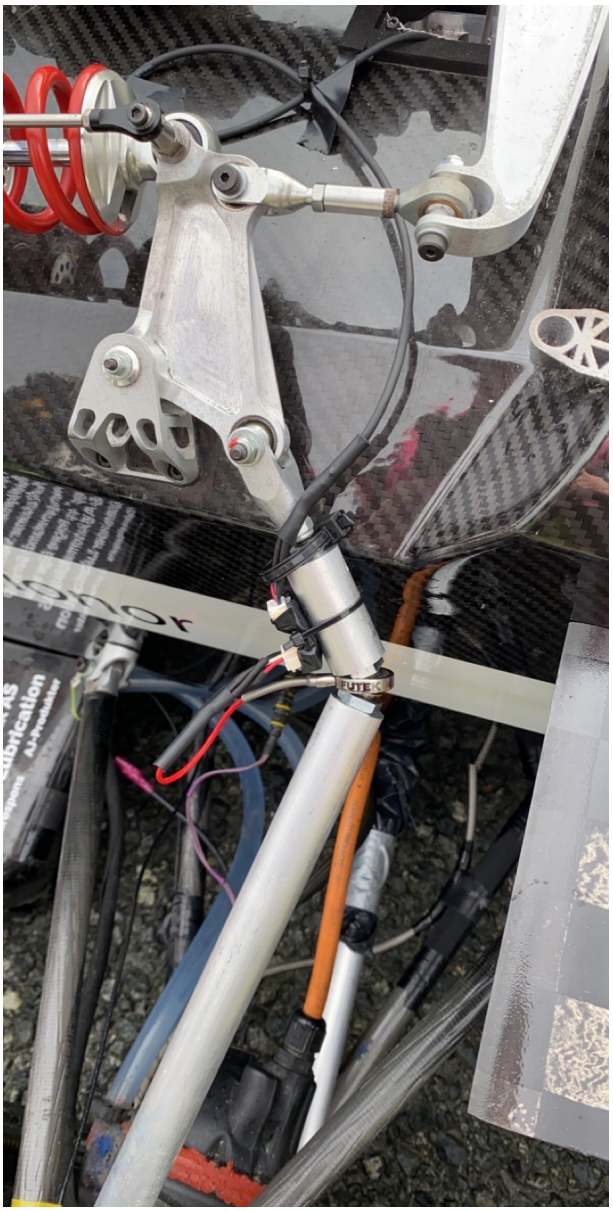

Figure 3.7: Buckled front right push rod on the 2019 car, Nova.

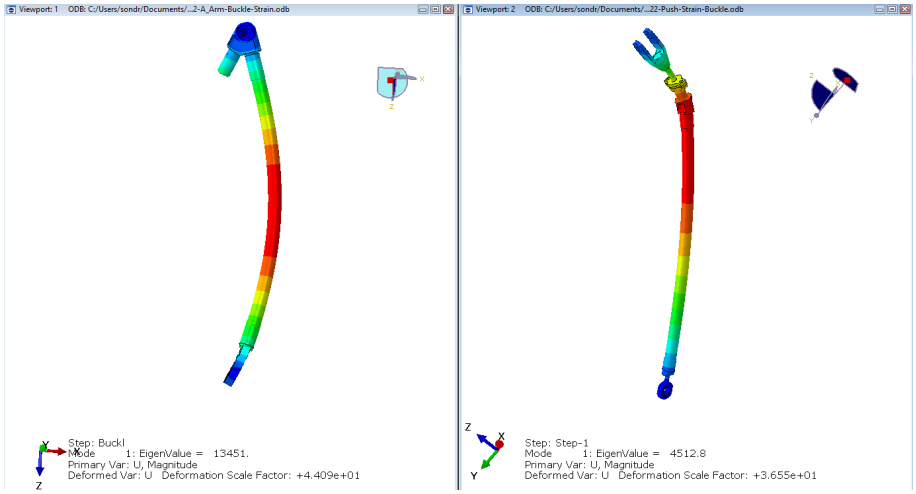

Figure 3.8: Buckling simulations of A-arm and push rod. Shows clearly where the buckling will occur.

3.3 Test setup

3.3.1 Quasi-Static Testing

Inspired by the quasi-static test jig in 2018[4], a similar one was designed to facilitate the newly introduced ring-gear-driven gearbox interface. The jig is made up by 30×30 mm steel square tubes and consists of two braces: one for the front and one for the rear. The front is mounted to the front bulkhead of the car. The front bulkhead is a section made to withstand a crash according to the rule set[23]. The rear bracing mounts to the accumulator cut-out underneath the monocoque - a structure designed to withstand accelerations of 40g in the longitudinal and lateral direction and 20g in the vertical direction[23]. Thus, these mounting points are adequate for the bracing. The test also utilises the same actuator used in 2018. The difference now is the changed hub setup caused by the transition to 10” rims in 2021. The new connection to the actuator also facilitates trail values.
In order not to get affected by springs and damper forces, fixed/solid dampers are mounted. This constraint is contemplated in the FEA-models by pinning the push rod pick-up point.

3.3.2 Actuator

The actuator is based on linear motion, with load cells reading the applied load. The actuator can only apply load in a maximum of two directions: X and Z, or Y and Z, seen

from the car frame. The actuator is mounted to the vehicle's hub[4] with a steel plate. The steel plate utilises the seven bolts used to attach the rim. The mounting points of the plate to the actuator are offset to simulate the trail values like the simulations. For lateral and longitudinal load measuring, the HBM U93A (Appendix E) is used. For vertical loading, a HBM U2 (Appendix F) was used.

3.3.3 Mounting of Strain Gauges

The strain gauges, HBM 1-CLY91-3/350ZE, were mounted in the pocket of the rod end, with the metallic traces oriented in the axial direction. Only the A-arms were prioritised to have the strain gauge mounted. This prioritisation is due to limited resources and the future investment of being able to run this setup during the testing phase of the project - as the push rod design would run the risk of buckling during real-life driving, as seen on the right-hand side in Figure 3.8.

The pockets were first cleaned with isopropyl alcohol before being sanded with 120 grit paper. Then cleaned again with isopropyl alcohol before the strain gauge was bonded to the sanded surface. One of the results are shown in Figure 3.11.

The strain gauge sends a voltage input to an amplifier card, then into an Damper Control Unit (DCU) - both developed in-house by Revolve NTNU. The amplifier card is located close to the strain gauge to minimise the noise caused by the wires going into the strain gauge. As the already installed DCU on the car had no free data channels available, a separate one was needed. Thus for the quasi-static testing, a separate DCU was set up outside of the car, both because of space limitation inside the cockpit and power shortage inside, as a new logistic and wire harness would have been necessary. The DCU is required due to data acquisition, as the in-house developed amplifier sends the signal in a format unsuitable for direct readings from i.e. an Arduino or a regular computer.

3.3.4 Constraining The Suspension

For the suspension not to move, which would alter the geometry and hence the load path, fixed dampers were made. Due to vehicle dynamical tuning, the heave damper was constrained in length with a machined aluminium rod with mounting options. The roll damper was constrained using an aluminium rod with clevises in each end; these are adjusted with an M6 bolt which is threaded inside the aluminium rod. Ideally, this would be a turnbuckle, but the limitations are limited by allowing one of the M6 bolts to turn freely within

[4] also the vehicle's rim center.

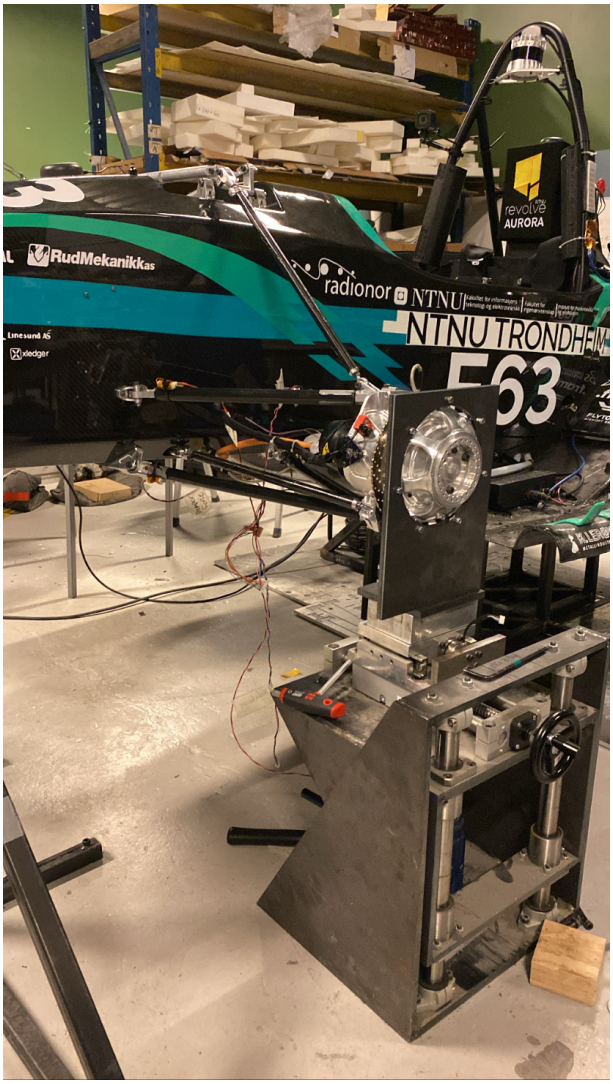

Figure 3.9: The actuator mounted on the suspension. Lateral loading scenario.

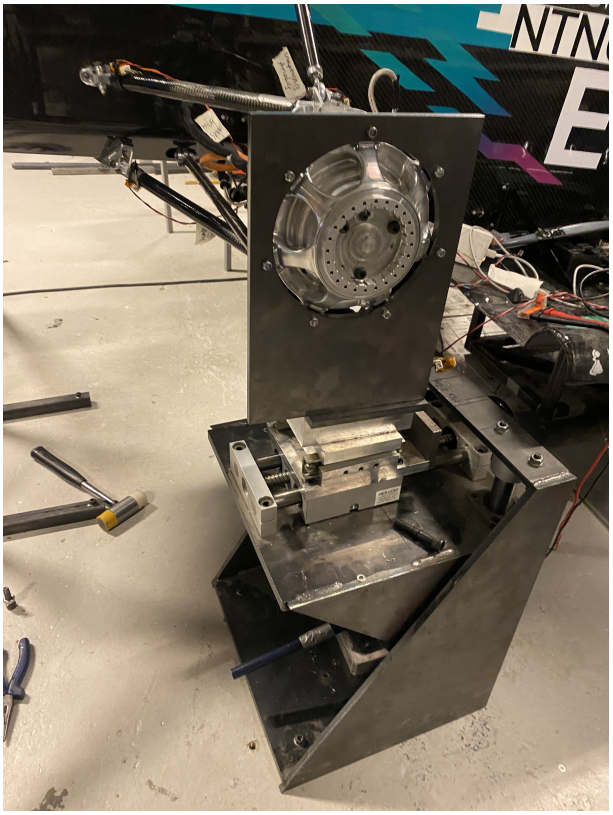

Figure 3.10: The actuator mounted on the suspension. Longitudinal loading scenario.

Figure 3.11: Strain gauge and amplifier mounted on the A-arm.

Figure 3.12: New A-arms mounted on Aurora.

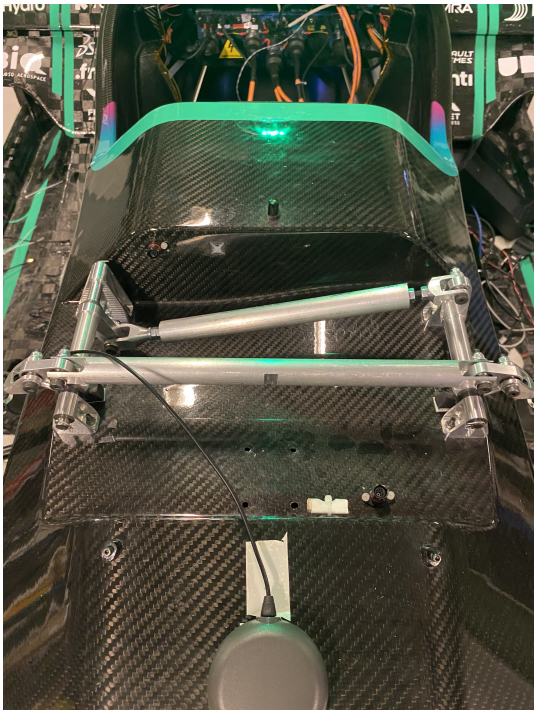

Figure 3.13: Fixed (top) suspension geometry

one of the forks.

3.4 Load Cases

In total, five load cases are run:

- Lateral - The load is applied in pure F_y. Up to 2500 N.
- Longitudinal - The load is applied in pure F_x. Up to 3000 N.
- F_z - The load is applied in pure F_z. Up to 2500 N.
- Combined load, Lateral + F_z - The load is applied in both F_y and F_z. Both directions are loaded to 2500 N.
- Combined load, Longitudinal + F_z - The load is applied in both F_y and F_z. Both directions are loaded to 2500 N.

These load cases are chosen based on the dimensioning load cases set by Revolve NTNU

(see section G).

For the FEA-model, the loading is applied using a *tabular* amplitude, with linear loading. For simplicity, the load is applied by a rate of $1000N/s$ during all steps/load cases. Therefore, the length of the step is the load divided by 1000.

After each load case, a neutralisation step is introduced. This step makes the model start with zero reaction forces acting on the members. No cross-loading should also be the case in real-life testing.

For the quasi-static testing, the load will be held for around three to five seconds to ensure good quality measurements from the strain gauges.

Chapter 4

Results

The probed values in the suspension pick-up points nodes during the different load cases are represented in this chapter. The rigid beam model took around **2 minutes** to run; most of the time is due to the pre-processing. The assembled model took **5 hours** to run with the specification mentioned in subsection 3.1.2.

4.1 Reaction Forces In Assembled Model

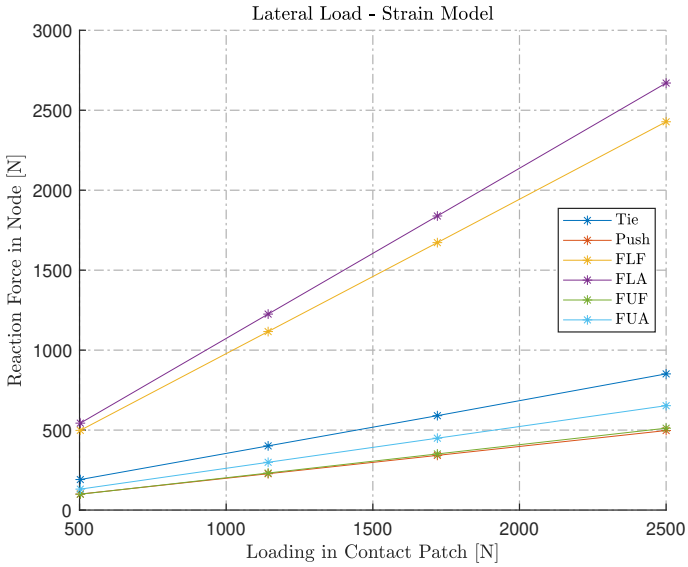

Figure 4.1

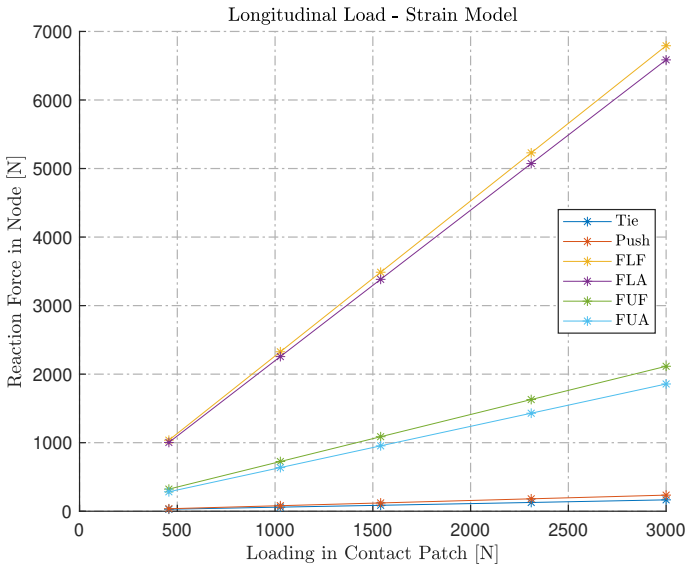

Figure 4.2

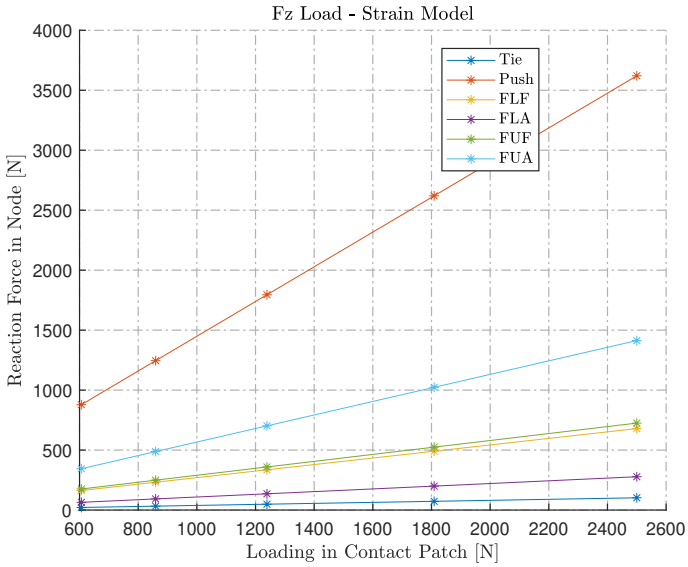

Figure 4.3

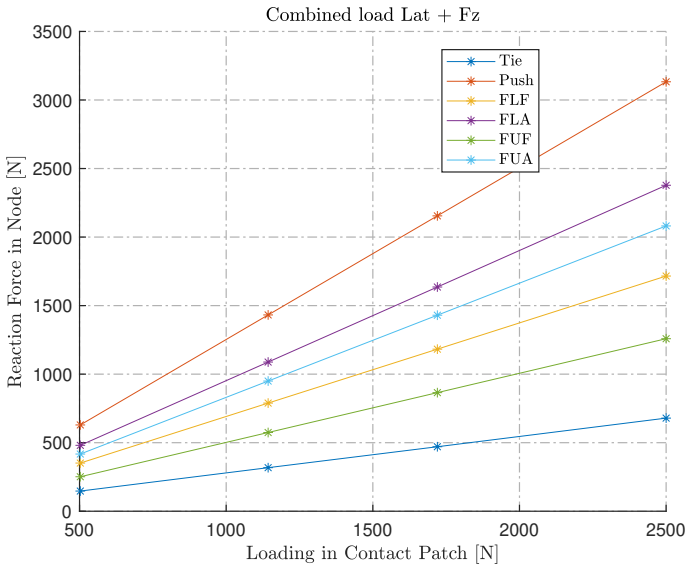

Figure 4.4

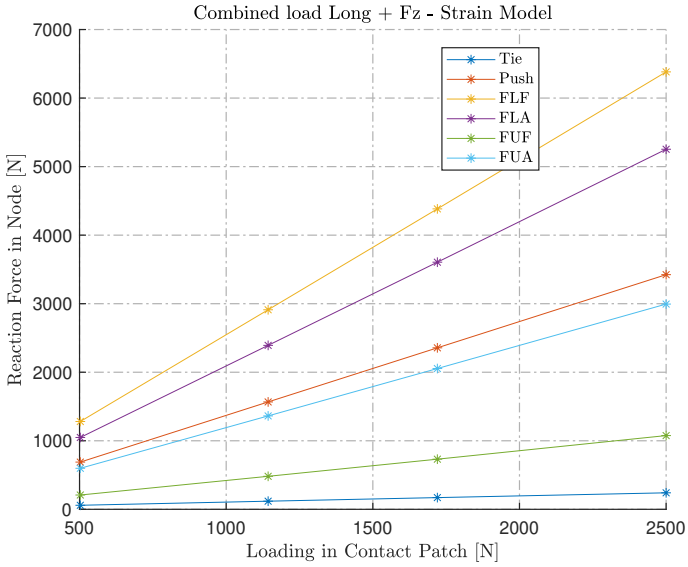

Figure 4.5

4.2 Reaction Forces In Rigid Beam Model

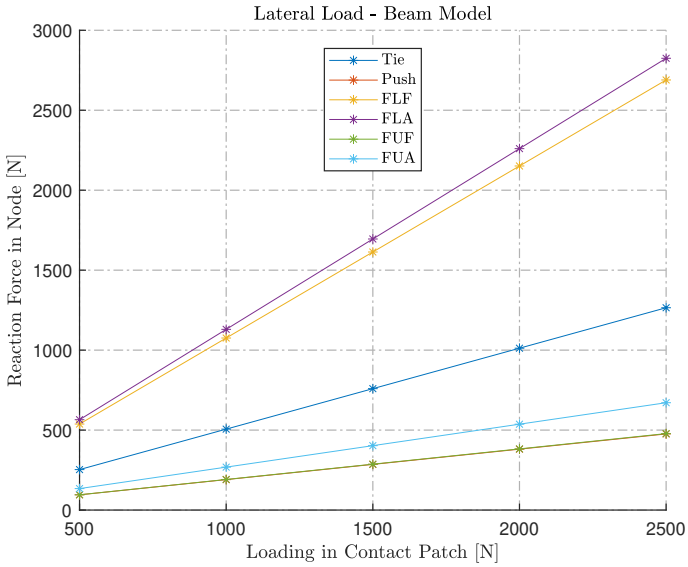

Figure 4.6

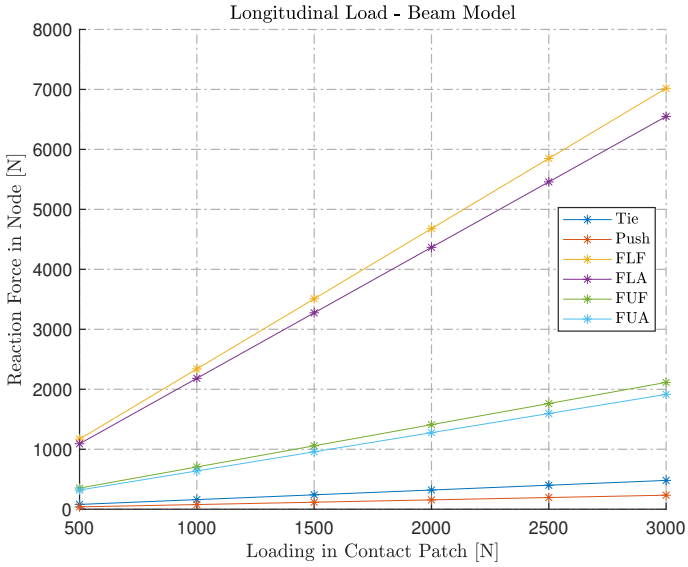

Figure 4.7

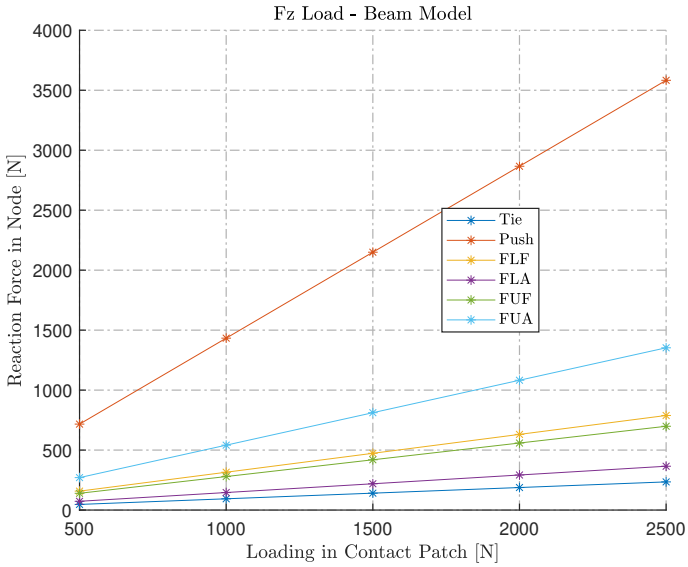

Figure 4.8

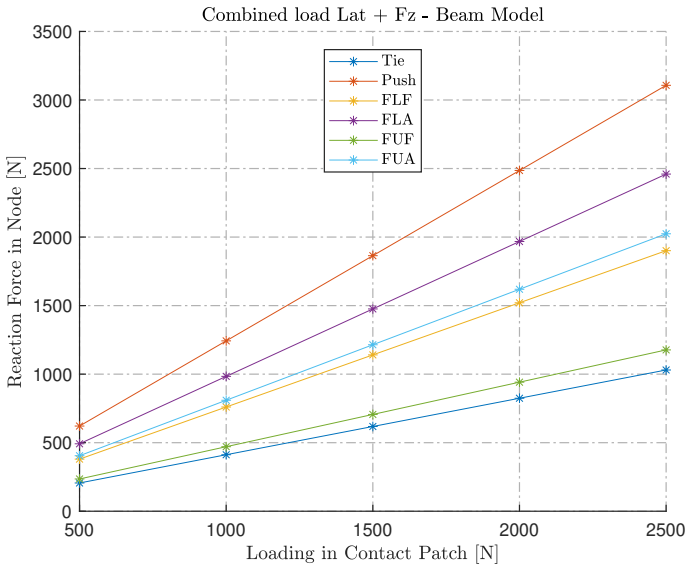

Figure 4.9

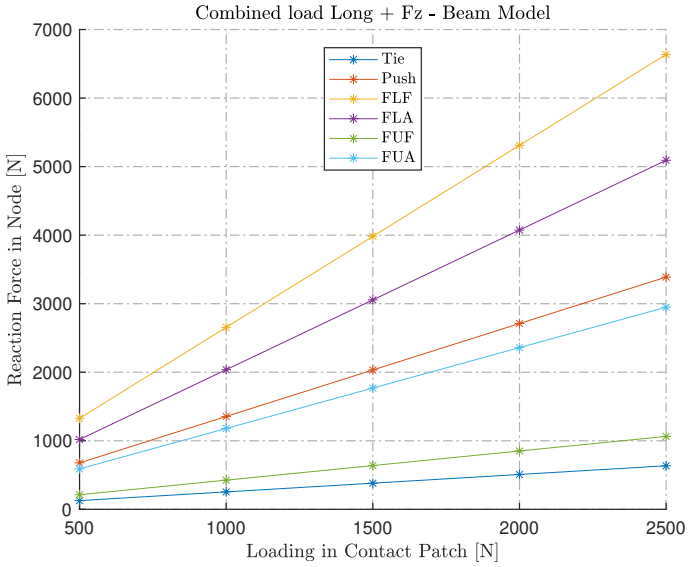

Figure 4.10

4.3 Peak Loads In Members & Their Corresponding Load Case

Beam Model		
Rod	**Magnitude**	**Load Case**
Tie	1265 N	Lateral
Push	3583 N	Fz
FLF	7018 N	Longitudinal
FLA	6550 N	Longitudinal
FUF	2115 N	Longitudinal
FUA	2949 N	Longitudinal + Fz

Table 4.1: Table overview of the peak forces found in the beam model, with subsequent load and load case.

Strain Model		
Rod	**Magnitude**	**Load Case**
Tie	851 N	Lateral
Push	3620 N	Fz
FLF	6792 N	Longitudinal
FLA	6585 N	Longitudinal
FUF	2115 N	Longitudinal
FUA	2994 N	Longitudinal + Fz

Table 4.2: Table overview of the peak forces found in the strain model, with subsequent load and load case.

4.4 Difference In Beam Model vs Strain Model

This section shows the difference between the FEA-models. There is a difference in step size and, thus, which step is available in the field output. In order to synchronise the field output, a linearisation process was applied to all reaction forces for each load case. Each load case was split into ten, regardless of the original length.

The plots show the beam model output, subtracted by the strain model output.

Beam minus/versus strain		
Rod	**Magnitude**	**Percentage**
Tie	414 N	32.7%
Push	-37 N	-1.03%
FLF	226 N	3.22%
FLA	-35 N	-0.05%
FUF	0 N	0%
FUA	-45 N	-1.53%

Table 4.3: Table overview of the difference in peak forces found.

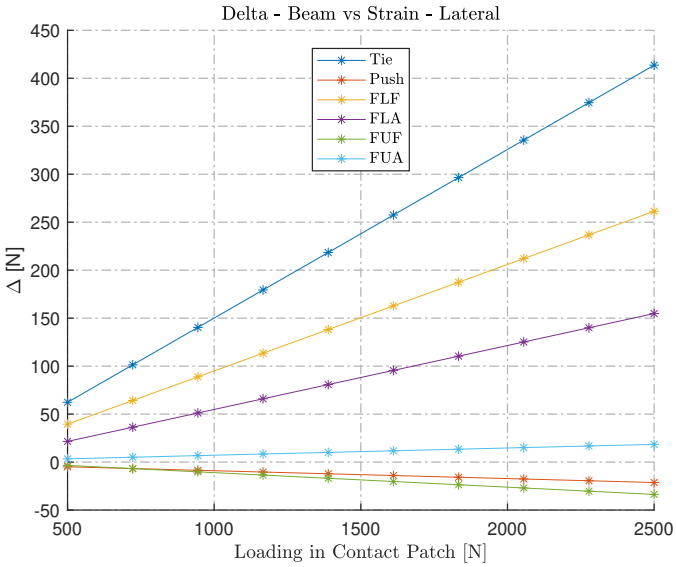

Figure 4.11

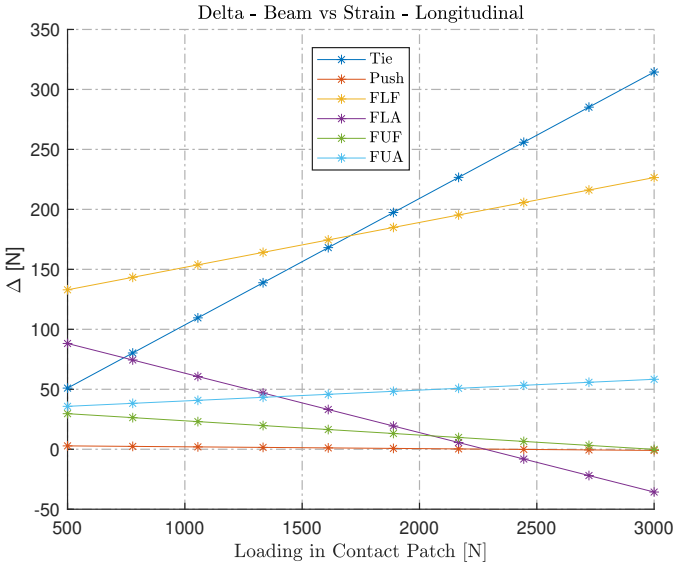

Figure 4.12

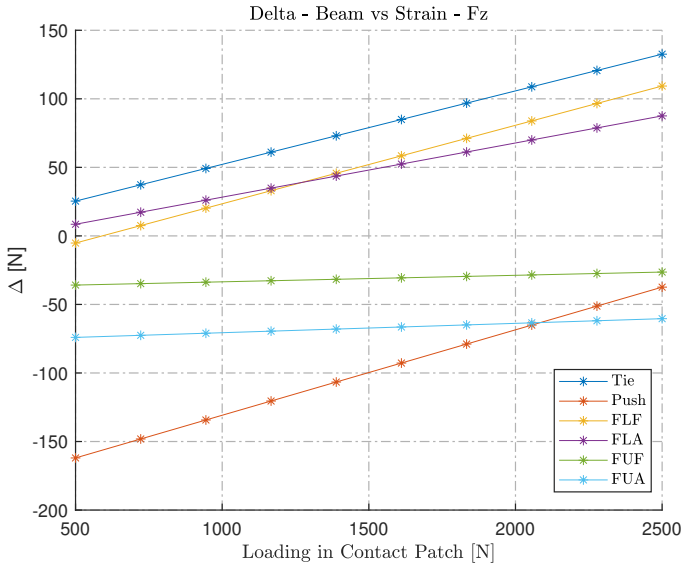

Figure 4.13

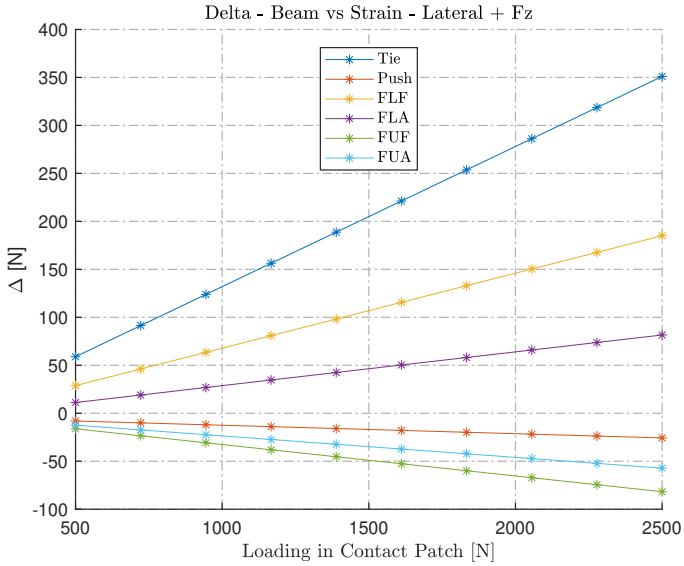

Figure 4.14

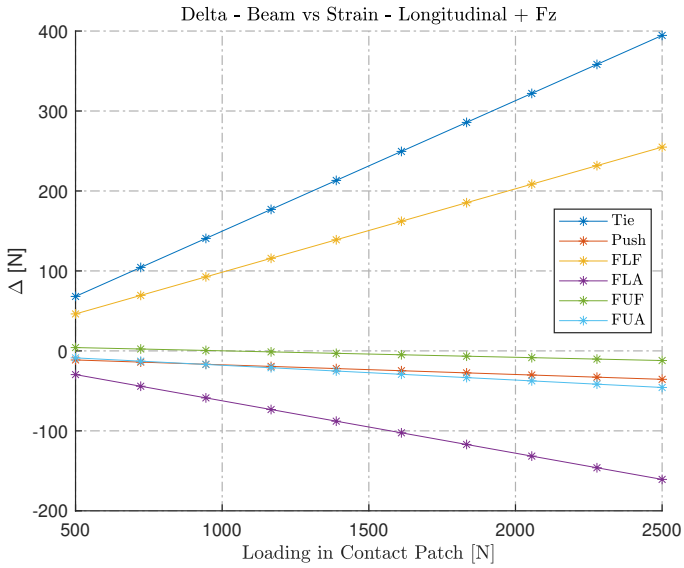

Figure 4.15

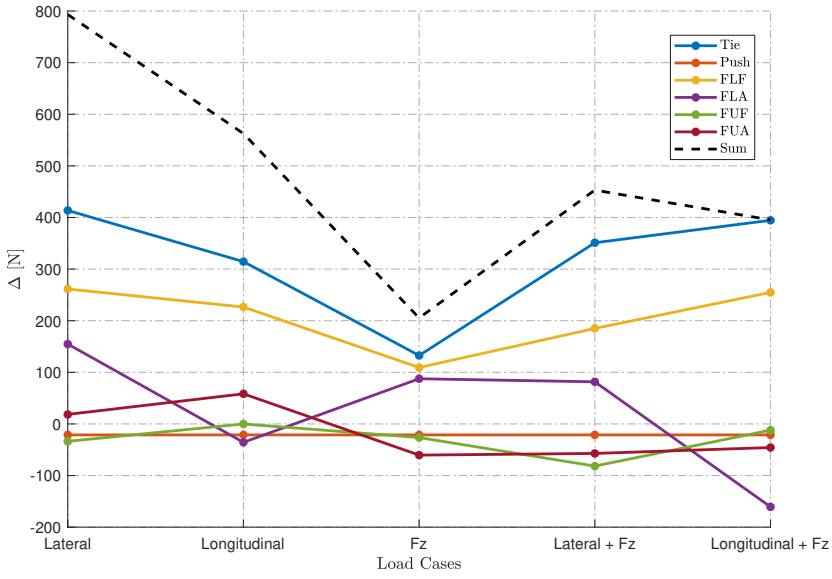

Figure 4.16: Difference in the end reaction forces and their sum. This graph does not differentiate between compression and tension forces.

4.5 Displacements And Energy In The FEA-models

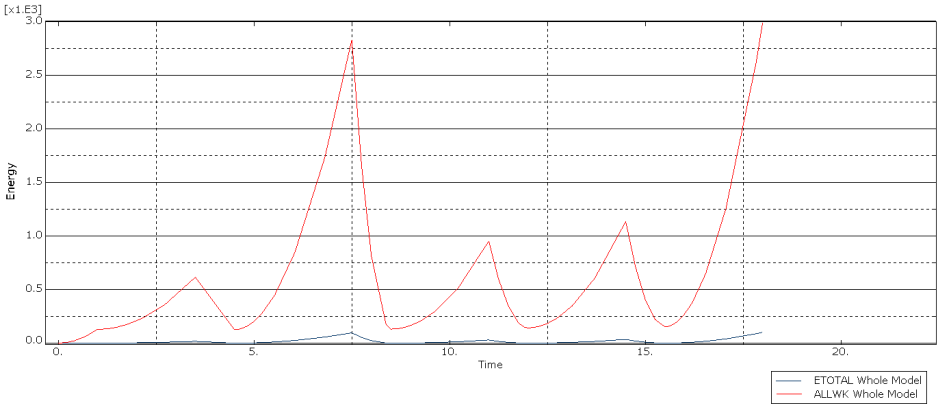

(a) *ETOTAL* and *ALLWK* for the assembled strain model.

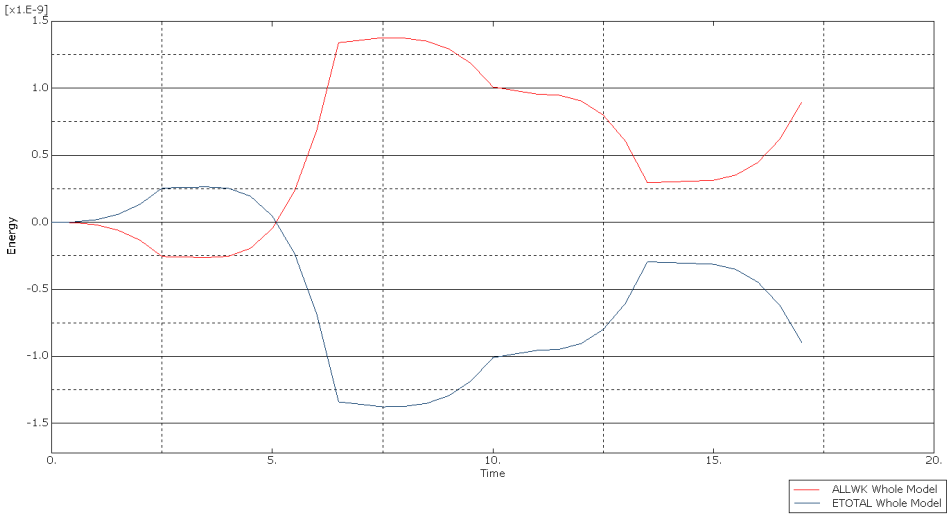

(b) *ETOTAL* and *ALLWK* for the rigid beam model.

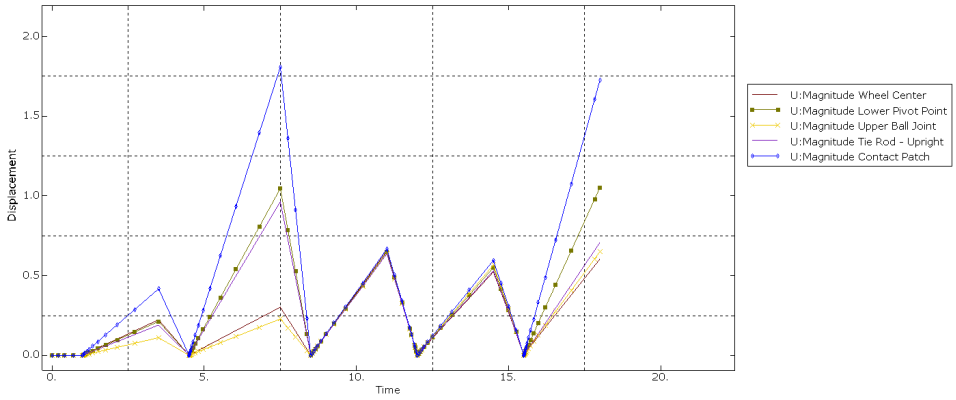

(a) Displacement for the assembled strain mode. Hidden nodes are boundary conditions and thus have no displacements.

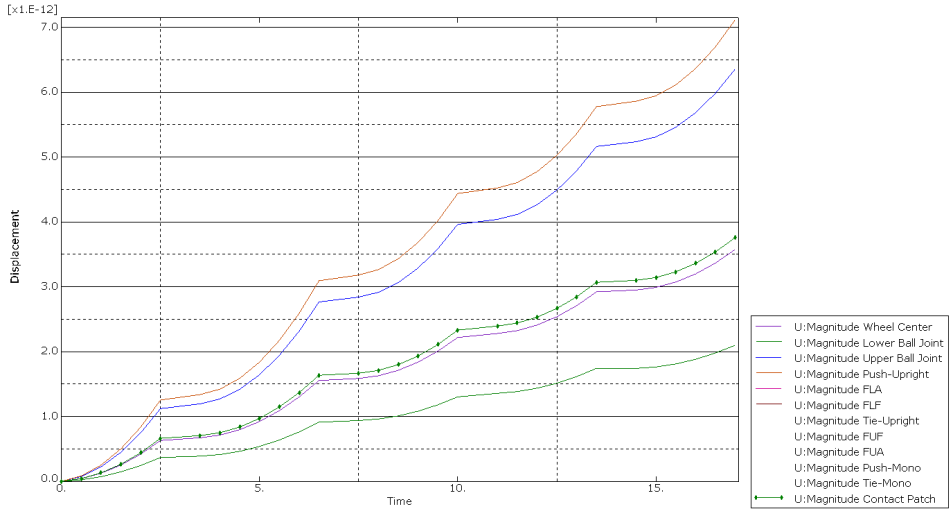

(b) Displacement for the rigid beam model. Hidden nodes are boundary conditions and thus have no displacements.

4.6 Testing

4.6.1 Corrected

Looking at Figure 4.19 to Figure 4.23, there is evidently some sort of offset. Looking at Figure H.5a, H.6a, H.7a, H.8a, and H.9a, there is some loading present at the beginning of the load scenario. In this section, this load (”base state”) is subtracted from the measurements - calibrating the results to the applied loading.

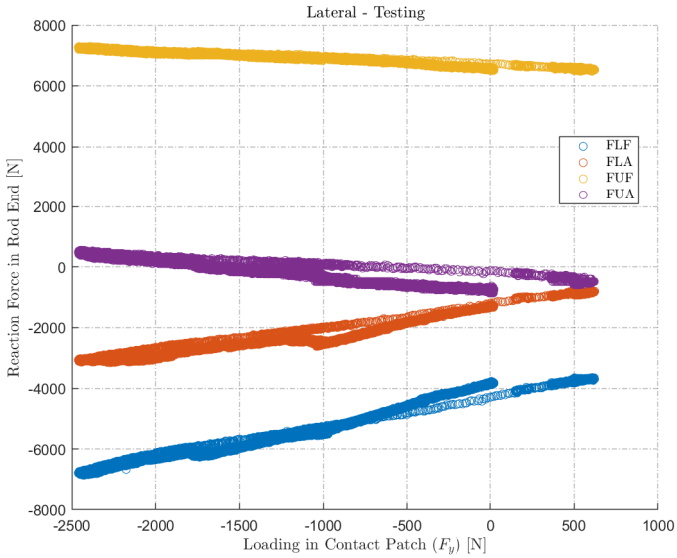

Figure 4.19

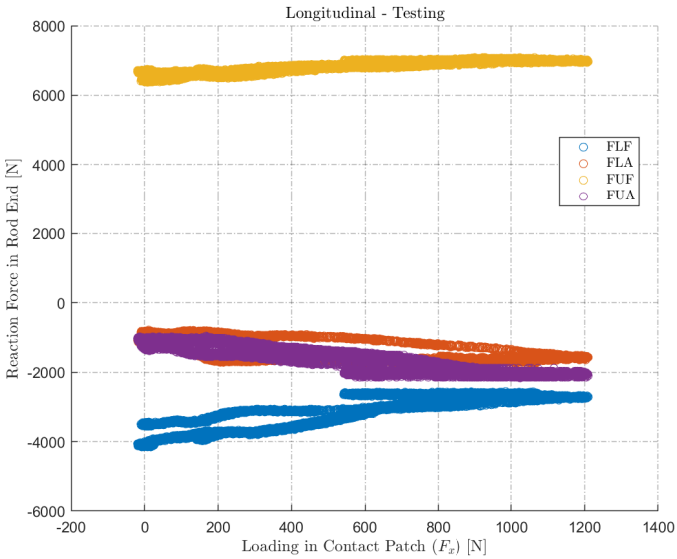

Figure 4.20

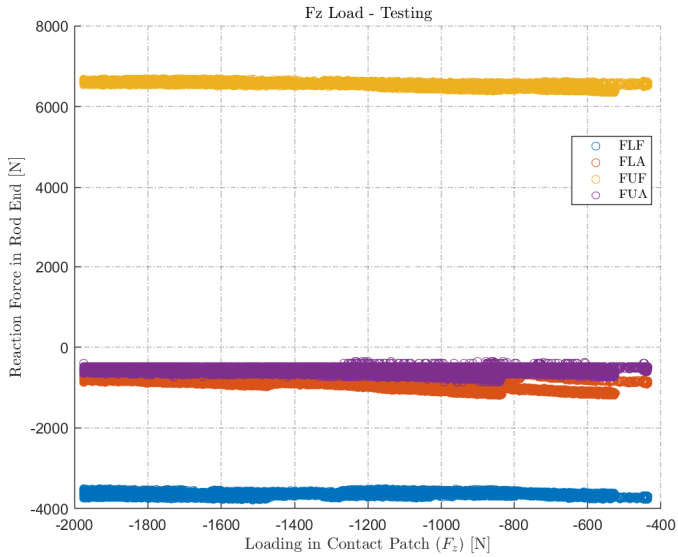

Figure 4.21

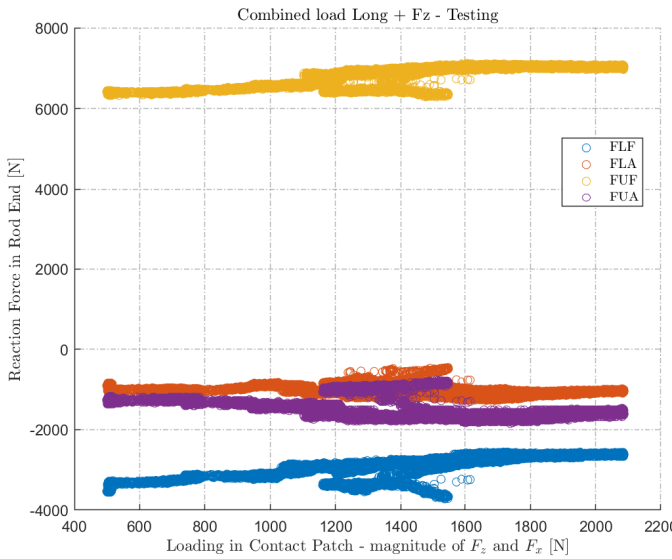

Figure 4.22: Combined load case, observing the magnitude of the applied load.

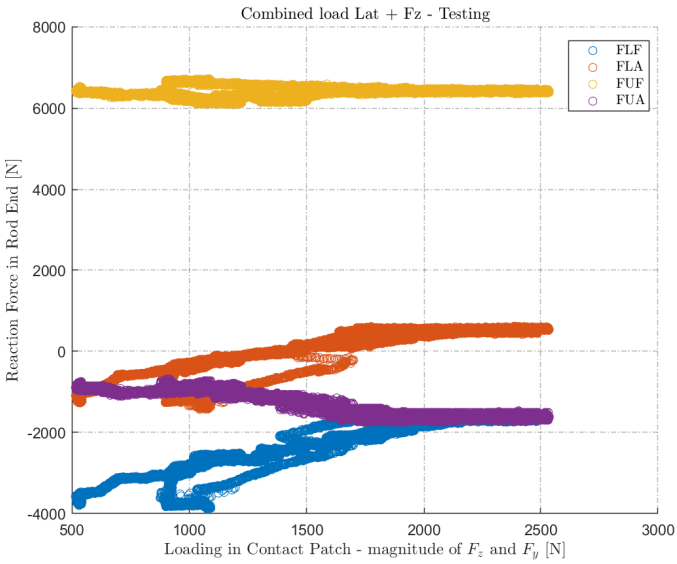

Figure 4.23: Combined load case, observing the magnitude of the applied load.

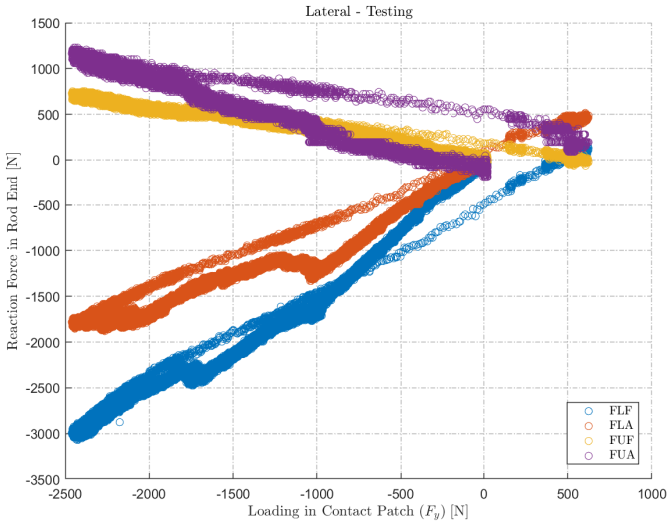

Figure 4.24

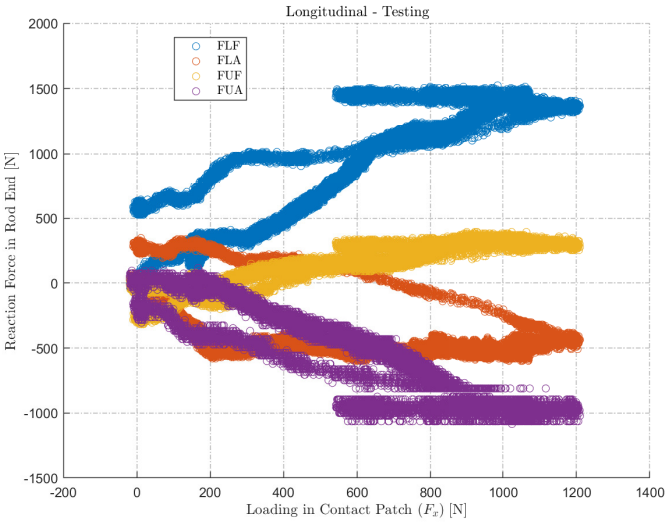

Figure 4.25

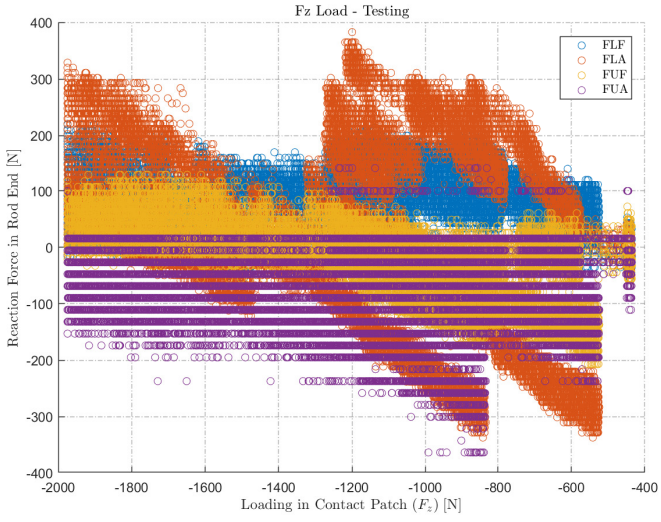

Figure 4.26

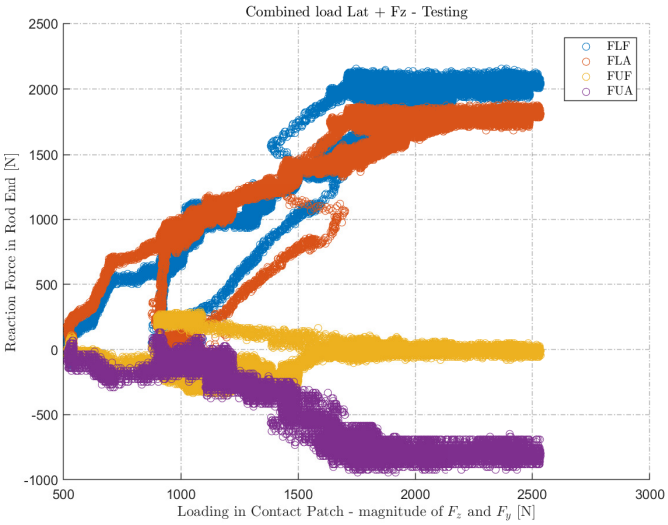

Figure 4.27: Combined load case, observing the magnitude of the applied load.

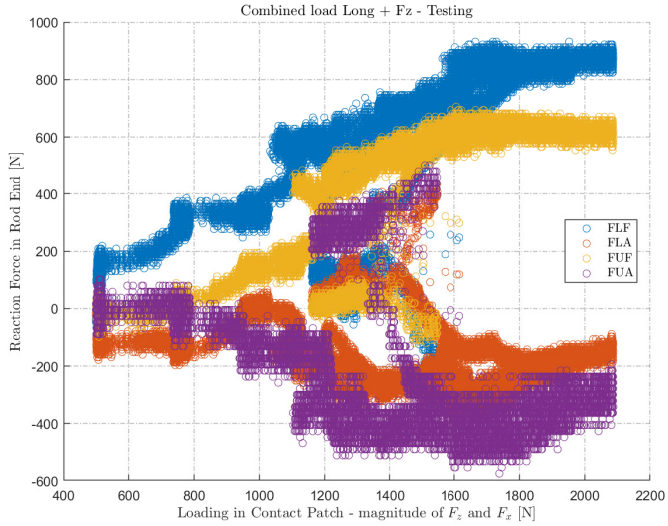

Figure 4.28: Combined load case, observing the magnitude of the applied load.

4.7 Testing Versus The Abaqus Models

In this section, only the corrected result (subsection 4.6.1) will be compared. However, an overall overview can be found in Appendix H, specifically in section H.7/subsection H.7.1.

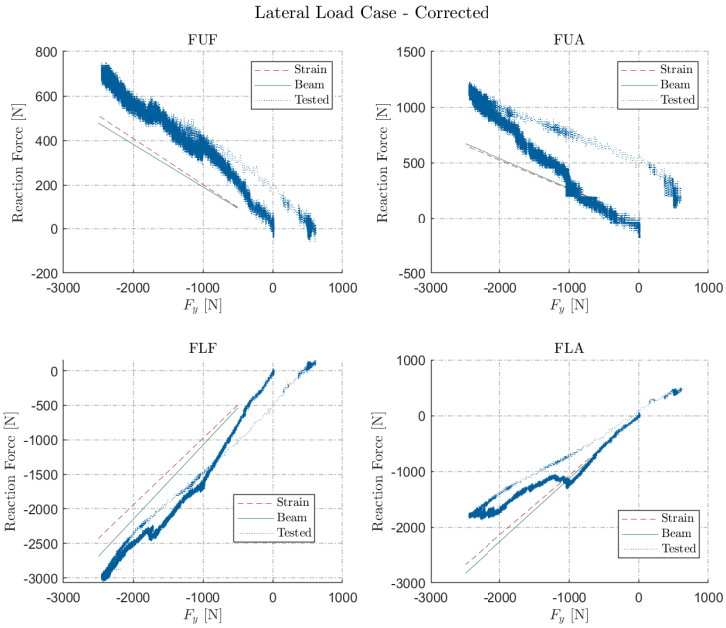

Figure 4.29: Lateral load case.

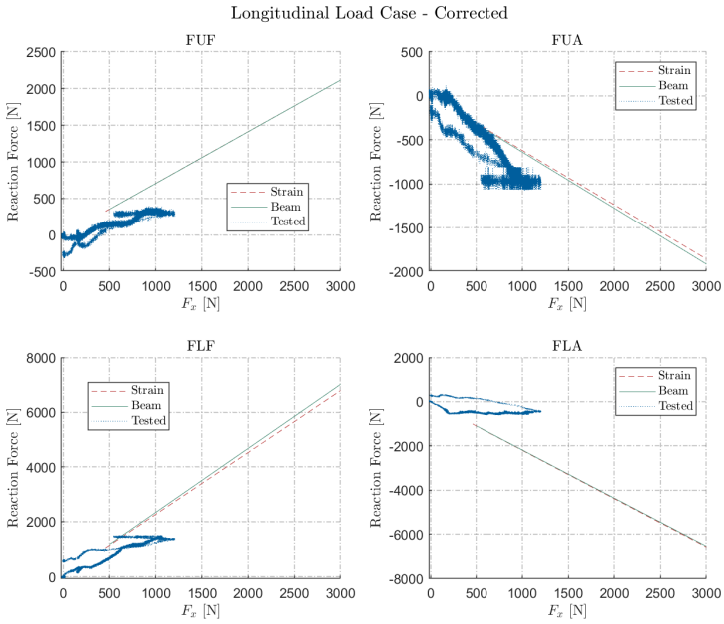

Figure 4.30: Longitudinal load case.

4.7.1 Comparing Reaction Forces pr Load

Due to the linearity of the results in the rigid beam model and the assembled strain model, a linear regression was utilised, calculating the reaction forces as a function of the applied load. Furthermore, the maxima for each rod during each tested load case were found. Then the corresponding load for when it occurred, both F_z and F_x/F_y. If it was a singular load case (lateral, longitudinal or vertical), the force component in question was used. If it was a combined case, the magnitude was used ($\|[F_x \quad F_y \quad F_z]\|$). This load was then used in the linear regression model of the reaction forces. Using

$$Diff = tested - model \tag{4.1}$$

and

$$Diff = \frac{tested - model}{tested} \times 100\% \tag{4.2}$$

Results can be seen in Figure 4.36 with the differences in Newton. In Figure 4.37 shows the same results, only shown with percentage difference.

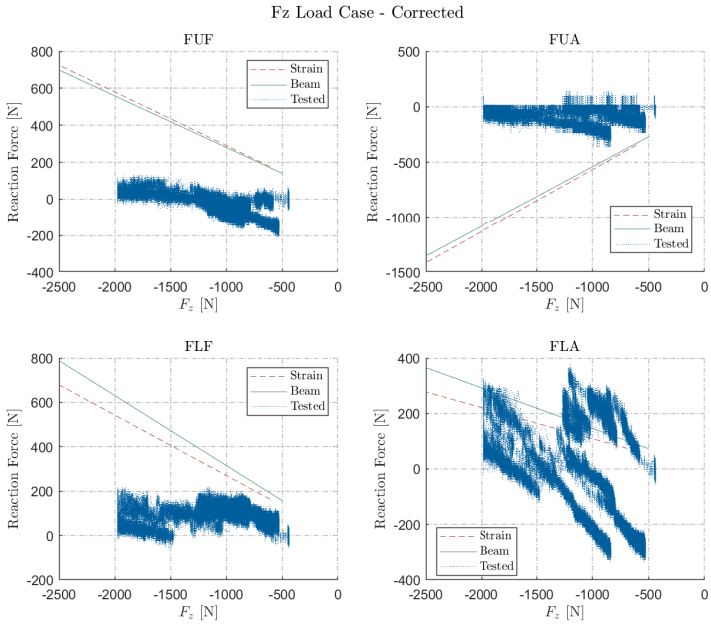

Figure 4.31: Vertical load case.

This data can be summarised into Table 4.4:

Extrema Values (%)	Corresponding Reaction Force [N]	Rod	Load Case
-427.6	-1854	FLA	Longitudinal + F_z
12.21	231.1	FLA	Lateral + F_z
361.7	-2197	FLA	Longitudinal

Table 4.4: Overview of the extrema values between the simulation models and the test. 12.21 was included due to being closest to the zero line.

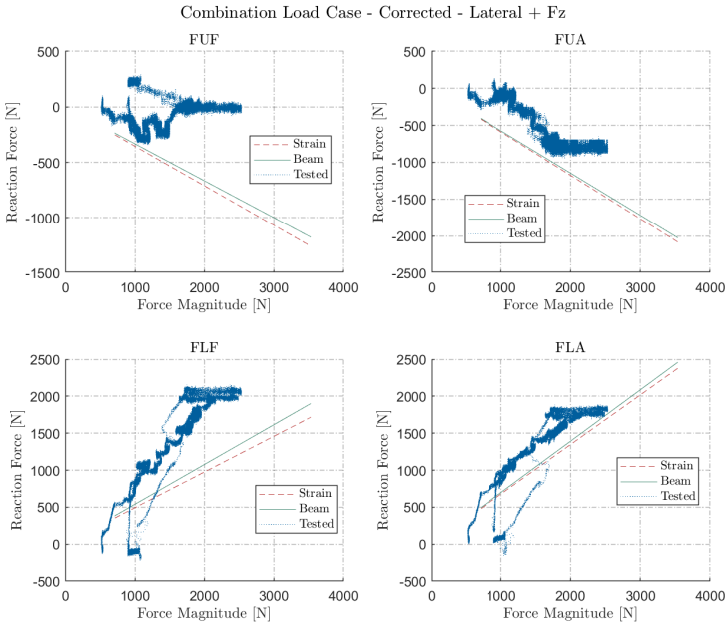

Figure 4.32: Combined load case, lateral and F_z.

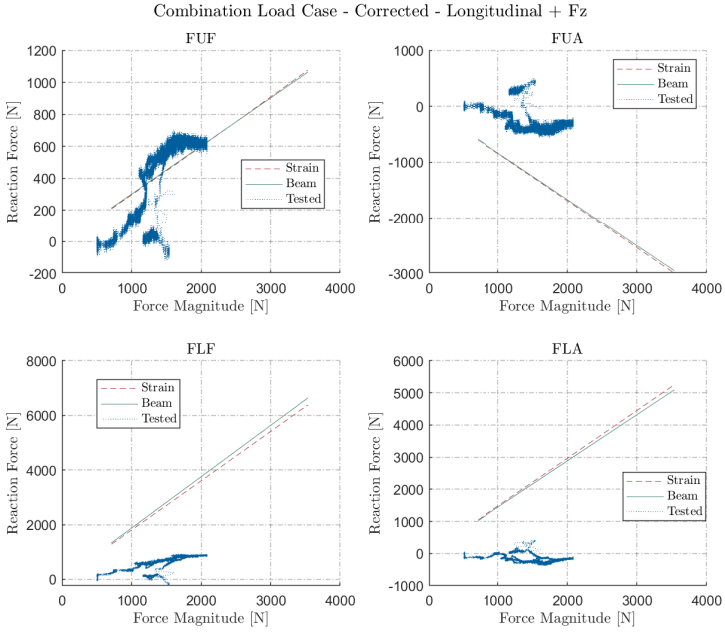

Figure 4.33: Combined load case, longitudinal and F_z.

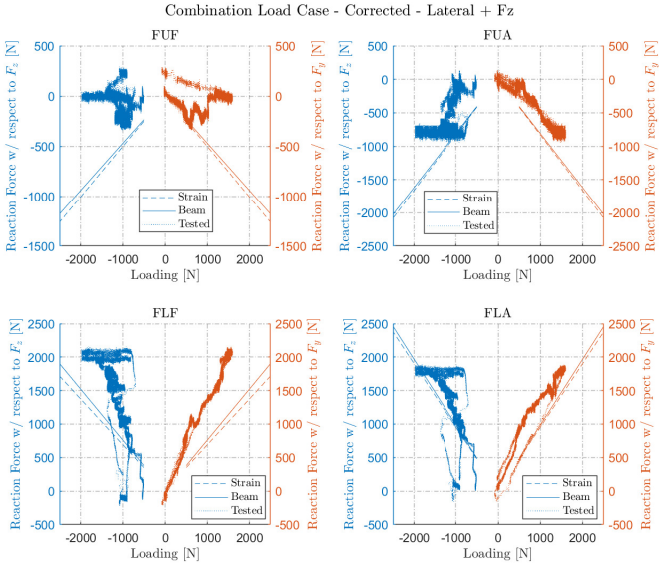

Figure 4.34: Combined load case, decomposed, lateral and F_z.

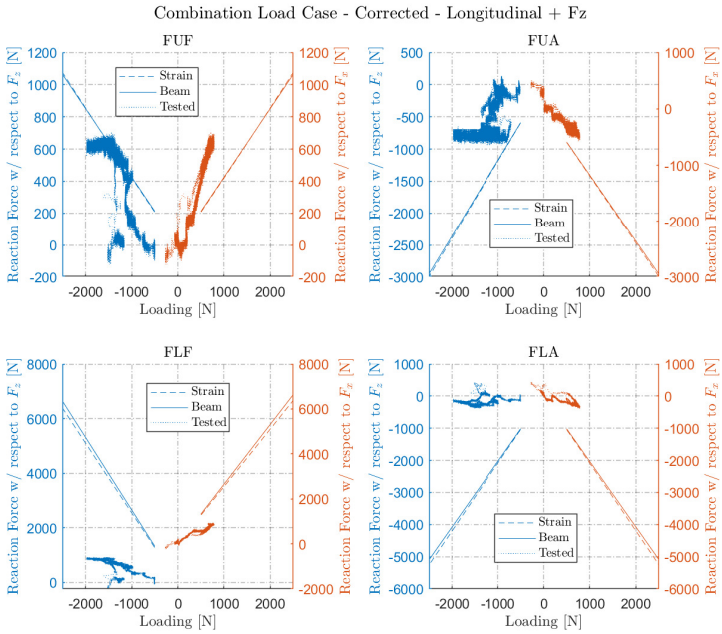

Figure 4.35: Combined load case, decomposed, longitudinal and F_z.

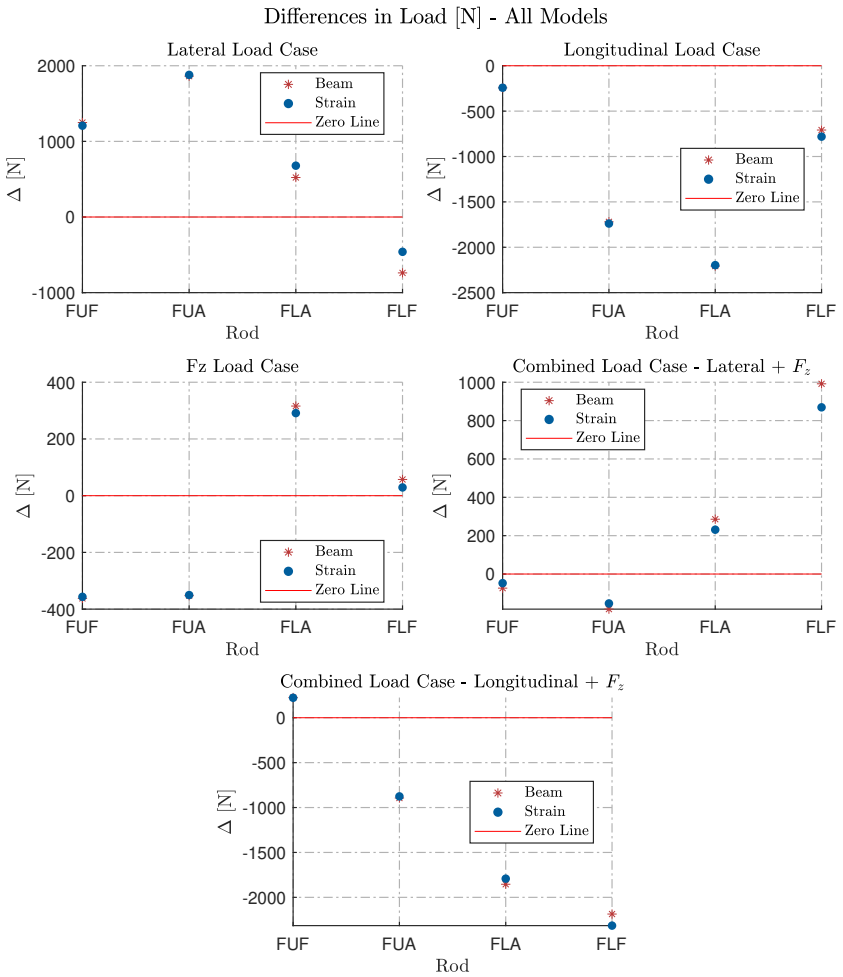

Figure 4.36: Difference with linear regression models. Difference in Newton.

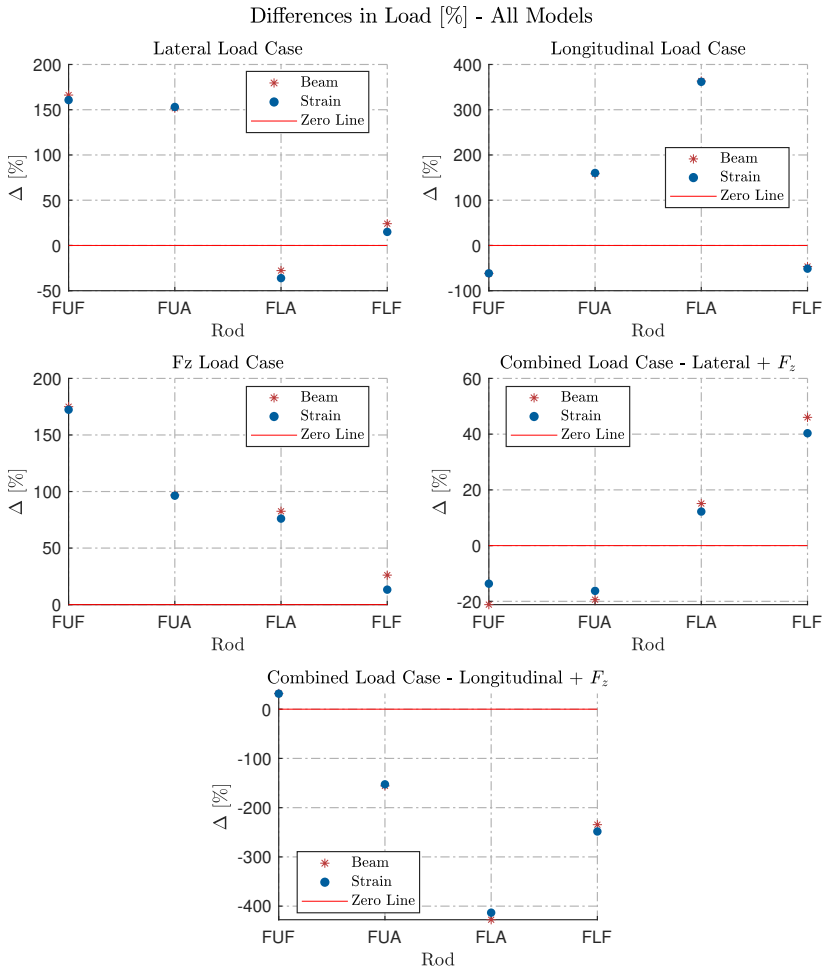

Figure 4.37: Difference with linear regression models. Difference in percent.

Chapter 5

Discussion

5.1 Discussion Regarding Setup of FEA-models

Due to the lack of information from 2020, one can only assume what the layup was. What is considered the most likely, is the layup used in 2019. The order sent to the producers is found in Appendix D.

The reaction forces in the nodes were probed out manually. In hindsight, this process had been more efficient by assigning these reference points to sets, for then to create a new field output, extracting Reaction Force(s) (RF) from the reference point-sets. However, the gain in efficiency would only save time during post-processing and is equal for both models. One could argue that the assembled model would take a longer time due to all the other nodes around the point of interest, but that discussion will not be taken further in this thesis.

5.1.1 Setup Time

For the subsection 3.1.1, utilising the build-in *macro manager* feature in Abaqus, recording a macro, is very efficient approach. Here, the reference points are entered manually from CAD data. The next step is to create and apply the correct connector assignment. The macro makes setting up the model quick when repeated later. Any changes in the suspension pick-up points are fixed by going into the macro-code and editing the definition of the reference point. Since this reference point keeps its name, and that point defines the

wire definitions (for the connectors), nothing else should be affected.

As mentioned in subsection 3.1.2: *The model requires the suspension pick-up points, connector assignments for the upright, and all*[1] *the components in the suspension.* If one were to use the macro manager as in the rigid beam model, the application would be limited due to the following reasons:

- Modified parts would have surfaces switched; thus, the contact surface would not be correct.
- The lengths of the A-arm rods are dependent on the length between the bonding surfaces of the angle locks and rod ends. This is subject to change due to spacing between rods, fillets, etc.
- Repeated, common parts, like the bearings in the rod ends, are mated in the assembly, utilising the surfaces of the angle lock to ensure concentricity.
- Rod layout may be subject to changes.

The first point is fixable by assigning surface sets and using these in the definitions of contacts; thus, only re-assigning the surface sets is necessary. The second point can be fixed by changing the extrude parameter value in the code. This value is taken from CAD, so not entirely automated. The third point may be solved by using self-made coordinate systems (CSYS) in parts. This has not been tried in the model, but from the author's previous experiences, Abaqus does not like using *assembly* features to mate *part* features. The following mating/constraint sequence to ensure perfect positioning should be doable because nodes and reference points are not changing. The fourth and last point is solved by modifying the macro code: adding another layer of composites.

That means all the "problems" are fixable. However, they do take time to set up. They are changed in both the CAE environment and the macro script.

5.1.2 Run-time

As mentioned in the introduction in chapter 4, the rigid beam model took around 2 minutes to run. The assembled strain model took 5 hours. By multiplying the run-time by the number of CPUs, one gets the CPU hours used in each process. The number for the rigid beam model is 0.033 CPU hours, while for the assembled strain model, the number is 80

[1] with exceptions, like spacers, jam nuts, and push rod shim bolts

CPU hours. That is over 2400 times more CPU hours than the rigid beam model. More effort could have been made to improve the model, such as mesh convergence, step-setup such as *nlgeom*, and contact definition.

5.2 Discussion Regarding Results - FEA-Models

Figure 4.16 shows the difference in reaction forces for all the front left suspension members. This graph shows that the beam model is more conservative overall than the assembled strain model. Some rods are over-estimated throughout the models, and some are under-estimated in the beam model. However, from comparing Table 4.1 and Table 4.2, one can see that the beam model is only underestimating one peak-loaded rod: the FUA-rod during the combined load step with longitudinal and Fz loading.

Looking at all the results in Appendix H, the deficit in some rods are, by percentage, quite substantial - up to 65% (Figure H.4b). These numbers suggest that the models would yield different results when subject to the load cases from the tire contact patch.
Also, note the differences in the energy plots: Where the beam/links-model has a minuscule amount of energy, 10^{-9}, the assembled model is in the range of 3×10^3. For the latter model, energy is converted into several forms of energy, such as ALLCCE, ALLCCSD, ALLCCSDT, etc. These energy states are minor, with a magnitude of < 10, compared to the external work and strain energy. External work and strain energy are in the magnitude of around 3×10^3. The similarities make sense as the distance moved by the rigid beam model is in the magnitude of 10^{-12} which is approximately zero; thus, the work done is also approximately zero (Equation 2.5.1). Compared to the assembled strain model, which has displacements on pick-up points of roughly 1.6mm. The displacement, which is due to the system's compliance, might also be why these models do not correspond, as these changes will alter the geometry of the suspension.

It is also evident that the *ETOTAL* is not constant, as it should have been[15] hence the model shows some numerical errors. Calculating the ratio between *ETOTAL* and *ALLWK*, a value which should not exceed 1%, shows a maximum ratio of 3.38%. Some discussions suggest a ratio between all kinematic and internal energies could be up to 5% and still be satisfactory [24].

From Table 4.3, it is evident that the beam model, when first underestimating, is of a magnitude significantly lower than vice versa: the strain model underestimates the peak tie load with 48.6%, whilst the most significant error for the beam model is 1.5% (FUA). It is consensus about which load cases are the most demanding for each rod.

Another case that could explain the difference between the two models is the displacement: Looking at Figure 4.5, observing over $1.5mm$ maxima displacement in the contact patch and approximately $1mm$ in the ball joint points. These displacements will alter the geometry of the suspension and thus might explain the differences observed in this comparison.

Note: A last minute attempt to solve the mystery resulted in the mystery remaining. A simulation of the rigid beam model with displaced nodes was sat up. The load case was the lateral load case, and the displacement was taken from the assembled strain model in the same load case. The results are concluding: the deficit is still there. Not to quantify, but to qualify.

5.3 Discussion Regarding Setup - Physical Testing

One uncertainty is the bonding process and its quality. Since the strain gauge is dependent on moving with the rod end, good bonding with good adherence is of great importance. One of the strain gauges loosened during one bonding process and had to be re-done. There is also play in the suspension system that is worth noting, both in the A-arms and the actuator.

5.3.1 Calibration of the Strain Gauges

The calibration was done in-house with the help of an engine crane[25] and a crane weight [26]. The crane had minor pressure leakages/loss; therefore maintaining a constant load proved difficult. During the initial calibrations, the calibration proved to be off by around 1%: 2kg deficit on 212 kg. An improved method was utilised on the latter two calibrations: Measuring the average voltage output over an average loading. Measuring average versus average yielded improved measures, having an offset of 0.1% and 0.5%.

5.3.2 The Geometry

Due to the new damper setup on Aurora, with roll-heave decoupled suspension mentioned in section 2.3, the system is over-defined when fully constrained with four pick-up points and only two degrees of freedom. Thus, it is difficult to validate in which state the car was in when the test was conducted.

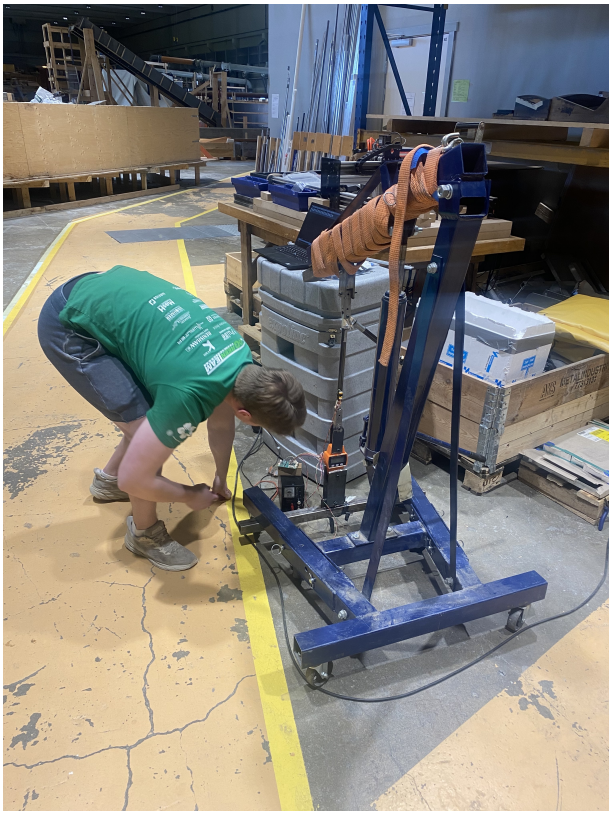

Figure 5.1: Calibration process

5.3.3 The Supporting Frame

Initially, the test was planned to be performed on the 2021 car, Luna. Due to the possibilities mentioned in section 3.2, a late switch to test on Aurora was made. This switch was not investigated adequately enough; thus, the supporting frames proved to be significantly off: The front end of the monocoque was raised this season to yield better aerodynamic performance. As a consequence, the rear supporting frame had to be raised too. The raising was performed by inserting $10mm$ aluminium plates, previously used as suspension bonding fixtures for the last three seasons. The pragmatic approach proved insufficient, and the frames were still skewed. Because the aluminium plates were underneath the rear supporting frame, only the front frame was bolted to the floor. When unloading the vehicle at the final load step, it made an evident noise, suggesting it had been on tilt whilst being subject to loading.

5.3.4 The Actuator(s)

The sub-actuator used for vertical loading (F_z)[27] was of rather poor quality: constantly losing the pressure being the most notable. This is evident in the data (Figure H.7b and Figure H.10b) as the loading is moving up and down. The pressure loss disabled the possibility of steady loading, and unloading the main actuator when resting. The latter can be seen in Figure H.6b where the F_z is under a constant, stable loading.

The sub-actuator was also limited to $2000kg$ (approximately $2kN$); this can be seen in the data as the loading curve flattens. The flattened curve could be due to the gainer/amplifier reaching saturation or the sub-actuator being physically unable to do any higher. That discussion will not be brought forth.

During the longitudinal loading, the actuator-to-hub fixture proved so loose that it rotated a few degrees. The rotation, added with the compliance of the suspension, resulted in the fixture mentioned above colliding with the actuator itself, see Figure 5.2.

Worth noting is how skewed the actuator appears to be when loading in the longitudinal direction, see Figure 5.3'

5.3.5 Reflection Upon the missing measurement points

Missing measurements in the push and tie suspension member are unfortunate, especially during the load cases where these are of great interest (vertical loading and lateral loading). The greatest loss was lack of measurements during the vertical loading, as few other

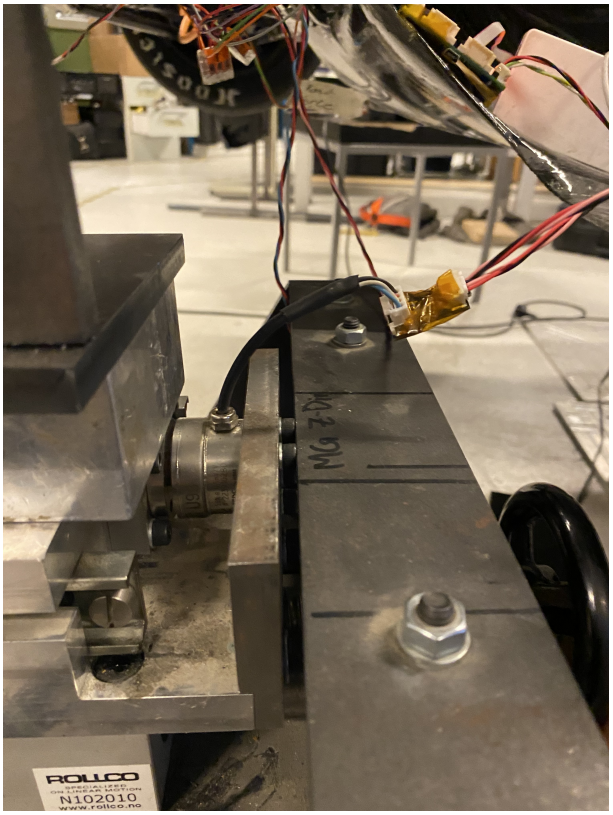

Figure 5.2: Collision during longitudinal loading

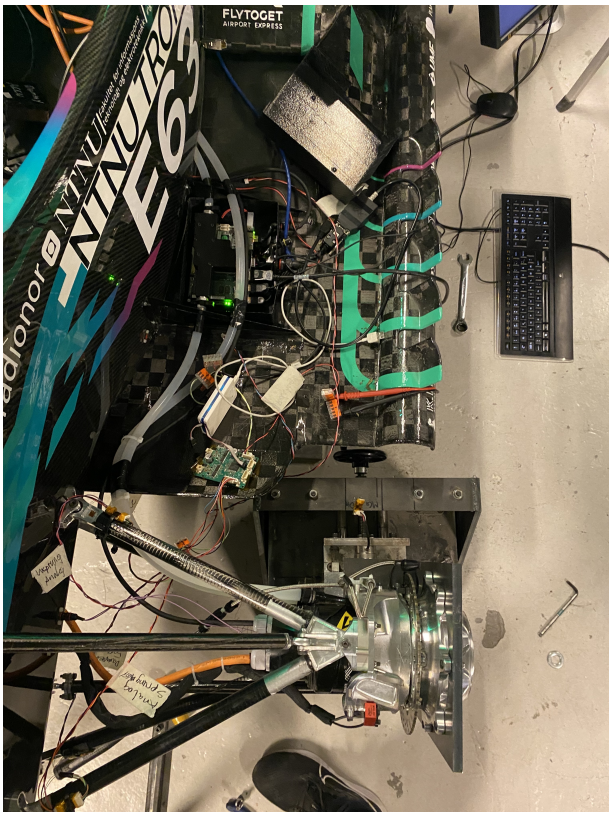

Figure 5.3: The actuator mounted on the suspension. Longitudinal loading scenario. Seen from above.

suspension members have a significant loading (Figure H.1c, Figure H.2c, Figure H.12c in Appendix H).

5.4 Discussion Regarding Results - Physical Testing

As can be seen in Appendix H, section H.5, some of the measurements seemed quite whimsical, especially FUF which had a reading of over $6000N$ prior to load application - however, the trends where there, which is seen throughout the results. Calibrating the results by setting the base condition (prior to loading, that is) to 0 makes the results more comprehensive.

Due to the lack of push rod measurements, the vertical loading scenario can be classified as the least valuable test of the one-directional ones (lateral, longitudinal, and vertical). The combined cases will be discussed in section 5.5.

5.5 Discussion Regarding Comparisons - Testing and Abaqus Models

The combined loading scenarios (lateral + F_z, and longitudinal + F_z) yield a problem when comparing them to a linear regressed model based on Abaqus' simulations: The magnitude of the load applied to the physical suspension might have different decomposed forces than the Abaqus load. The Abaqus load is 1:1, meaning the magnitude is the square root of 2 times the applied load. For the physical testing, this is not the case, as seen in Appendix H, Figure H.8b and Figure H.9b. The different directions affect the reaction forces, which is evident when comparing the different one-directional load cases. Hence, these load cases are not as comparable as desired.

Chapter 6

Conclusion and Future Work

6.1 Conclusion

There is no clear explanation as to why the models gave such different results was found: There are no warnings from Abaqus regarding solver problems, a common message during iterations as these connectors tended to over-constrain between upright and A-arms. A few plausibilities would be material damping, displacement caused deviations, energy dissipation due to contact stabilisation(s), or propagation caused by the displacement of other parts (compliance). Nevertheless, it is safe to say that the rigid beam model is the most conservative. Looking at Table 4.3, it is evident that a minor safety factor of 1.0153 would be substantial enough to cover the deficit/unevenness. The simulation is by far the quickest and the least computational demanding. The model also provides the service of adding parts by parts to check them in the load cases. Checking parts is also true for the assembled strain model; however, the computing time does not justify the quality of the results.

Even though the results yield the camber and toe compliance directly from the suspension assembly, this can be done by simply simulating them part by part or sub-assembly by sub-assembly. Using the results to model the system as springs in parallel and series, as briefly mentioned in subsection 2.3.2.

When comparing the models to the testing, a deviation between **-427.6%** and **361.7%**, with the nearest correlation being at **12.21%**, was found. As discussed in section 5.5, the

combined loading is misleading in these comparisons, in which we find the greatest, as well as the smallest, deficit at -427.6% and 12.21% respectively. By ignoring these, the greatest/smallest deficits are **-61.56%** and **13.25%**, numbers not found in the combined load cases.

As further discussed in chapter 5, there is reason to believe the testing was performed under severe sub-optimal conditions.

6.2 Future Work

Further investigation on why the simulations yielded different results should be looked further into, focusing on the theories behind it. Running different layups on the rods also yielded different results, supporting the initial statement.

The supporting frames should be (and should have been) re-made and tailored for Aurora. Fixing the frames allows them to be bolted more securely onto the ground, avoiding the car moving/rotating.

The play in the suspension rod ends should also be assessed; the play was of such magnitude that it was visible through a cellphone video.

It should also be looked into making a better strain gauge design for the push rod, if not looking into a fitting load cell. Aurora has load cells installed on the dampers; it is outside the scope of this thesis to discuss these, but an analysis of how much more data the push rod strain gauge would yield needs to be considered. Changing from a linear strain gauge to a rosette could be attractive, as a rosette strain gauge would enable separating strain from axial displacement versus bending displacement [28].

Performing the same test on the rear suspension should be done. Driving with the strain gauged front suspension should also be performed. With this running, in collaboration with van der Lee's models[29] could potentially yield a better understanding of the tires and how different parameters such as camber and toe affect the loads generated from the tires. Meaning we could reassemble a tire model ourselves. This testing and data acquisition would require extensive running and post-running analysis.

Bibliography

[1] Sondre Audal. Estimation Of Pneumatic Trail On Tyres Fitted On A Formula Student Race Car. 2021.

[2] Technia. Simuleon FEA Blog, Abaqus python scripting: how difficult is it? https://info.simuleon.com/blog/abaqus-python-scripting-how-difficult-is-it, 2021. Accessed: 2022.03.20.

[3] Torbjørn Smith. Development of a Quasi Steady State Lap Time Simulator for a Formula Student Racing Team. Technical report, Norwegian University of Science and Technology, Trondheim, 10 2021.

[4] Kristoffer Haugland. Validation of Finite Element Analysis using strain gauges, of the suspension system of a Formula student car. 2018.

[5] M. Autio, H. Parviainen, and A. Pramila. Accuracy of the finite element method in analyzing laminated plate and pipe structures. *Mechanics of Composite Materials*, 28(3), 1992. ISSN 0191-5665. doi: 10.1007/BF00604915.

[6] Suspension System Design for Revolve NTNU Project Thesis author = Ramsdal, Ole Andreas, year = 2017,.

[7] Ole Andreas Ramsdal. Suspension System Design for Revolve NTNU Master Thesis. 2018.

[8] Mercedes-Benz. The new Mercedes-AMG ONE: Formula 1 technology for the road. https://group-media.

mercedes-benz.com/marsMediaSite/en/instance/ko/The-new-Mercedes-AMG-ONE-Formula-1-technology-for-the-road.xhtml?oid=53396743, 2022. Accessed: 2022.03.20.

[9] KYLE.ENGINEERS. Mercedes Project ONE Suspension - Explanation and Analysis. https://www.youtube.com/watch?v=8js55jE2da0&ab_channel=KYLE.ENGINEERS, 2017. Accessed: 2022.03.20.

[10] Greenteam Uni Stuttgart. E0711-8. https://www.greenteam-stuttgart.de/fahrzeuge/e0711-8/, 2017. Accessed: 2022.03.20.

[11] Greenteam Uni Stuttgart. E0711-9. https://www.greenteam-stuttgart.de/fahrzeuge/e0711-9/, 2018. Accessed: 2022.03.20.

[12] TU Fast Racing Team. eb020. https://tufast-racingteam.de/rennwagen/eb020/, 2020. Accessed: 2022.03.20.

[13] William F Milliken and Douglas L Milliken. *Race Car Vehicle Dynamics*. SAE International, Warrendale, PA, 10 1994. ISBN 978-1-56091-526-3.

[14] Ola Flåskjer. Topology optimization and dimensioning of a subtractively manufactured Formula Student upright. 2021.

[15] Dassault Systèmes Simulia Corp. *Energy Balance*, 2017. URL https://classes.engineering.wustl.edu/2009/spring/mase5513/abaqus/docs/v6.6/books/gsx/default.htm?startat=ch03s07.html.

[16] R. Haghani. Finite element modelling of adhesive bonds joining fibre-reinforced polymer (frp) composites to steel, 2014.

[17] All About Circuits. All About Circuits: Strain Gauges. https://www.allaboutcircuits.com/textbook/direct-current/chpt-9/strain-gauges/, 2021. Accessed: 2022.05.13.

[18] Dassault Systèmes Simulia Corp. *Link Connector*, 2012. URL https://abaqus-docs.mit.edu/2017/English/SIMACAEELMRefMap/simaelm-c-connectiontypedesc-link.htm.

[19] Dassault Systèmes Simulia Corp. *Beam Connector*, 2012. URL https://abaqus-docs.mit.edu/2017/English/SIMACAEELMRefMap/simaelm-c-connectiontypedesc-beam.htm.

[20] Jerome Montgomery. Boundary condition influences on shank stress in 3d solid bolt simulation, 2012.

[21] Gustavo Tumialan, Nestore Galati, and Antonio Nanni. Structural testing, 2014. URL www.STRUCTUREmag.org.

[22] Seif. M. Osman, Ebtisam H. Hasan, H. M. El-Hakeem, R.M. Rashad, and F. Kouta. Conceptual design of multi-capacity load cell. EDP Sciences, 10 2013. ISBN 978-2-7598-1089-5. doi: 10.1051/metrology/201303002.

[23] Formula Student Germany. *FS-Rules 2021 V1.0.pdf*, 2021. URL https://www.formulastudent.de/fsg/rules/. Accessed: 2021.06.20.

[24] Youming Chen, Raj Das, and Mark Battley. Effects of cell size and cell wall thickness variations on the strength of closed-cell foams. *International Journal of Engineering Science*, 120:220–240, 11 2017. ISSN 00207225. doi: 10.1016/j.ijengsci.2017.08.006.

[25] Biltema. Motorkran 2000 kg. https://www.biltema.no/bil---mc/verkstedsutstyr/lofteutstyr/motorstativ/motorkran-2000-kg-2000045389, 2021. Accessed: 2022.06.09.

[26] Biltema. Digital hengevekt. https://www.biltema.no/fritid/jakt/viltvekter/digital-hengevekt-2000034665, 2021. Accessed: 2022.06.09.

[27] Biltema. Hydraulisk jekk, 2000 kg. https://www.biltema.no/bil---mc/verkstedsutstyr/lofteutstyr/jekker/hydraulisk-jekk-2000-kg-2000050407, 2021. Accessed: 2022.06.09.

[28] Strain Gauge Rosette, 2017. URL https://www.hbm.com/en/7330/what-is-a-strain-gauge-rosette/.

[29] Lars C. M. van der Lee. Online Tyre Parameter Estimation for a 4WD Formula Student Racecar. 2021.

Appendix A

Formula Student Scoring System

Static Events

- **Engineering Design (150 points)**
  The design is presented to judges. Points are scored on solutions, knowledge, and design.
- **Cost (100 points)**
  Points are scored based on cost efficiency and understanding of cost of design.
- **Business Presentation (75 points)**
  The team presents their car a potential investment opportunity and presents a business plan to the judges.

Dynamic Events

- **Acceleration (75 points)**
  75 m straight forward. Tests the vehicle's acceleration.
- **Skid-Pad (75 points)**
  Figure of eight track. Tests the vehicle's steady-state cornering.
- **Autocross (75 points)**
  One lap, approximately one km long. Tests the vehicle's overall capabilities.

- **Endurance (325 points)**
  Approximately 22 km with multiple laps similar to the one during Autocross. Tests the vehicle's overall capabilities and reliability.
- **Efficiency (100 points)**
  From the Endurance run, the car which uses less energy scores the most. Linear slope down to the reminder of finishing teams.

Appendix B

Setup of FEA-Models

B.1 Materials

B.1.1 Aluminium 7075

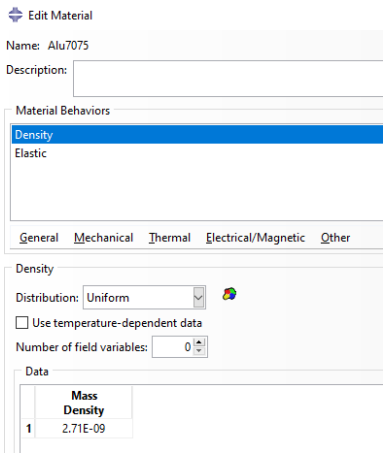

(a) Density of aluminium in tonnes/mm^3

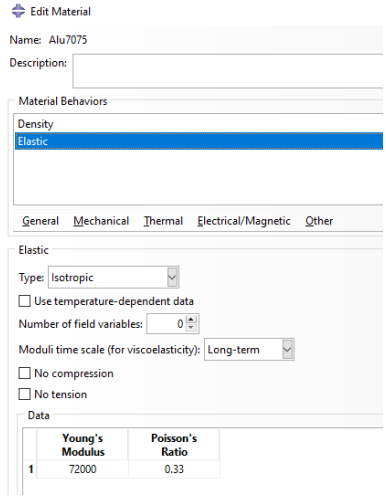

(b) Elasticity of aluminium 7075, in MPa, including Poisson's ratio.

B.1.2 Steel

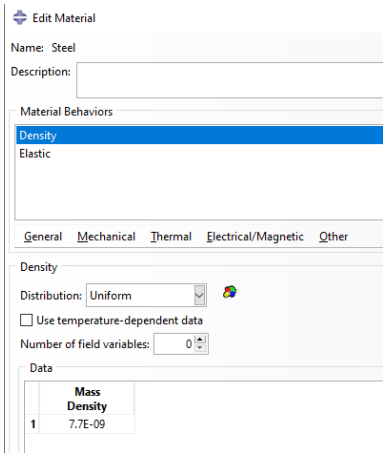

(a) Density of steel in tonnes/mm^3

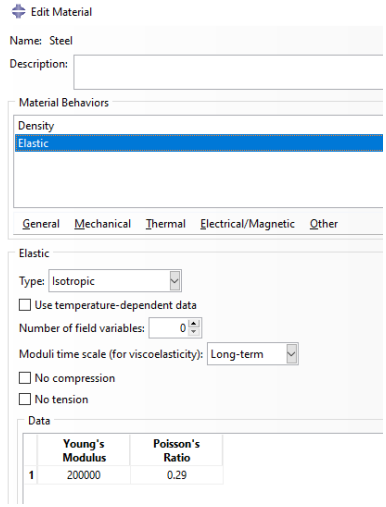

(b) Elasticity of steel, in MPa, including Poisson's ratio.

B.1.3 T700

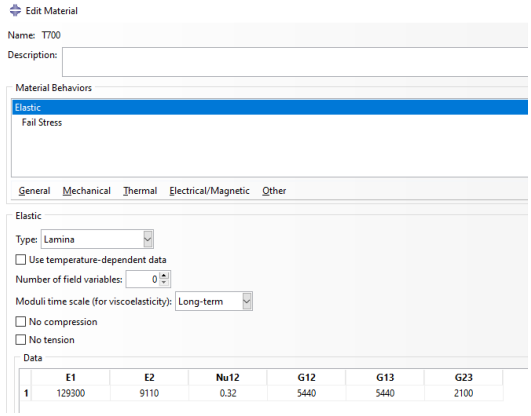

(a) Material properties of the T700 composite.

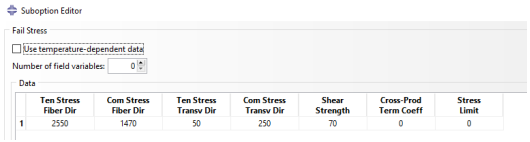

(b) T700 stress failure criteria.

B.2 Parts in FEA

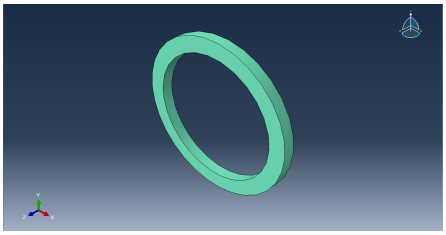

(a) DKR-16, steel material, 98 C3D20R Elements.

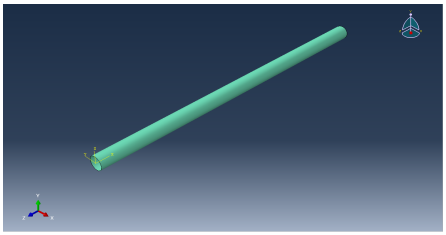

(b) A-Arm(s), T700 CFRP, ten layers, ranging from 2662 to 3454 S4R elements.

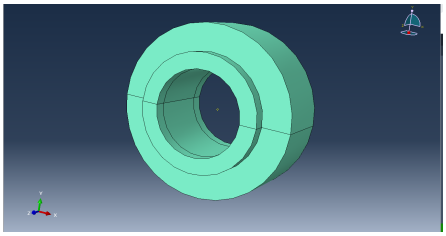

(c) SKF GE 8c dummy, steel material, 986 C3D20R elements.

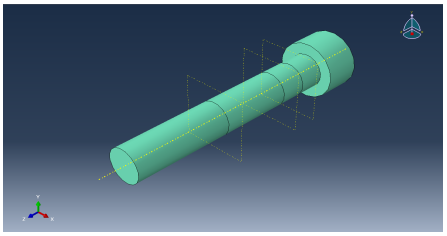

(d) M6 dummy bolt sitting in the push rod, steel material, 1332 C3D8R elements.

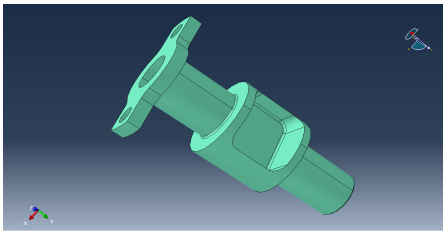

(e) Strain insert for the push rod, aluminium 7075 material, 27'962 C3D10 elements.

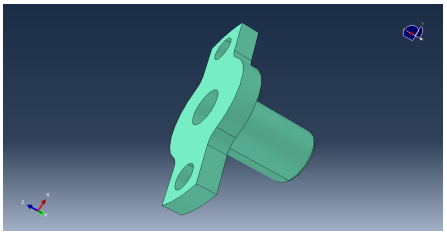

(f) Male part of push rod insert, aluminium 7075 material, 4480 C3D8R elements.

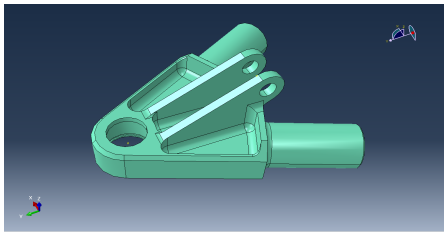

(g) Front Upper (LHS) angle lock, aluminium 7075 material, 27'962 C3D10 elements.

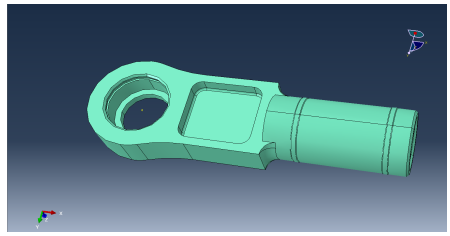

(h) Strain rod end, aluminium 7075 material, 22'782 C3D10 elements.

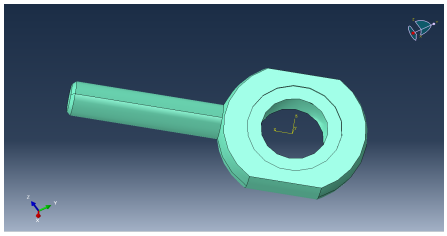

(i) CAD of the SKF SAKB 6F housing, steel material, 6864 C3D10 elements.

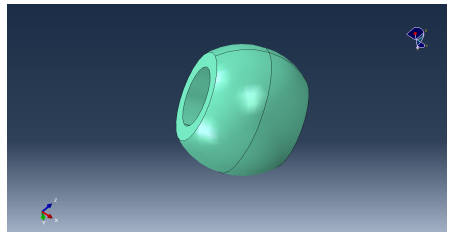

(j) CAD of the SKF SAKB 6F ball, steel material, 252 C3D20R elements.

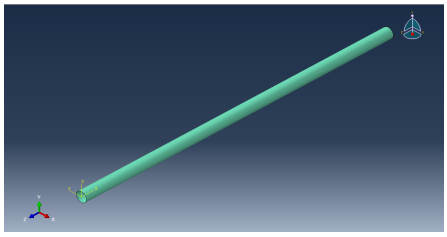

(k) Tie- and push rod, T700 CFRP, five (tie) and six(push) layers, 4642 S4R elements for tie rod, and 4202 for push rod.

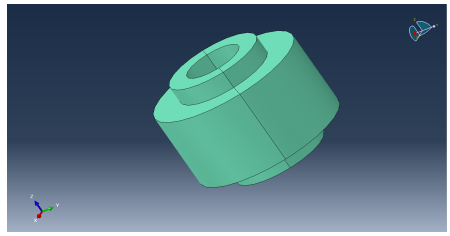

(l) Sarma/SKF XLR 6 dummy, steel material, 1590 C3D20R elements.

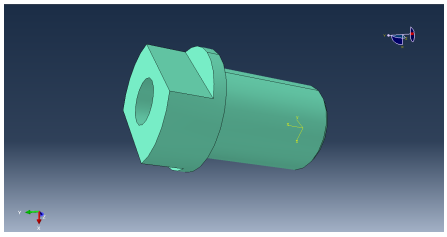

(m) Rod end insert, aluminium 7075 material, 6027 C3D10 elements.

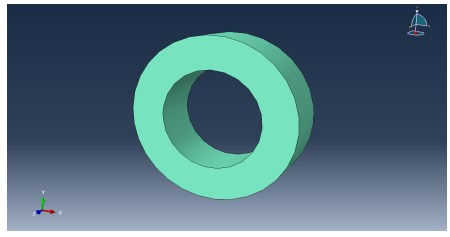

(n) M6 nut, steel material, 76 C3D8R elements.

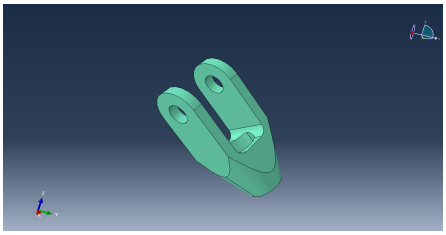

(o) Push rod fork, aluminium 7075 material, 7610 C3D10 elements.

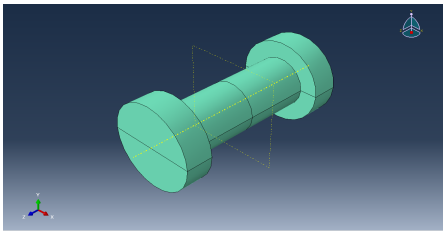

(p) M5 shoulder bolt, steel material, 704 C3D8 elements.

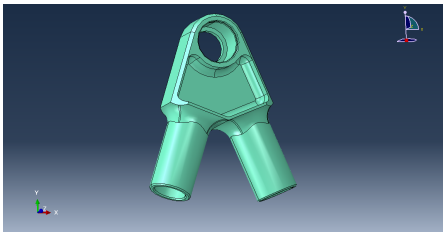

(q) Front Lower Angle Lock, aluminium 7075 material, 18'405 C3D10 elements.

B.3 Interaction Properties

Ignoring subsection B.3.1, the remainder had two similar interaction properties, where the only difference is for *Normal Behavior*: "SS" means the constraint enforcement method is set to "Direct (Standard). Whilst the non-SS has this setting set to "non-linear Penalty (Standard)".

B.3.1 Adhesive

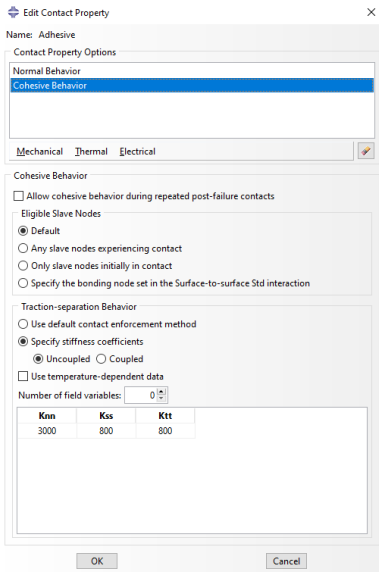

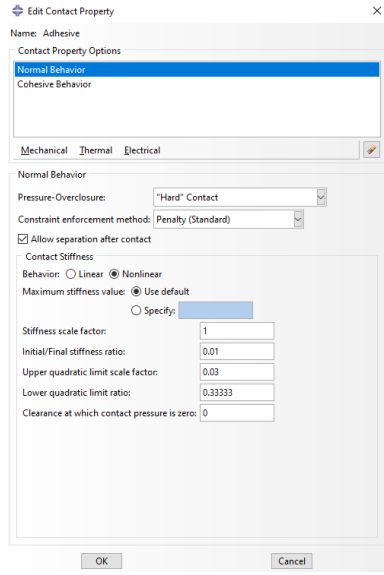

B.3.2 Alu-Steel

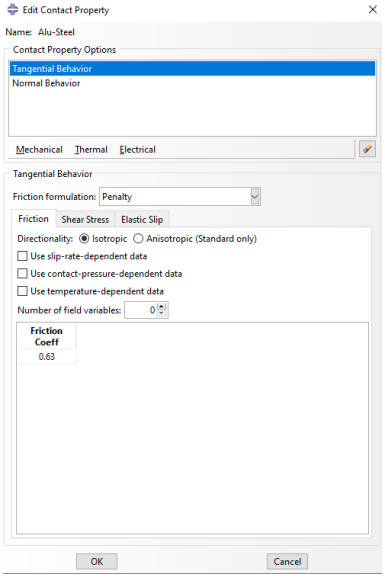

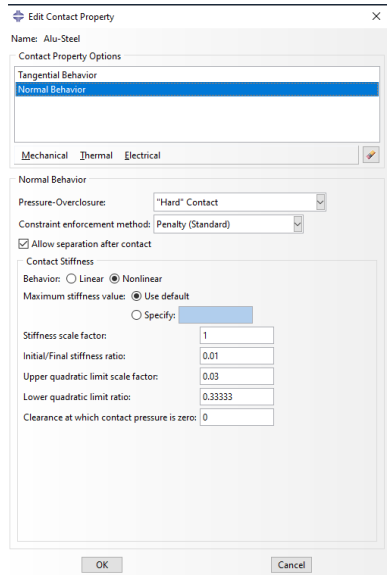

B.3.3 Glider

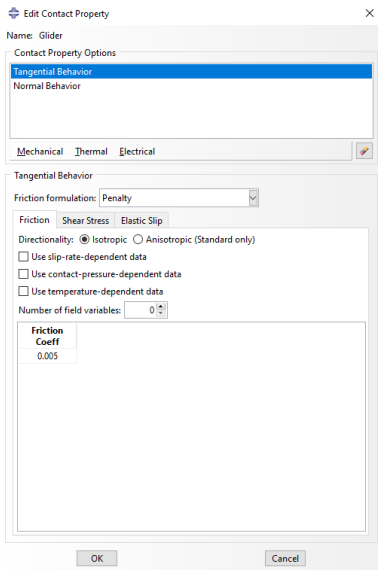

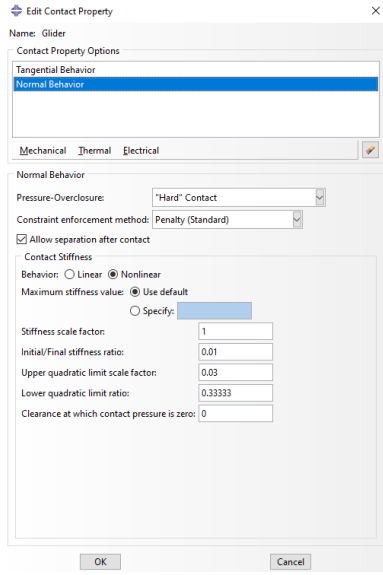

B.4 Interactions

B.4.1 Thread Connections

The SKF SAKB rod ends (Figure B.4i are threaded into an thread insert (Figure B.4m, in both ends of the tie rod. The same is true for the M6 bolt (Figure B.4d) to the M6 nut (Figure B.4n) and the strain insert for the push rod (Figure B.4e). As mentioned in subsection 3.1.2, these threaded connections are modelled as tie constraints.

B.4.2 Adhesive Contact

The A-arms (Figure B.4b are interacting with the strain rod ends (Figure B.4h) and angle lock (Figure B.4g) via the cohesive interaction as described in subsection B.3.1. The sliding is set to small. The same goes for the rod end inserts (Figure B.4m and Figure B.4e) and their corresponding rod (Figure B.4k). The *adjust* is set to 0.25 to allow for wider shell rod, as this parameter proved crucial for buckling strength (section C.5).

B.4.3 Alu-Steel Contacts

All the bolts (Figure B.4p and Figure B.4d), along with the bearings (Figure B.4c and Figure B.4l), have all their contact defined as *Alu-steel*, defined in subsection B.3.2. The

contact of the SKF SAKB 6F ball (Figure B.4j) have the ”SS” definition of the contact. The *adjust* is set to 0.25 here as well, in order for the parts not to loose contact during any stage of the simulation.

B.4.4 Glider Contacts

The SKF SAKB assembly, consisting of the housing and the ball(Figure B.4i and Figure B.4j, respectively), have defined a this as their contact (subsection B.3.3).

B.4.5 Pick-up Points

The pick-up points, which defines the suspension geometry, is coupled to their corresponding bearing with kinematic coupling, locked in all DOFs.

B.5 Steps, Loading and Boundary Conditions

B.5.1 Steps

A new step is created of each load case listed in section 3.4. Between each step, a ”cool down” was introduced in order to set the contact and reaction forces back to zero, before the new load was applied.

B.5.2 Loading

As prescribed in section 3.4, the load is applied with tabular incrementations of 1000 N/s, and applied at the estimated contact patch.

B.5.3 Boundary Conditions

All the suspension pick-points on the monocoque-side is pinned - locked in U1, U2, U3.

B.6 Verification of Established Contact

All the interactions are defined as surface-to-surface in order to ensure full control of the contact properties. To ensure no contact was left out, and the contact was well established, Abaqus’ *CSTATUS* field output was utilized. This allows to check for poor contact through the initial data check, making in an computational effective, as no steps are ran.

Appendix C

Setup of Buckling Models

C.1 Materials, Interaction Properties, and Interactions

These are the same as defined in Appendix B, section B.3 and section B.4. The interactions are only of interest for the corresponding parts in the analysis.

Two reference points were made: one in each pick-up point in the bearings. These are coupled through a kinematic coupling, with all DOFs constrained.

C.2 Parts in FEA

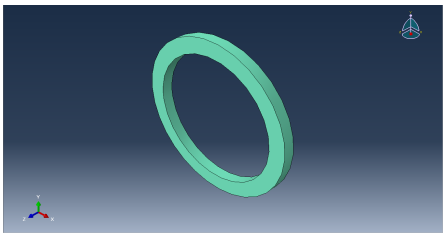

(a) DKR-16, steel material, 468 C3D8R Elements.

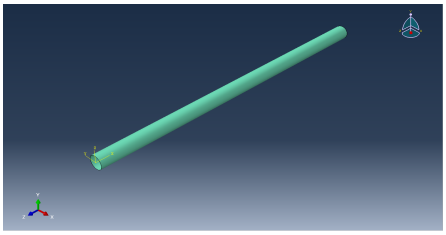

(b) A-Arm, T700 CFRP, ten layers, 18'105 S4R elements.

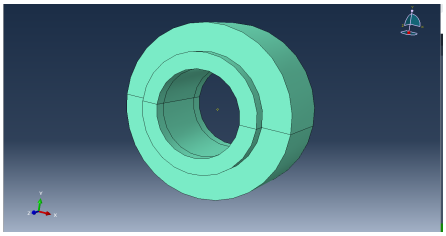

(c) SKF GE 8c dummy, steel material, 540 C3D8R elements.

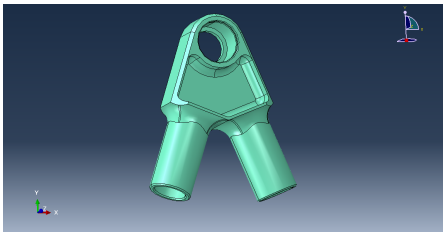

(d) Front Lower Angle Lock, aluminium 7075 material, 13'863 C3D10 elements.

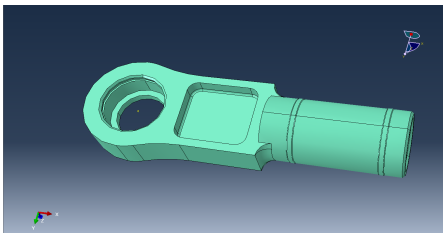

(e) Strain rod end, aluminium 7075 material, 22'951 C3D10 elements.

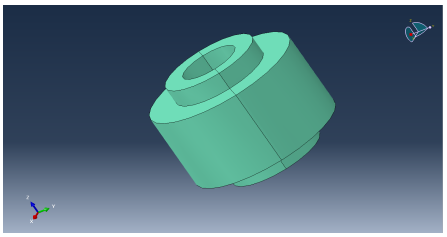

(f) Sarma/SKF XLR 6 dummy, steel material, 1696 C3D8R elements.

C.3 Steps, Loading and Boundary Conditions

C.3.1 Steps

Abaqus' *Linear Perturbation* step, *Buckle*, is used for this analysis.

C.3.2 Boundary Conditions

A coordinate system was made, aligning its X-axis with the centre axis of the rod. In the strain rod end, the corresponding reference point was bounded in U1, U2, U3, and UR1 with respect to the aforementioned coordinate system. In the angle lock, the corresponding reference point was bounded in U2 and U3.

C.3.3 Loading

The load is applied in at the reference point in the angle lock. With a magnitude of 1, in the X-direction of the coordinate system in subsection C.3.2, compressing the assembly. This setup makes the eigenvalue in the post-analysis being the same as the buckling load (buckling load = Eigenvalue $\times$ Applied load).

C.4 Assembly

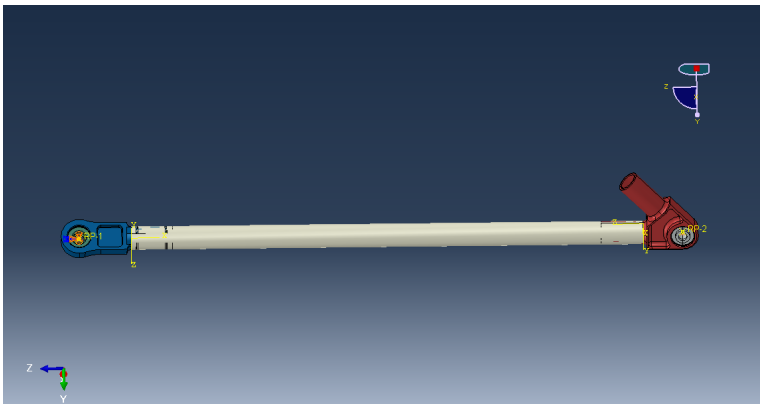

Figure C.2: Buckling assembly.

C.5 Case Study Regarding Diameter & Buckling Load

The simulation was ran with different diameters. The equation for Euler buckling is:

$$P_{cr} = \frac{\pi^2 EI}{L^2} \tag{C.1}$$

where

$$I = \pi(\frac{R+r}{2})^3(R-r) \approx \pi r^3 t \tag{C.2}$$

Combining these two equation yields

$$P_{cr} = \frac{\pi^3 E(\frac{R+r}{2})^3(R-r)}{L^2} \tag{C.3}$$

According to Equation C.5, the buckling load should be depended on the radius to the

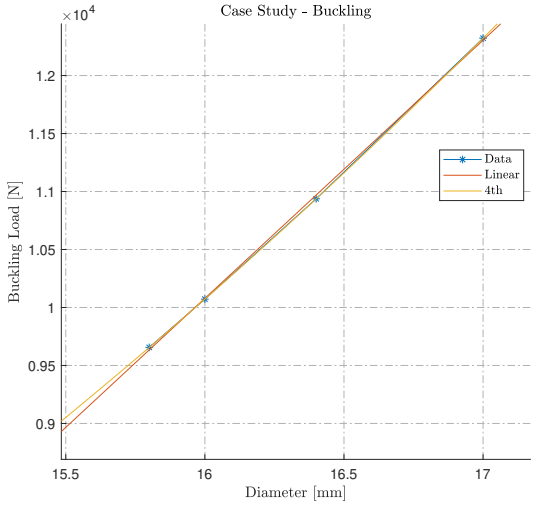

Figure C.3: Results of iterative simulations

fourth power.

This is supported by the findings in Figure C.3. Thus, opting for the correct diameter is crucial.

Appendix D

Rod Order - Revolve NTNU 2019

Production Order 2019 - Revolve NTNU

Lag nr.	Antall rep.	Grader	Bruksområde:	A-armer		
1		Hoop				
2		6		Øi:	16	mm
3		Hoop		Øy:	19.4	mm
4		6		Total Lengde	9	m
5		6				

Lag nr.	Antall rep.	Grader	Bruksområde:	Styresystem		
1	1	Hoop				
2	1	40		Øi:	16	mm
3	1	6		Øy:	20.2	mm
4	1	40		Total Lengde	2	m
5	1	6				

Lag nr.	Antall rep.	Grader	Bruksområde:	Tierod		
1	0.5	Hoop				
2	1	6		Øi:	12	mm
3	1	Hoop		Øy:	15.8	mm
4	1	6		Total Lengde	3	m
5	1	6				

Lag nr.	Antall rep.	Grader	Bruksområde:	Pushrod/FW mounts		
1	0,5	Hoop				
2	1	6		Øi:	12	mm
3	1	Hoop		Øy:	16,7	mm
4	1	6		Total Lengde	5	m
5	1	6				
6	1	6				

Revolve NTNU

Eirik Bodsberg
Chief Mechanical Engineer
Revolve NTNU
0047 40 766 222

S.P. Andersens veg 3
c/o MTP Valgrinda
7491 Trondheim, Norway

Appendix E

HBM Datasheet - U93

Data Sheet

U93

Force Transducer

Special features

- **Tensile/compressive force transducer**
- **Simple installation thanks to flange connection on both sides**
- **Integrated TEDS electronic data sheet**
- **Compact**
- **Robust**
- **Stainless steel transducer**
- **Suitable for cable drag chains**

Dimensions (in mm; 1 mm = 0.03937 inches)

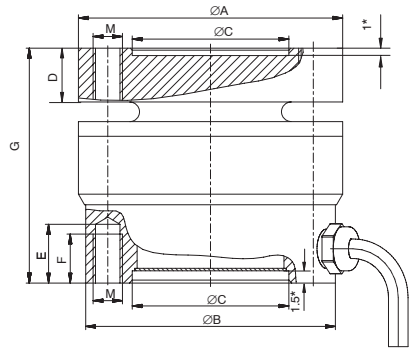

U93/1 kN ... 10 kN

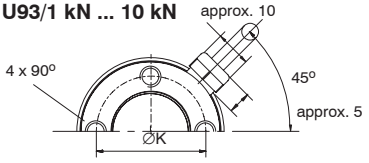

U93/20 kN ... 50 kN

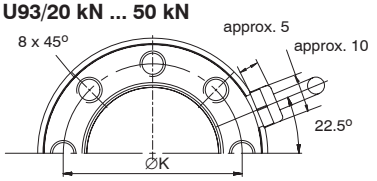

Nominal (rated) force	ØA	ØB	ØC H8	D	E	F	G	ØK ±0.1	M
U93/1 kN ...10 kN	35	33	18	6.2	9	7	30.5	26	M5
U93/20 kN ...50 kN	54	51	32	11	12	10	48	42	M6

* admissible centering depth

Specifications (data per VDI/VDE 2638 standards)

Type			**U93**					
Data as per VDI 2638								
Nominal (rated) force	F_{nom}	**kN**	**1**	**2**	**5**	**10**	**20**	**50**
Nominal (rated) sensitivity	C_{nom}	mV/V	0.5	1	0.5	1	0.5	1
Relative sensitivity error (compression)	d_c	%	< ± 0.5					
Relative zero signal error	$d_{s,o}$	mV/V	< ± 0.075					
Rel. reversibility error (0.5 F_{nom})	$v_{0.5}$	%	< ± 0.5					
Relative linearity error	d_{lin}	%	< ± 0.5					
Effect of temperature on sensitivity/ 10 K, related to nominal (rated) sensitivity	TK_C	%	< ± 0.5					
Effect of temperature on zero signal/ 10 K, related to nominal (rated) sensitivity	TK_0	%	< ± 0.8	< ± 0.5	< ± 0.8	< ± 0.5	< ± 0.8	< ± 0.5
Relative creep over 30 min	d_{crF+E}	%	< ± 0.2					
Effect of lateral forces (lateral force 10% F_{nom}) [1]	d_Q	%	< 0,2		< 0,5		< 0,4	
Effect of eccentricity per mm	d_E	%	< 0.07		< 0.03		< 0.12	
Input resistance	R_i	Ω	> 295					
Output resistance	R_o	Ω	230–350					
Isolation resistance	R_{is}	Ω	$>1 \cdot 10^9$					
Reference excitation voltage	U_{ref}	V	5					
Operating range of the excitation voltage	$B_{U,G}$	V	0.5...12					
Nominal temperature range	$B_{t,nom}$	°C	–10...+70					
Operating temperature range	$B_{t,G}$	°C	–30...+85					
Storage temperature range	$B_{t,S}$	°C	–50...+85					
Reference temperature	t_{ref}	°C	+23					
Max. operating force	(F_G)	%	180					
Breaking force	(F_B)	%	> 400		> 300		> 300	
Lateral force limit [1]	(F_Q)	%	100		80		40	
Permissible force application eccentricity	e_G	mm	1.5		3		6	
Nominal (rated) displacement (± 15%)	S_{nom}	mm	0.01	0.02	0.02	0.04	0.01	0.03
Fundamental resonance frequency	f_G	kHz	7.9		11.7		10.3	
Weight with cable, approx.		g	200					600
Relative permissible oscillatory stress	F_{rb}	%	15 0					
Cable connection, six–wire connection			3 m cable length; outside diameter 4 mm; 6 x 0.08 mm^2; polyurethane sheath; min. bending radius R10					
Degree of protection per DIN 60529			IP67					
Transducer identification			TEDS, as per IEEE 1451.4					

[1] relative to a point of contact on the force application surface

Pin assignment

Six wire circuit

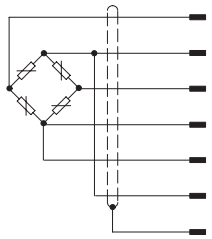

wh (white)	Measurement signal (+) U_A
bk (black)	Excitation voltage (–) U_B TEDS
rd (red)	Measurement signal (–) U_A
bu (blue)	Excitation voltage (+) U_B
gn (green)	Sense lead (+)
gy (gray)	Sense lead (–) TEDS
ye (yellow)	Cable shield, connected to the housing

Order Nos.: Force Transducer

Order Code	Nominal (rated) force						Unit
1-U93 ...	1	2	5	10	20	50	kN

Options:
U93 force transducer, version options

Code	Nominal (rated) force
1K00	1 kN
2K00	2 kN
5K00	5 kN
10K0	10 kN
20K0	20 kN
50K0	50 kN

Code	Cable length
03	3 m
06	6 m
12	12 m

Code	Cable version
Y	free ends
F	15-pin D-Sub plug
N	MS3106PEMV plug
Q	Sub-HD plug (QuantumX)

Preferred version available soon

K-U93 - | 2K00 | - | 0 3 | - | Y |

Hottinger Baldwin Messtechnik GmbH

Im Tiefen See 45 · 64293 Darmstadt · Germany
Tel. +49 6151 803-0 · Fax: +49 6151 803-9100
Email: info@hbm.com · www.hbm.com

measure and predict with confidence

B2083-2.3 en

Appendix F

HBM Datasheet - U2A

U2A…

Load cells

Special features

- **Load cells made of stainless steel**
- **Max. capacities: 50 kg … 20 t**
- **Suitable for scales according to OIML R60 up to 1000 d**
- **Six wire circuit**
- **Low profile**
- **For tensile loads**
- **Meets EMC requirements according to EN 45 501**
- **Explosion proof version (optional)**

Dimensions (in mm; 1 mm= 0.03937 inches)

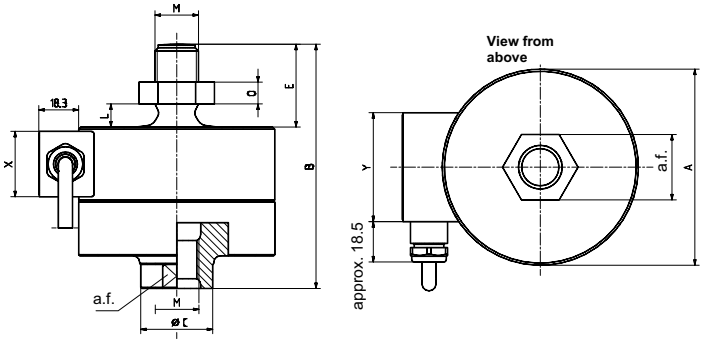

Max. cap. [t]	$A_{-0,2}$	B	C	E	L_{min}	M	O	a.f.	X	Y
0.05 … 1	50	72	21	24	5*)	M12	6	19	20	35
2	90	112	33	38	10.6	M20x1.5	10	30	30	50
5	100	141	40	47	13.2	M24x2	12	36	30	50
10	135	197	68	67	19	M39x2	19	60	30	50
20	155	232	82	85	24.2	M48x2	22	70	30	50

*) with U2A/1 t: 7.4 mm

Specifications

Type			U2A		
Accuracy class			0.2	0.1	D1
Max. numbers of load cell verification intervall	n_{LC}		-	-	1000
Max. capacity	E_{max}	kg t	50 -	100, 200, 500 10, 20	500 1, 2, 5
Minimum load cell verification interval	v_{min}		-	-	0.0286
Sensitivity	C_n	mV/V	2		
Tolerance on sensitivity					
with tensile loads		%	<±0.20		<±0.20
with compressive loads		%	<±1.50	<±0.50	<±0.50
Temperature effect on sensitivity[1)]	TK_C				
in nominal temperature range		%/10 K	<±0.05		<±0.05
in service temperature range		%/10 K	<±0.10		<±0.10
Temperature effect on zero balance	TK_0				
in nominal temperature range		%/10 K	<±0.05		<±0.04
in operating temperature range		%/10 K	<±0.10		<±0.10
Hysteresis error [1)]	d_{hy}	%	<±0.15		<±0.07
Non-linearity[1)]	d_{lin}		<±0.20	<±0.10	<±0.05
Creep over 30 min.	d_{cr}		<±0.06		<±0.05
Input resistance	R_{LC}	Ω	340 … 450		
Output resistance	R_0		356±0.2		
Insulation resistance	R_{iso}	GΩ	>5		
Reference excitation voltage	U_{ref}	V	5		
Nominal range of excitation voltage	B_u		0.5 … 10	0.5 … 12	
Max. permissible excitation voltage			12	18	
Nominal temperature range	B_T	°C [°F]	-10 … +40 [14 … 104]		
Operating temperature range[2)]	B_{tu}		-30 … +85 (-30 … +120) [-22 … 185] [-22 … 248]		
Storage temperature range	B_{tl}		-50 … +85 [-58 … 185]		
Safe load limit	E_L	% from max. capac.	130	150	
Breaking load	E_d		300		
Rel. stat. lateral load limit	E_{lq}		25		
Permissible dynamic load (peak to peak according to DIN 50100)	F_{srel}		100	160	
Degree of protection (IP) to EN 60529 (IEC 529)			IP 67		
Material: Measuring body Cable gland Cable sheath			Stainless steel[3)] Nickel plated brass, Silicone Thermoplast. elastomere		

1) The data for Non-linearity, hysteresis error and temperature effect on sensitivity are typical values. The sum of these data meets the requirements according to OIML R60.
2) Optionally available with extended operating temperature range.
3) According to EN 10088-1

Mechanical values

Max. capacity [t]	Deflection at max. capacity (s_{nom}), approx. [mm]	Weight (G), approx. [kg]	Cable length [m]
0.05	< 0.1	0.8	3
0.1	< 0.1	0.8	3
0.2	< 0.1	0.8	3
0.5	< 0.1	0.8	3
1	< 0.1	0.8	3
2	< 0.07	2.9	6
5	< 0.07	4.3	6
10	< 0.09	10.7	12
20	< 0.09	15.9	12

Mounting accessories (in mm; 1 mm = 0.03937 inches)

Knuckle eye ZGOW

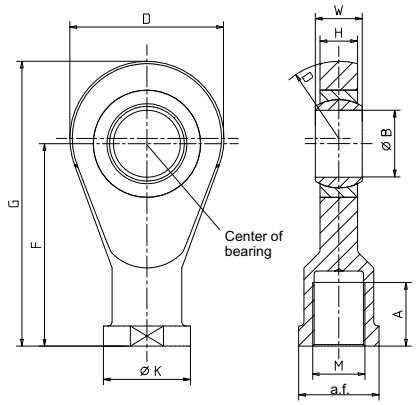

Knuckle eye ZGUW

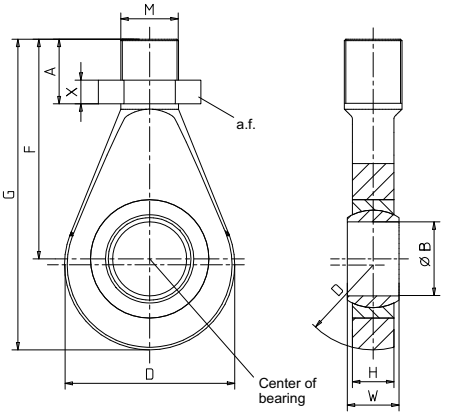

Max. cap. [t]	Knuckle eye ZGOW	Weight [kg]	A	∅B	D	F	G	H	∅K	M	a.f.	W
0.05 … 1	U2A/1T/ZGOW	0.2	22	12^{H7}	32	50	66	12	22	M12	19	16
2	U2A/2T/ZGOW	0.5	33	20^{H7}	50	77	102	18	34	M20x1.5	32	25
5	U2A/5T/ZGOW	0.8	42	25^{H7}	60	94	124	22	42	M24x2	36	31
10	U2A/10T/ZGOW	3.2	50	$50^{+0.002}_{-0.014}$	115	151	212,5	28	65	M39x2	60	35
20	U2A/20T/ZGOW	4.8	60	$60^{+0,003}_{-0,018}$	126	167	235	36	82	M48x2	70	44

Max. cap. [t]	Knuckle eye ZGUW	Weight [kg]	A	∅B	D	F	G	H	M	a.f.	W	X
0.05 … 1	U2A/1T/ZGUW	0.1	33	12^{H7}	32	54	70	12	M12	19	16	7
2	U2A/2T/ZGUW	0.2	47	20^{H7}	50	78	103	18	M20x1,5	32	25	9
5	U2A/5T/ZGUW	0.4	57	25^{H7}	60	94	124	22	M24x2	36	31	10
10	U2A/10T/ZGUW	1.1	65.5	$50^{+0.002}_{-0.014}$	115	148.5	210	28	M39x2	60	35	16
20	U2A/20T/ZGUW	3.2	80	$60^{+0.003}_{-0.018}$	126	168	236	36	M48x2	70	44	18

Load cell U2A with monted knuckle eyes ZGOW, ZGUW

Max. capacity [t]	A_{min}	A_{max}	F_{min}	F_{max}	Min. depth for screwing		Tightening torque M_A [N·m]
					B	C	
0.05...0.5	139	156	171	188	9.6	9.6	60 *)
1	141	156	173	188	9.6	9.6	60
2	212	234	262	284	16	16	300
5	260	288	320	348	19.2	19.2	500
10	418	436	541	559	27	31.2	2500
20	466	489	602	625	36.6	38.4	4500

*) Do not exceed this value and handle the load cell with care during fastening to avoid damage to the thin measuring diaphragm. Hold the lock nut in place.

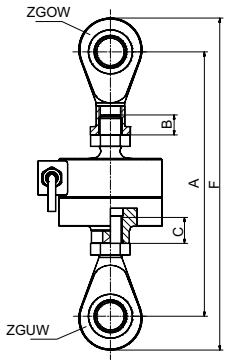

Mounting accessories, continued (in mm; 1 mm = 0.03937 inches)

U2A, with ZGOW, without adaptor

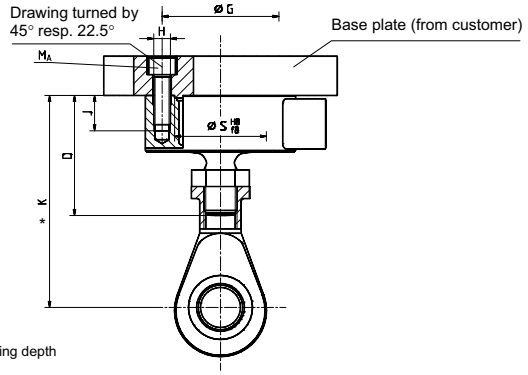

* Dimension, with preferred screwing depth

Max. capacity [t]	D	∅G	H	J	K	∅S	M_A 1) [N·m]
0,05 … 0,5	47	42	4xM5	13	84 … 86,4	34	5
1	47	42	4xM5	13	86,4	34	5
2	72	70	4xM10	20,5	131,6	55	35
5	86	78	4xM12	19	158,2	61	60
10	122	105	8xM12	16	244	79	60
20	142	125	8xM16	26	270,2	97	150

1) Recommended values for a dry thread, using a torque wrench

Wiring code

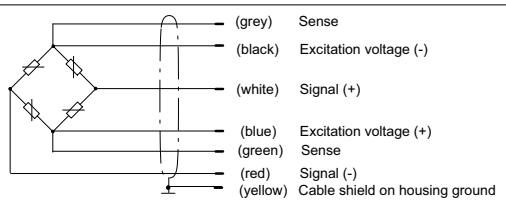

Options

Explosion-proof versions

AI1/21 IECEx+ATEX zone 1/21 + FM intrinsically safe, II2G Ex ia IIC T6/T4 Gb / II2D Ex ia IIIC T125°C Db [only with Option 6=N]
AI2/21 IECEx+ATEX zone 2/21 non-intrinsically safe, II3G Ex nA IIC T6/T4 Gc / II2D Ex tb IIIC T125°C Db [only with Option 6=N]
AIM1 IECEx+ATEX M1, intrinsically safe I M 1 Ex ia I Ma [only with Option 6 = N]

Accessories, to be ordered separately

- U2A knuckle eyes, above, U2A/.../ZGOW
- U2A, knuckle eyes, below U2A/.../ZGUW
- EEK Grounding cable

Hottinger Baldwin Messtechnik GmbH
Im Tiefen See 45 · 64293 Darmstadt · Germany
Tel. +49 6151 803-0 · Fax +49 6151 803-9100
Email: info@hbm.com · www.hbm.com

B1000-7.0 en HBM: public

Appendix G

Load Case

Load Cases - Revolve NTNU

One of the sub-goals for Revolve NTNU is *sustaining the theoretical performance of last years car* (Luna), thus the decision was made not to alter the load cases.

2021 dimensioning load cases [N]							
Front wheels							
Load case	Turn @ 112 km/h		Acceleration	Brake @ 112 km/h	3g bump	2g bump + turn @ 112 km/h (outside wh.)	2g bump + brake @ 112 km/h
	Inside wh.	Outside wh.					
Fx	0	0	625 (+121 vs. 2019) (+68 vs. 2020)	3649 (+194 vs. 2019) (+38 vs. 2020)	0	0	3649 (+194 vs. 2019) (+38 vs. 2020)
Fy	1111 (+232 vs. 2019) (-16 vs. 2020)	3248 (+21 vs. 2019) (-6 vs. 2020)	0	0	0	3248 (+21 vs. 2019) (-6 vs. 2020)	0
Fz	486 (+111 vs. 2019) (-7 vs. 2020)	2466 (+123 vs. 2019) (-78 vs. 2020)	618 (+107 vs. 2019) (+62 vs. 2020)	2335 (+219 vs. 2019) (+47 vs. 2020)	1679 (-9 vs. 2019) (-15 vs. 2020)	3585 (+117 vs. 2019) (-89 vs. 2020)	3454 (+212 vs. 2019) (+36 vs. 2020)

Figure G.1: Load cases used in 2021 and 2022

Appendix H

Results

H.1 Beam model

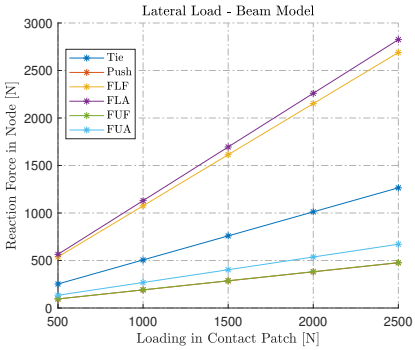

(a) Lateral load case.

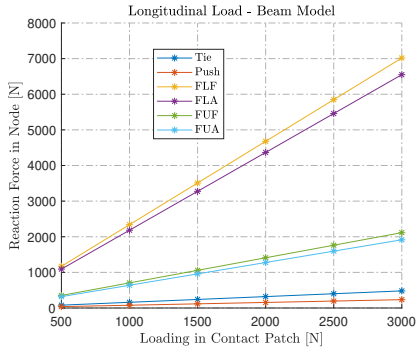

(b) Longitudinal load case.

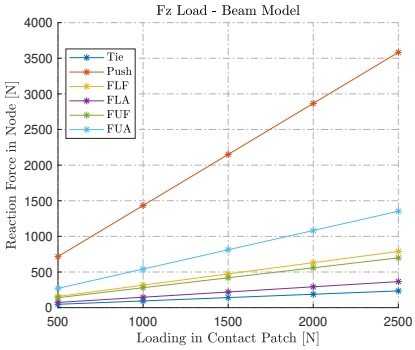

(c) Vertical load case.

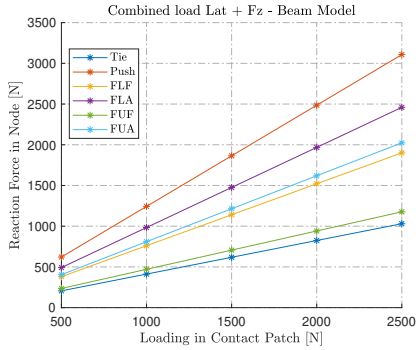

(d) Combined load case, vertical and lateral.

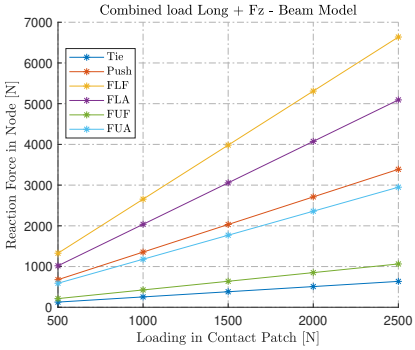

(e) Combined load case, vertical and longitudinal.

H.2 Strain Model

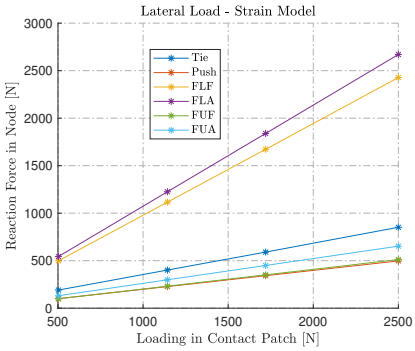

(a) Lateral load case.

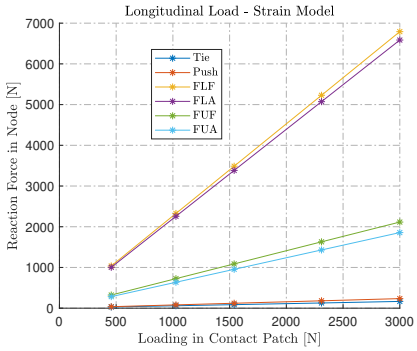

(b) Longitudinal load case.

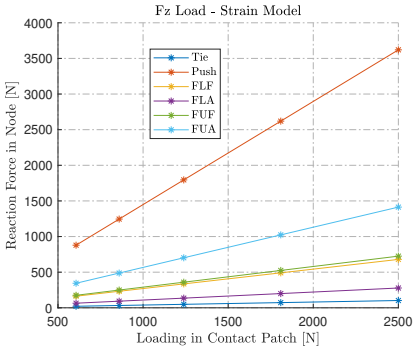

(c) Vertical load case.

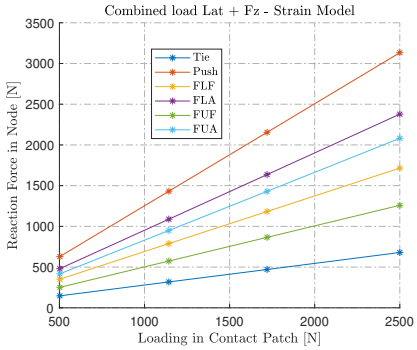

(d) Combined load case, vertical and lateral.

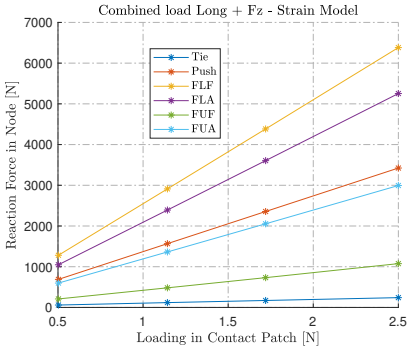

(e) Combined load case, vertical and longitudinal.

H.3 Beam vs Strain Model - Newton

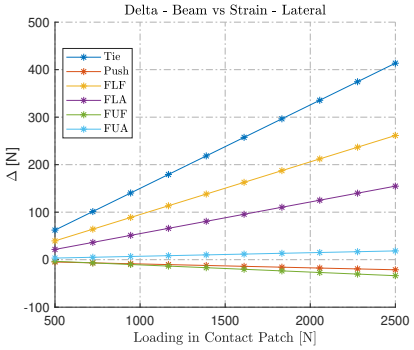

(a) Lateral load case.

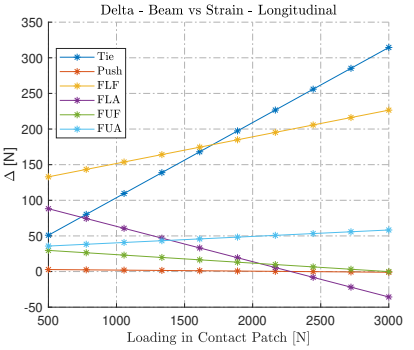

(b) Longitudinal load case.

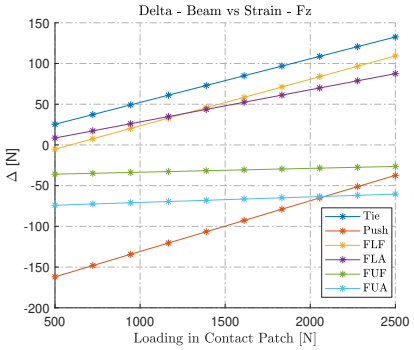

(c) Vertical load case.

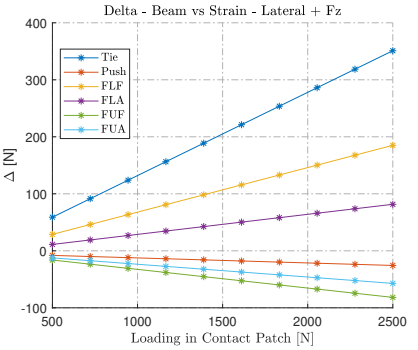

(d) Combined load case, vertical and lateral.

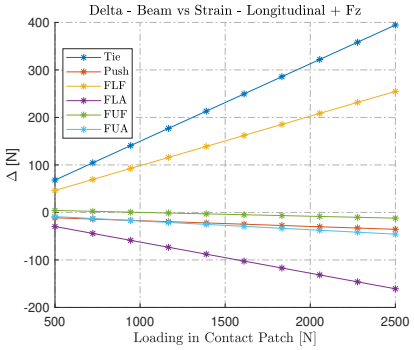

(e) Combined load case, vertical and longitudinal.

H.4 Beam vs Strain Model - Percentage

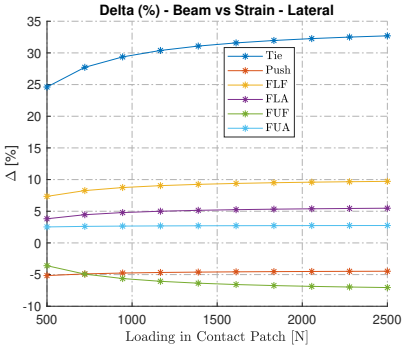

(a) Lateral load case.

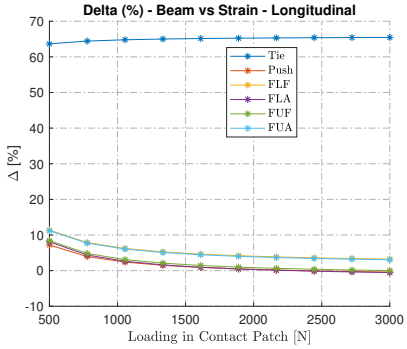

(b) Longitudinal load case.

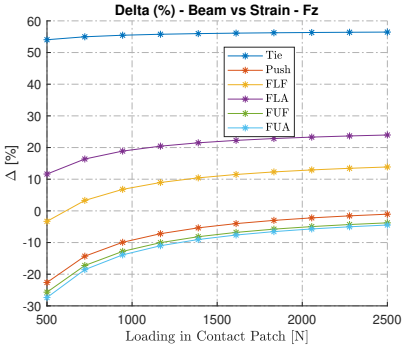

(c) Vertical load case.

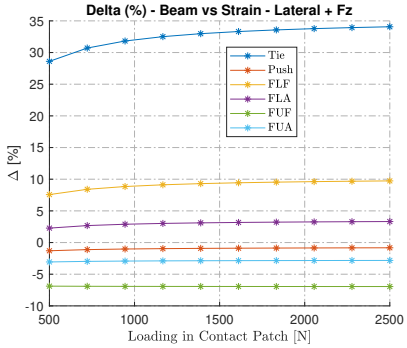

(d) Combined load case, vertical and lateral.

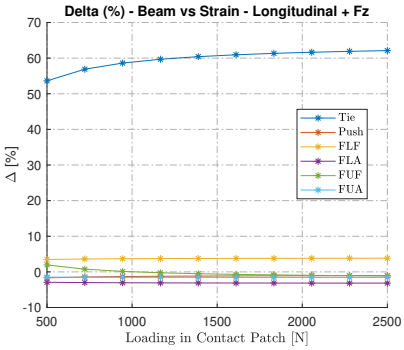

(e) Combined load case, vertical and longitudinal.

H.5 Testing

H.5.1 Lateral

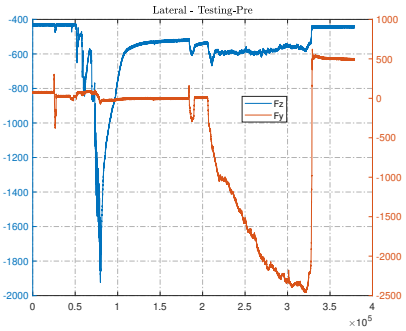

(a) Applied load, raw data, F_z and F_y.

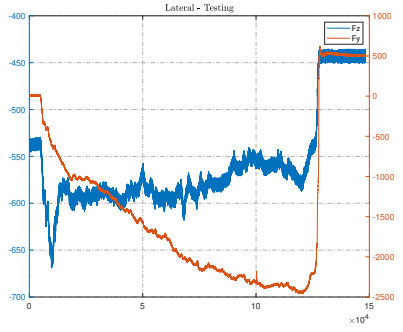

(b) Applied load, trimmed to the section of interest, F_z and F_y.

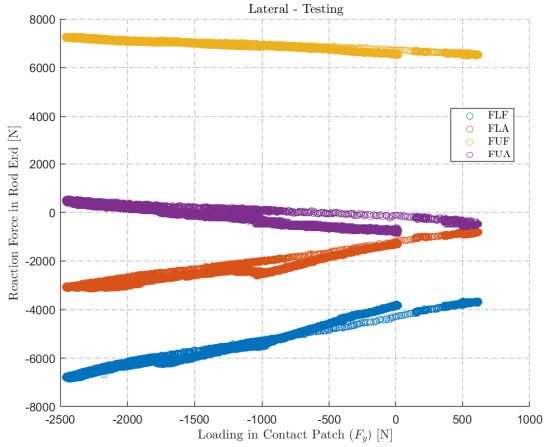

(c) Reaction forces due to lateral applied load.

H.5.2 Longitudinal

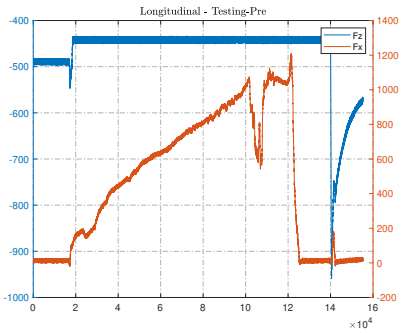

(a) Applied load, raw data, F_z and F_x.

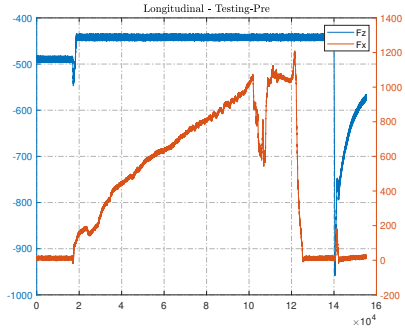

(b) Applied load, trimmed to the section of interest, F_z and F_x.

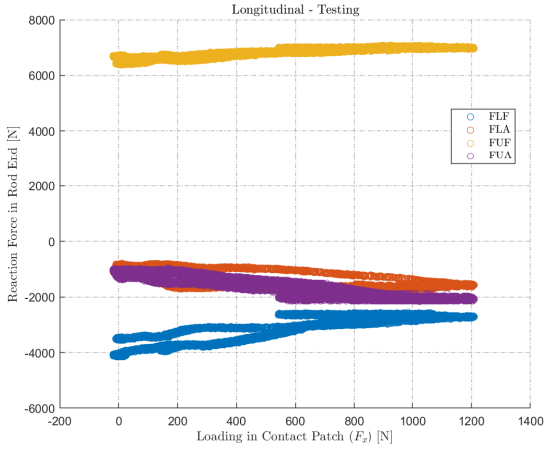

(c) Reaction forces due to longitudinal applied load.

H.5.3 F_z Load

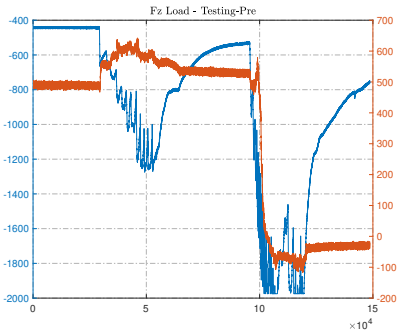

(a) Applied load, raw data, F_z and F_y.

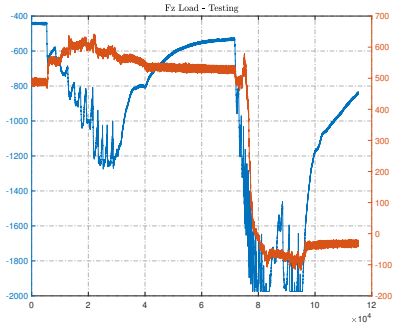

(b) Applied load, trimmed to the section of interest, F_z and F_y.

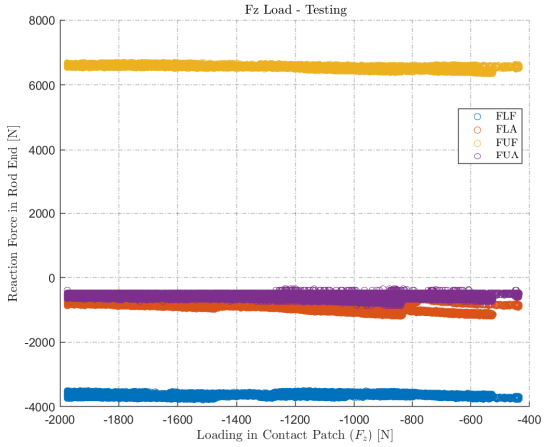

(c) Reaction forces due to vertical applied load.

H.5.4 Combined Load - Lateral + F_z

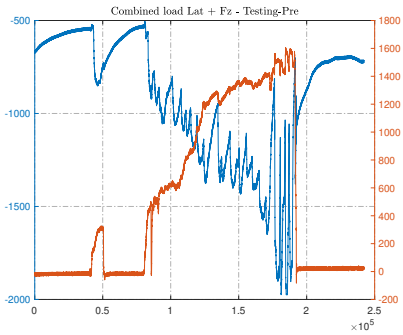

(a) Applied load, raw data, F_z and F_y.

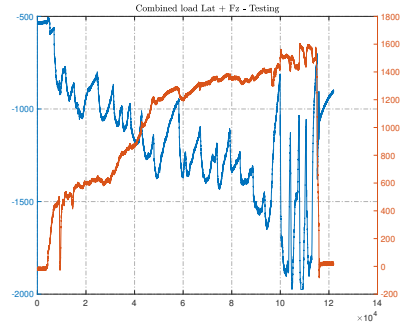

(b) Applied load, trimmed to the section of interest, F_z and F_y.

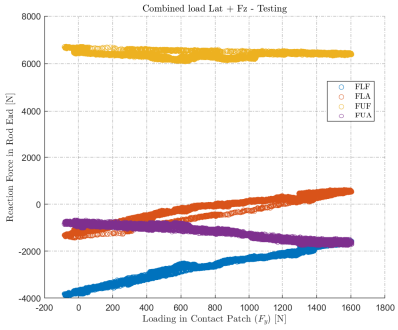

(c) Reaction forces with respect to increased F_y applied load.

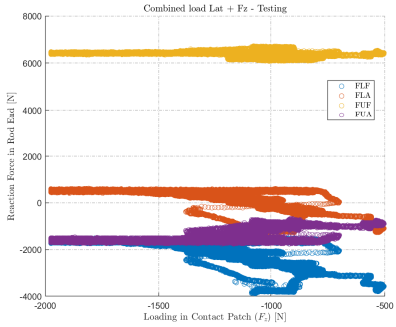

(d) Reaction forces with respect to increased F_z applied load.

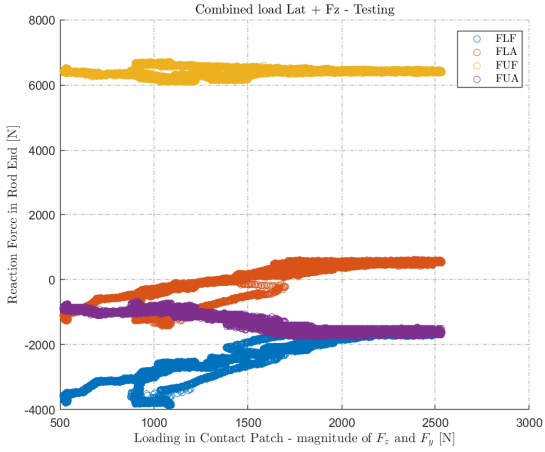

(e) Reaction forces due to the magnitude applied load.

H.5.5 Combined Load - Longitudinal + F_z

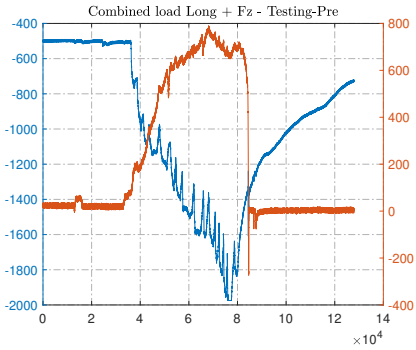

(a) Applied load, raw data, F_z and F_x.

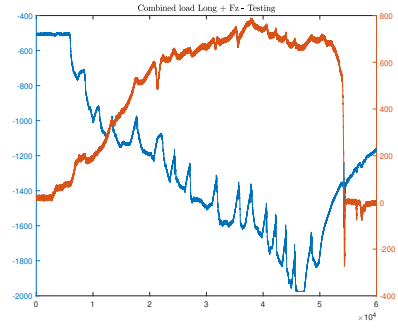

(b) Applied load, trimmed to the section of interest, F_z and F_x.

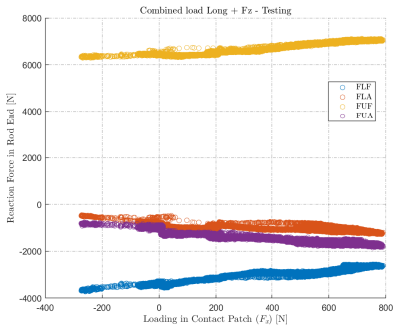

(c) Reaction forces with respect to increased F_x applied load.

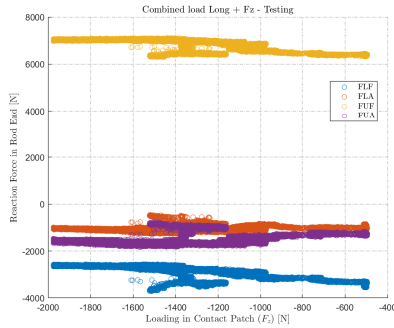

(d) Reaction forces with respect to increased F_z applied load.

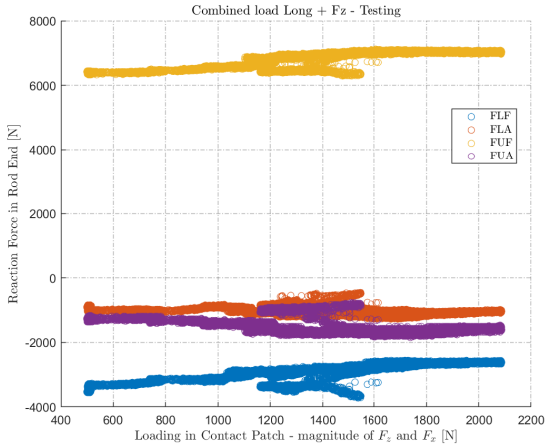

(e) Reaction forces due to the magnitude applied load.

H.6 Testing - Corrected

H.6.1 Lateral

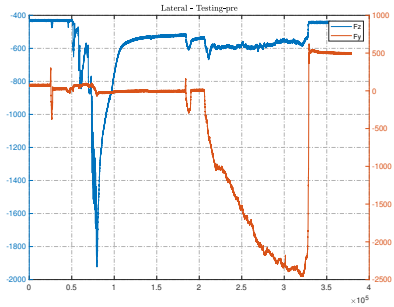

(a) Applied load, raw data, F_z and F_y.

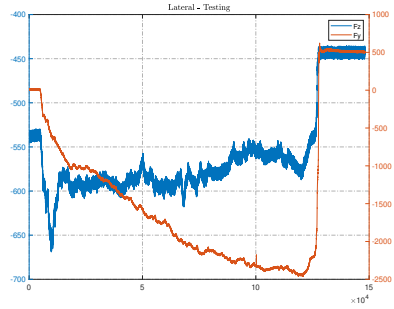

(b) Applied load, trimmed to the section of interest, F_z and F_y.

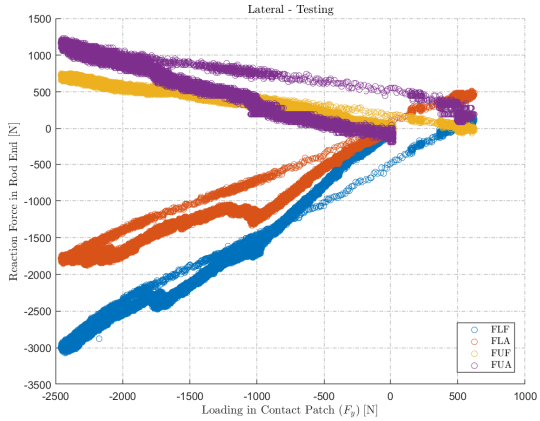

(c) Reaction forces due to lateral applied load.

H.6.2 Longitudinal

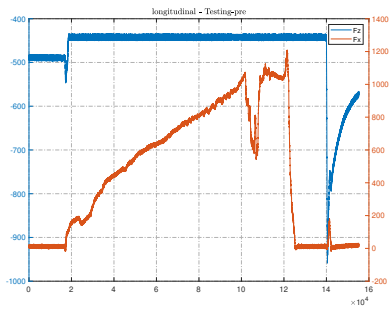

(a) Applied load, raw data, F_z and F_x.

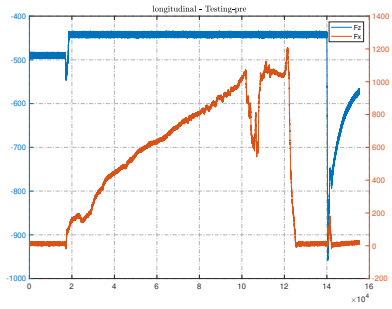

(b) Applied load, trimmed to the section of interest, F_z and F_x.

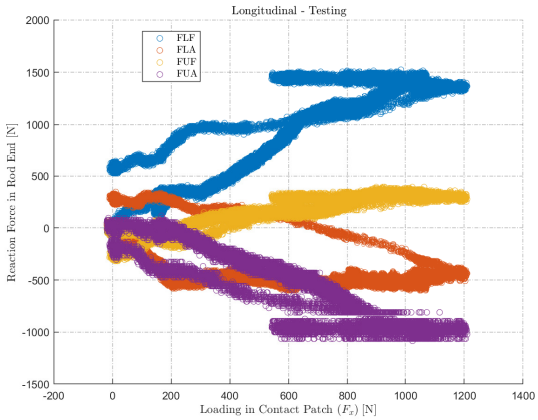

(c) Reaction forces due to longitudinal applied load.

H.6.3 F_z Load

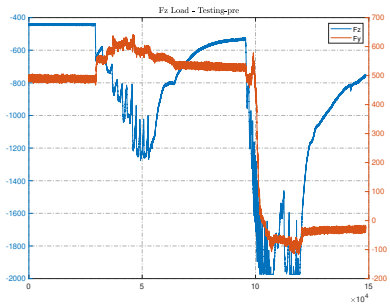

(a) Applied load, raw data, F_z and F_y.

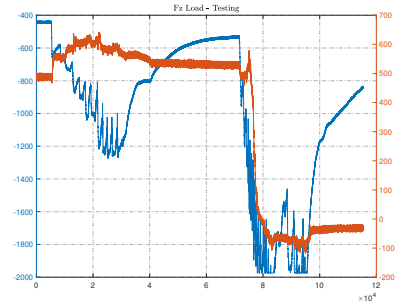

(b) Applied load, trimmed to the section of interest, F_z and F_y.

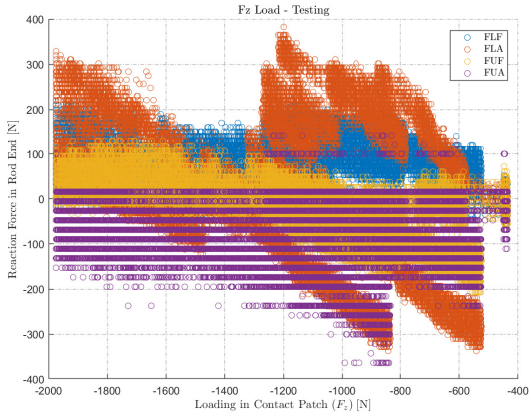

(c) Reaction forces due to vertical applied load.

H.6.4 Combined Load - Lateral + F_z

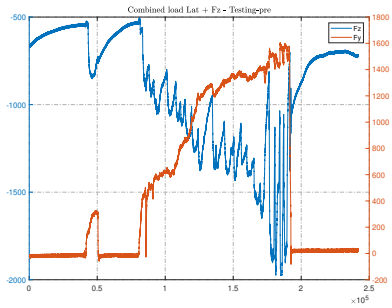

(a) Applied load, raw data, F_z and F_y.

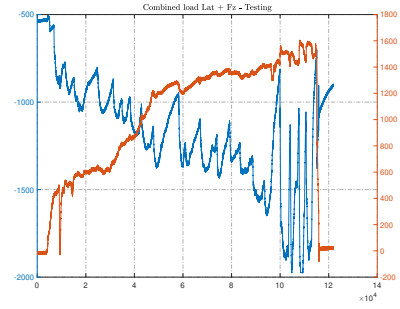

(b) Applied load, trimmed to the section of interest, F_z and F_y.

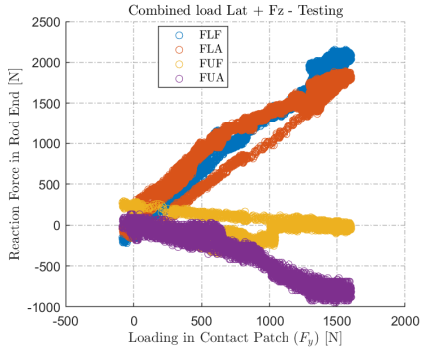

(c) Reaction forces with respect to increased F_y applied load.

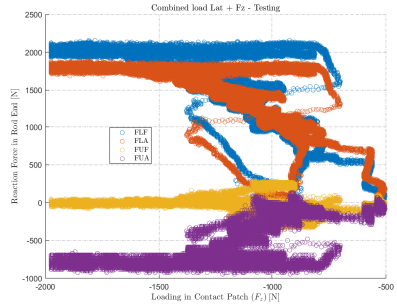

(d) Reaction forces with respect to increased F_z applied load.

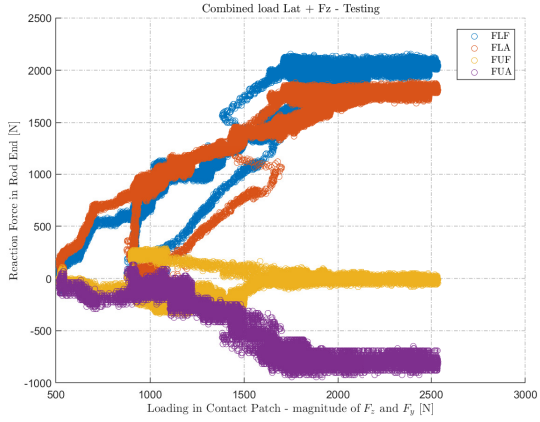

(e) Reaction forces due to the magnitude applied load.

H.6.5 Combined Load - Longitudinal + F_z

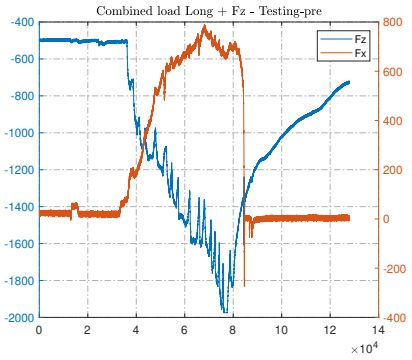

(a) Applied load, raw data, F_z and F_x.

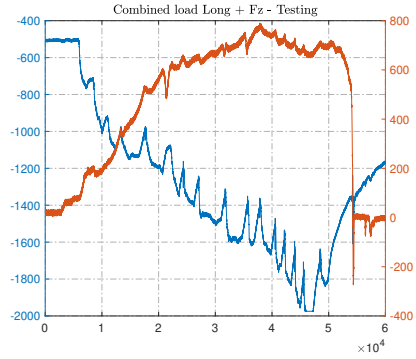

(b) Applied load, trimmed to the section of interest, F_z and F_x.

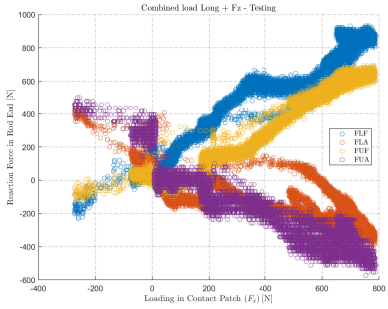

(c) Reaction forces with respect to increased F_x applied load.

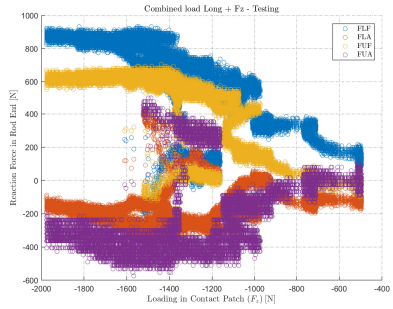

(d) Reaction forces with respect to increased F_z applied load.

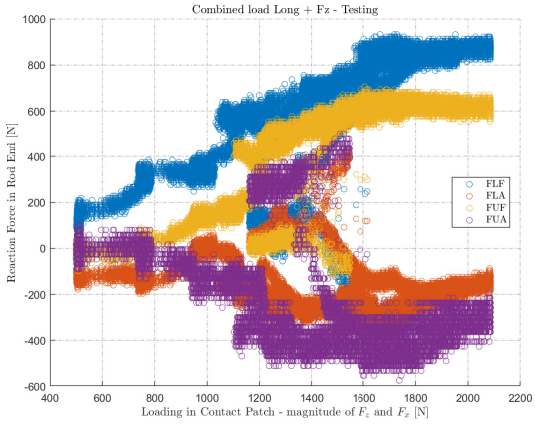

(e) Reaction forces due to the magnitude applied load.

H.7 Testing vs Models

H.7.1 Not-Corrected

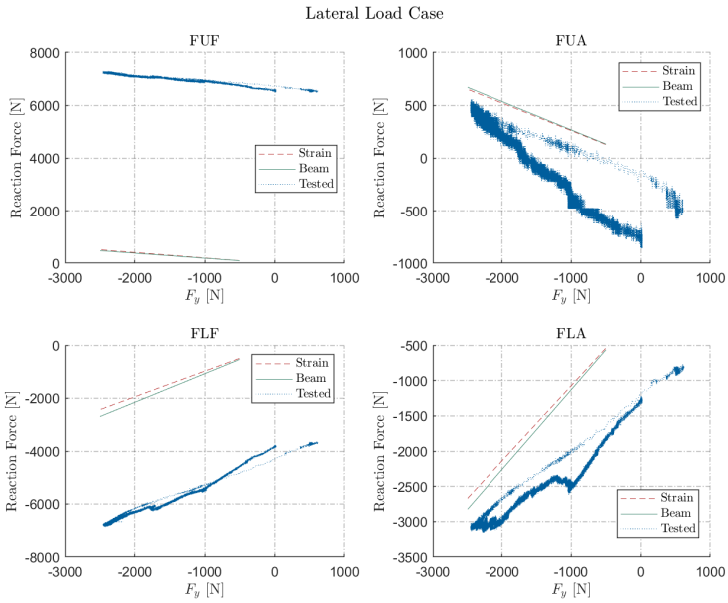

Figure H.15: Lateral load case.

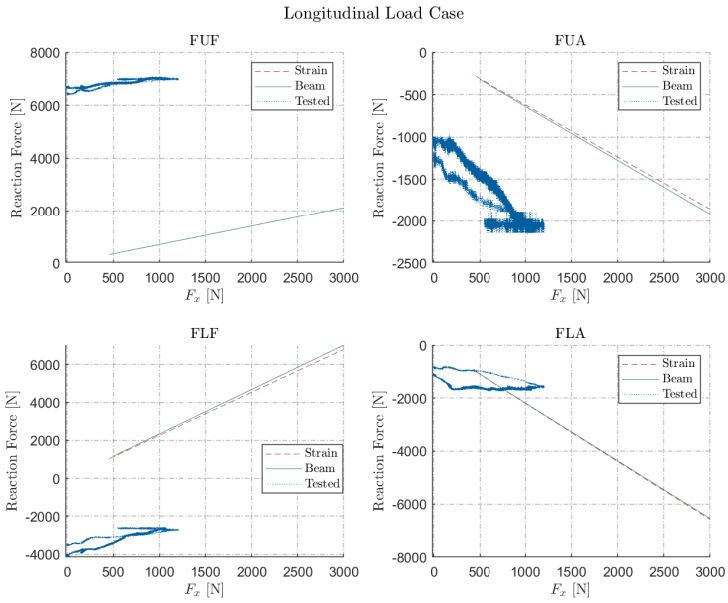

Figure H.16: Longitudinal load case.

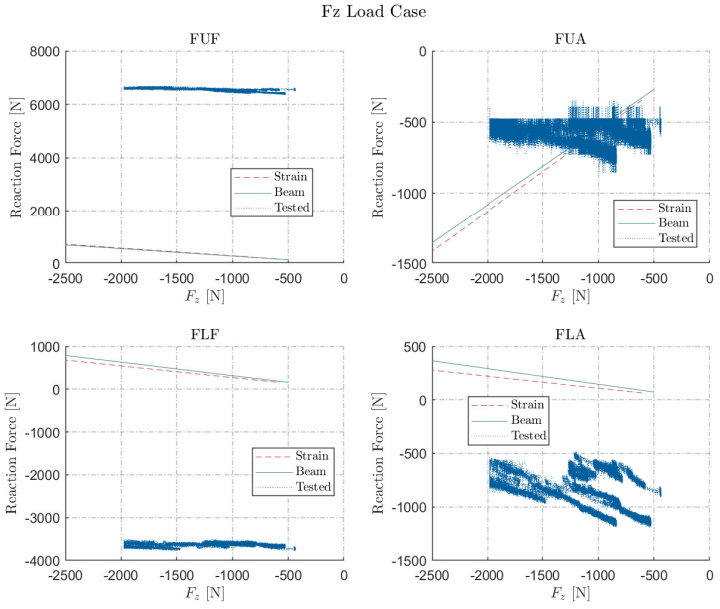

Figure H.17: Vertical load case.

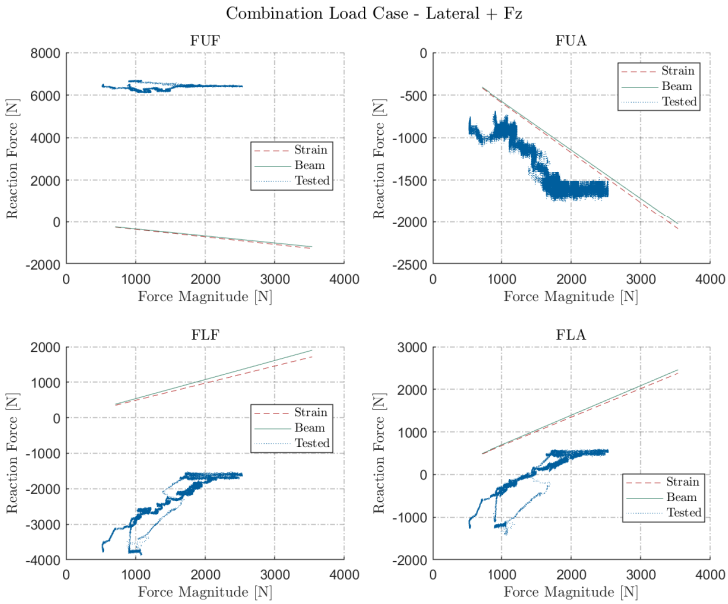

Figure H.18: Combined load case, lateral and F_z.

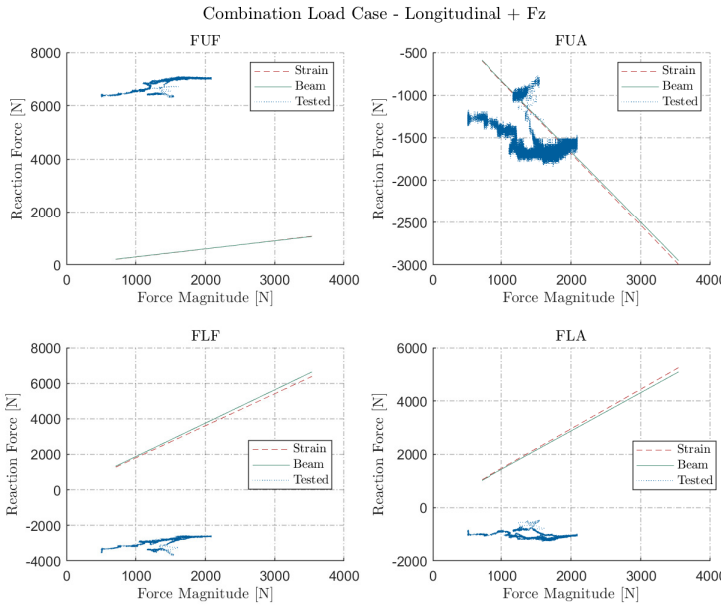

Figure H.19: Combined load case, longitudinal and F_z.

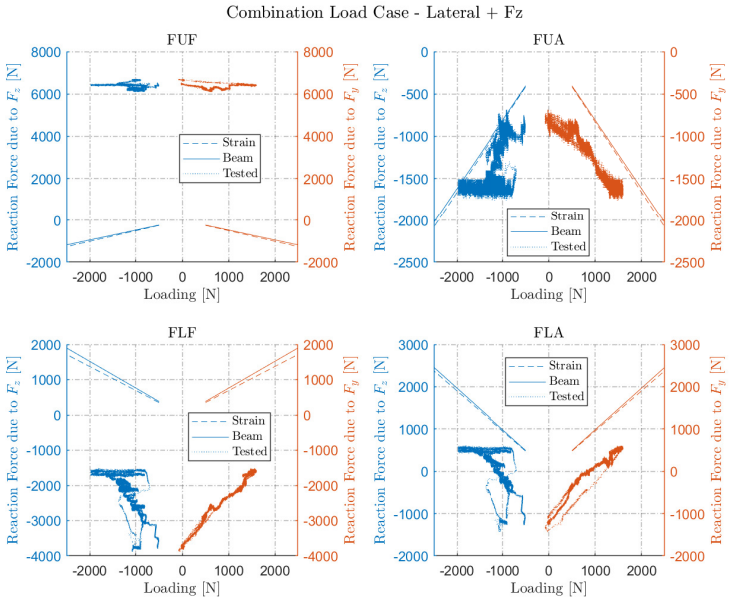

Figure H.20: Combined load case, decomposed, lateral and F_z.

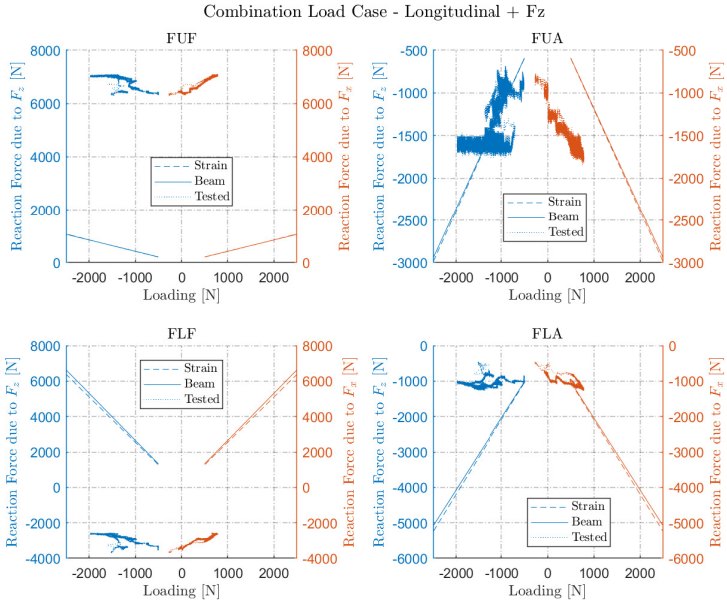

Figure H.21: Combined load case, decomposed, longitudinal and F_z.

H.7.2 Corrected

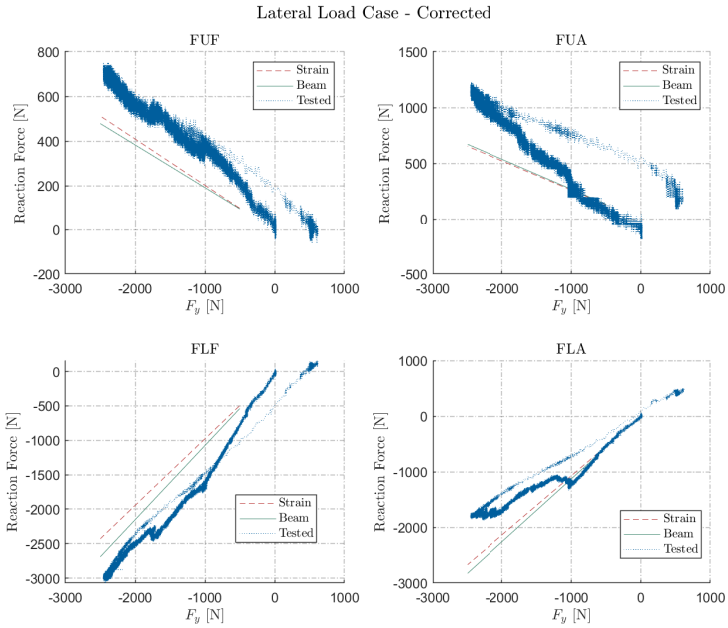

Figure H.22: Lateral load case.

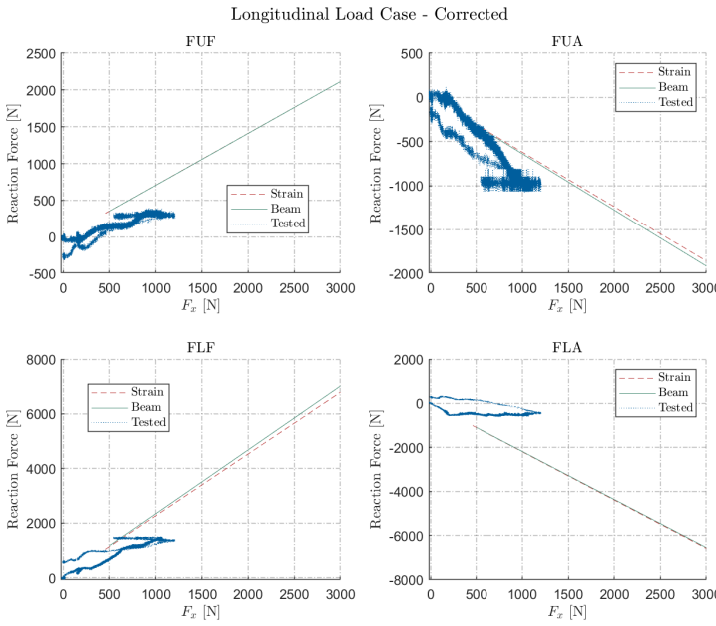

Figure H.23: Longitudinal load case.

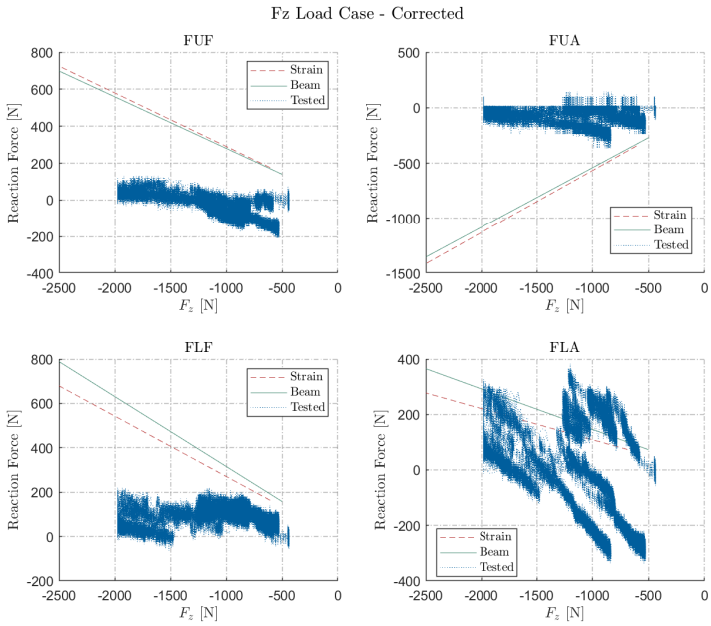

Figure H.24: Vertical load case.

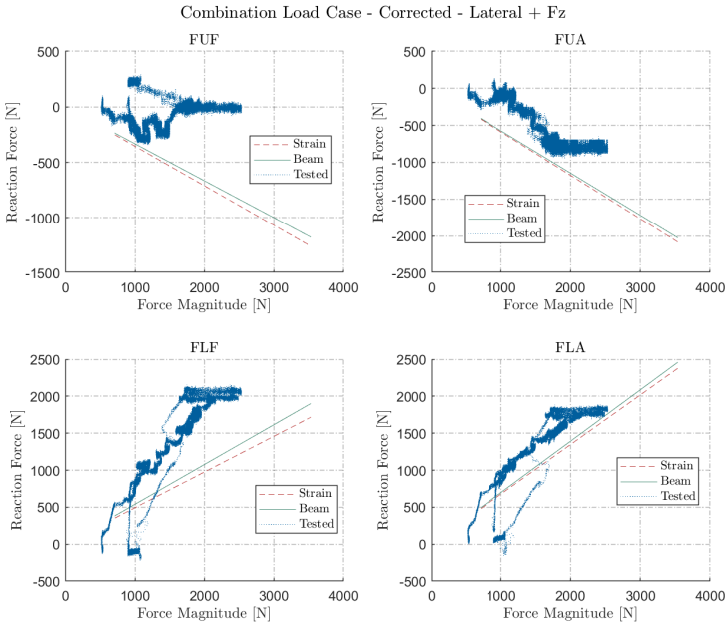

Figure H.25: Combined load case, lateral and F_z.

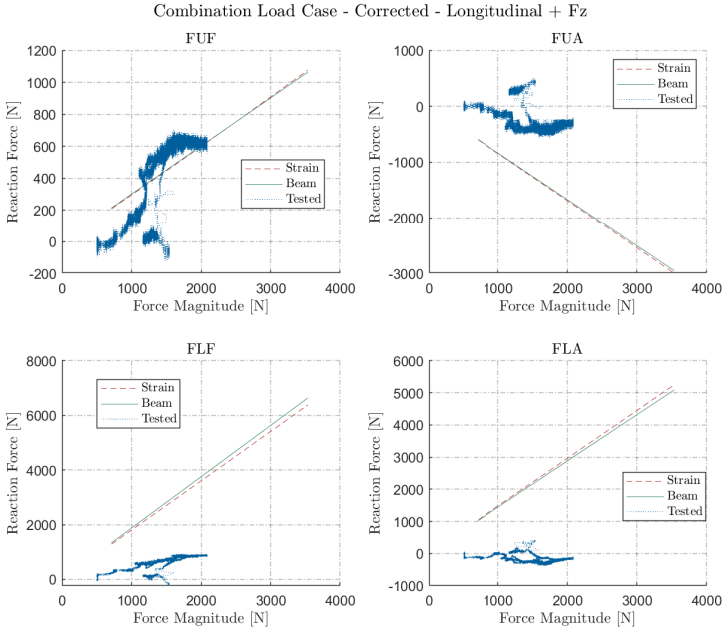

Figure H.26: Combined load case, longitudinal and F_z.

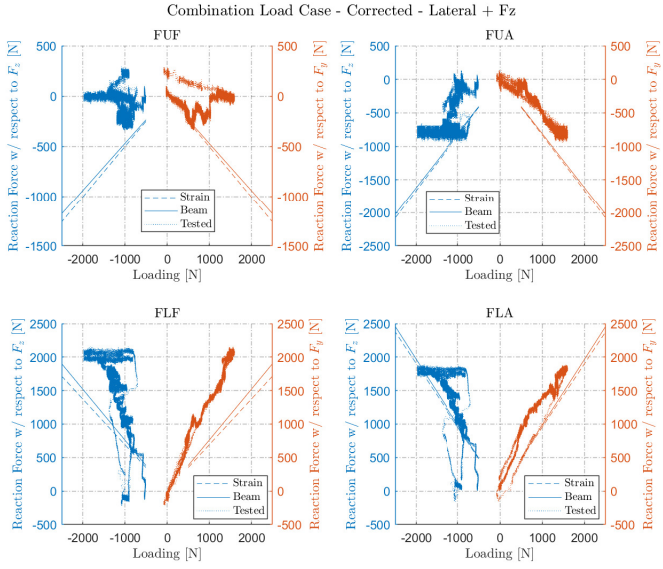

Figure H.27: Combined load case, decomposed, lateral and F_z.

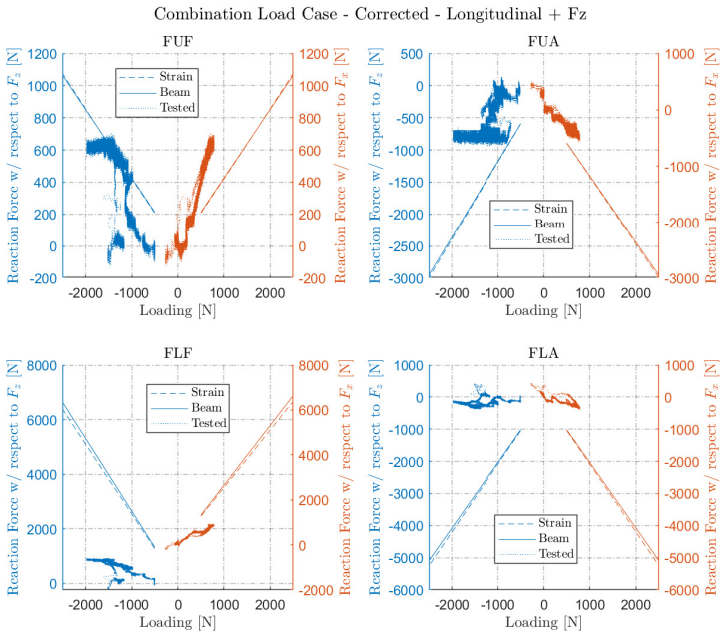

Figure H.28: Combined load case, decomposed, longitudinal and F_z.

Sondre Audal

Validation of Force Propagation On A FS Race Car

NTNU
Norwegian University of
Science and Technology